



DESIGN AND MODELLING OF UNDERGROUND DECAY HEAT REMOVAL SYSTEM FOR A DISTRICT HEATING REACTOR

Lappeenranta–Lahti University of Technology LUT
LUT School of Energy Systems
Master’s Programme in Energy Technology, Nuclear Engineering

University of Ljubljana
Faculty of Mathematics and Physics
Department of Physics
Nuclear Engineering

Lappeenranta, 2021

Brahim Dif

Supervisors: Prof. D.Sc. (Tech.) Juhani Hyvärinen

D.Sc. (Tech.) Juhani Vihavainen,

Prof. Dr. Iztok Tiselj

ABSTRACT

Lappeenranta–Lahti University of Technology LUT

LUT School of Energy Systems

Energy Technology

Brahim Dif

Design and modelling of an underground decay heat removal system for a district heating reactor

Master's thesis

2021

111 pages, 53 figures, 5 tables

Examiners: Prof. D.Sc. (Tech.) Juhani Hyvärinen and Prof. Dr. Iztok Tiselj

Keywords: Thermal hydraulics, condensation, decay heat, non-condensable gas, TRACE.

Decay heat in fission reactors is a main concern from a safety perspective. Adequate removal of decay heat should be maintained under all circumstances to ensure reactor operability within safety limits and mitigating any undesirable consequences. This could be achieved by utilising passive safety which increases the inherent safety characteristics and reliability of the design.

The study carried out in this report investigates the feasibility of a proposed passive decay heat removal system for a 24 MWth nominal power underground district heating conceptual design. The proposed loop utilises air and steam mixture as a working fluid and relies on natural circulation to eject the heat from the containment to the ground as a buffer.

A Comprehensive review of condensation theory in horizontal tubes is provided in the literature review with a focus on the effect of non-condensable gas (NCG) on heat transfer. An analytical study is then performed using a MATLAB script substantiated with relevant correlations to determine the geometrical and operational parameters of the system. The analysis is initially performed for a pure steam case as a baseline then the effect of NCG is considered in a further updated model. This was followed by a numerical simulation using thermal hydraulic code system (TRACE) to study the overall behaviour of the loop. Both analytical and numerical results are compared.

The work presented in this report shows that removal of decay heat up to one month following shutdown is feasible with the proposed decay heat removal system. The presence of NCG in the loop has little to no effect on the condensation process and does not compromise the overall performance of the system significantly.

ACKNOWLEDGEMENTS

First and foremost, my deepest appreciation goes to my supervisors D.Sc. Juhani Vihavainen, Professor Iztok Tiselj, and Professor Juhani Hyvärinen for their guidance and support throughout the course of this work. I am immensely grateful for the insights and in-depth knowledge shared with me throughout the process that helped me write this thesis.

Most importantly, I would like to thank my parents who always supported me since the very start of my academic journey abroad. I would also like to express my gratitude to all my friends with whom I have shared the past two years of this master's degree programme.

SYMBOLS AND ABBREVIATIONS

Roman characters

h_{fg}	specific latent heat of vaporization	[J/kg]
D_H	hydraulic diameter	[m]
P_d	decay power	[W]
c_p	specific heat capacity	[J/(kg·K)]
q'	heat transfer per unit length	[W/m]
D	diameter	[m]
E	energy	[J]
f	friction coefficient	
g	gravitational acceleration	[m/s ²]
G	mass flux	[kg/m ² s]
H	heat transfer coefficient	[W/m ² · K]
h	specific enthalpy	[J/kg]
k	thermal conductivity	[W/m K]
l, L	length	[m]
m	mass	[kg]
M	molar mass	
Nu	Nusselt number	
P	power	[W]
p	pressure	[bar]
Pr	Prandtl number	
Q	decay heat, heat transfer rate	[W]

q_m	mass flow rate	[kg/s]
r	radius	[m]
R	thermal resistance	[1/(W/m ² ·K)]
Re	Reynolds number	
T	temperature	[°C, K]
t	time	[s]
u	velocity	[m/s]
v	specific volume	[m ³ /kg]
V	volume	[m ³]
V	velocity	[m/s]
W	mass fraction	
x	gas quality	
X	molar fraction, Martinelli's parameter	

Greek characters

α	thermal diffusivity	
μ	dynamic viscosity	[kg/m s]
ε	void fraction	
θ	flooding angle	[rad]
λ	thermal conductivity	[W/m K]
ζ	hydraulic resistance	
ρ	density	[kg/m ³]
Φ	two phase multiplier	
τ	shear stress	[N/m ²]

Subscripts

bot	bottom part of the tube wall
cr	critical
f	fluid
f0, l0	All two-phase flow of vapor liquid mixture assumed to be saturated liquid
fg, lv	latent
fr	friction
g	ground
G,g	gas
i	inner
in	inlet, inner
L, l	liquid
mix	steam and air mixture
nc	non condensable
o	outer
out	outlet
p	pipe
sat	saturation
sp	single phase
top	top part of the pipe wall
tot	total
TP	two phase
v	vapour
w	wall

d decay

Abbreviations

ABWR	Advanced Boiling Water Reactor
BWR	Boiling Water Reactor
DHR	Decay Heat Removal
ESBWR	Economic Simplified Boiling Water Reactor
GHE	Ground Heat Exchanger
HTC	Heat Transfer Coefficient
IAEA	International Atomic Energy Agency
LOCA	Loss of Coolant Accident
MSBL	Main Steam Break Line
NCG	Non-Condensable Gas
NPP	Nuclear Power Plant
PCCS	Passive Containment Cooling System
PWR	Pressurized Water Reactor
RHR	Residual Heat Removal
SMR	Small Modular Reactor

Table of contents

Abstract

Acknowledgements

Symbols and abbreviations

1. Introduction	12
1.1. Background	12
1.2. Project Scope, Aim and Objectives.....	14
1.3. Methodology	15
2. Literature review	16
2.1. Small Modular Reactors.....	16
2.2. Passive Systems and Natural Circulation.....	20
2.2.1. Passive Containment Cooling Systems	20
2.3. Condensation.....	24
2.3.1. Flow pattern maps	24
2.3.2. Condensation inside horizontal pipes.....	26
2.3.3. Heat transfer calculations	28
2.3.4. Pressure drop.....	29
2.3.5. Effect of non-condensable gas	31
3. Theoretical Framework/Analytical Study.....	33
3.1. Pure Steam Case Model	34
3.1.1. Heat transfer calculations	34
3.1.2. Pressure drop calculations	44
3.2. Steam and Non-Condensable Gas.....	51
4. Computational Study/Numerical Model	59
4.1. Thermal Hydraulic System Codes	59
4.2. TRACE Code	60
4.2.1. Field equations	60
4.2.2. Trace calculation algorithm and condensation models	61
4.3. Model Nodalization.....	62
4.3.1. Single pipe test	62
4.3.2. Loop study.....	66

5. Results and discussion	68
5.1. Analytical Results	68
5.1.1. Pure steam case results.....	68
5.1.2. Model with NCG and Lee Kim degradation factor.....	72
5.2. TRACE Numerical Simulations Results	81
5.2.1. Single pipe results and comparison with analytical model	81
5.2.2. Loop simulation results	94
5.3. Limitations and Errors.....	99
5.4. Future Work	101
6. Conclusions	102
References	103

Figures

Figure 1.1 Market share of space heating in 2018 (Finnish Energy, 2021b).	13
Figure 1.2 District heating energy sources in 2020 (Finnish Energy, 2021b).	13
Figure 1.3 Flowchart of project work development.	15
Figure 2.1 LUTHER core design.	17
Figure 2.2 Simple scheme of LUTHER RHR closed loop.	18
Figure 2.3 Simple sketch of open containment cooling loop.	19
Figure 2.4 ABWR PCCS (Jeon et al., 2013a).	22
Figure 2.5 ESBWR PCCS (Silvonen, 2011).	23
Figure 2.6 Flow regimes during in-tube condensation.	26
Figure 2.7 Schematic illustration of thermal resistance during film condensation with NCG.	32
Figure 3.1 Radial cross section view for a buried pipe underground.	34
Figure 3.2 Schematic view for flow in the axial direction.	37
Figure 3.3 Illustration of main dominant regimes during in-tube condensation.	39
Figure 3.4 Scheme of sensible heat transfer balance.	42
Figure 3.5 MATLAB Calculation script for pure steam case.	50
Figure 3.6 Pipe cross section view illustrating flood angle.	52
Figure 3.7 MATLAB calculation procedure with NCG presence.	58
Figure 4.1 TRACE heat transfer regime selection logic for condensation, source TRACE Manual (USNRC, 2019, 278).	61
Figure 4.2 Single pipe TRACE input model.	64
Figure 4.3 TRACE input model for proposed LUTHER RHR loop.	66
Figure 5.1 Decay heat power and total steam mass flow rate over time.	68
Figure 5.2 Temperature across heat exchanger inlet and outlet over time.	69
Figure 5.3 Steam quality axial profile across condenser pipe for different times.	70
Figure 5.4 Fluid bulk temperature across condenser pipe for different times.	70
Figure 5.5 Ground HTC deterioration over time.	71
Figure 5.6 Theoretical model validation and mesh sensitivity study.	72
Figure 5.7 Top internal HTC axial profile for different (Steam +NCG) mixtures, 2 minutes after shutdown.	73
Figure 5.8 Bottom internal HTC axial profile for different (Steam +NCG) mixtures, 2 minutes after shutdown.	73
Figure 5.9 Axial profile of top radial heat flux for different (NCG + steam) mixtures, 2 minutes after shutdown.	75
Figure 5.10 Axial profile of bottom radial heat flux for different (Steam + NCG) mixtures, 2 minutes after shutdown.	75
Figure 5.11 Ground thermal resistance over time.	77
Figure 5.12 Thermal resistance profile across the top part of the tube for gas mixtures with varying NCG fractions, 2 minutes after shutdown.	78
Figure 5.13 Axial profile of top radial heat flux across a partial pipe length for a gas mixture with 80 % air at different time steps.	79
Figure 5.14 Axial profile of radial heat flux for top and bottom parts of the tube, 1hr after shutdown for a gas mixture with 80 % air.	79
Figure 5.15 Axial profile of inner wall temperature for top and bottom parts of the tube, 1 hr after shutdown.	80
Figure 5.16 Radial heat flux in the 1 st node over time, comparison of analytical and numerical results, 1 month simulation.	82
Figure 5.17 Axial profile of radial heat flux 1 hr after shutdown for partial length of the tube, comparison of analytical and numerical solutions.	84

Figure 5.18 Inner wall temperature over time in the 1 st node for numerical and analytical solutions.	84
Figure 5.19 Axial profile of inner wall temperature for analytical and numerical solutions.	85
Figure 5.20 Comparison of radial heat flux over time in the 1 st node for different ground materials.	86
Figure 5.21 Axial profile of radial flux for the initial part of the tube tested with different ground materials, 1 hr after shutdown.	87
Figure 5.22 Comparison of heat flux over time in the 1 st node for different saturation pressures. ...	88
Figure 5.23 Axial profile of radial heat flux for different saturation pressures 1 hr after shutdown.	88
Figure 5.24 Comparison of heat flux over time in the 1 st node for different inclination angles.	89
Figure 5.25 Comparison of heat flux over time in the 1 st node for varying (Steam + NCG) fractions with selected ground material soil (mixture).	90
Figure 5.26 Comparison of heat flux over time in the 1 st node for varying (Steam + NCG) fractions with selected ground material Finnish granite.	91
Figure 5.27 Axial profile of radial heat flux for initial partial length of the tube for different (Steam + NCG) mixtures 1 hr after shutdown, with selected ground material Finnish granite.	92
Figure 5.28 Reactor decay power and condenser heat removal rate over time.	94
Figure 5.29 Gas and liquid mass flows across condenser tubes over time.	95
Figure 5.30 Axial profile of gas and liquid mass flows across the condenser tubes, 1 hr after shutdown.	96
Figure 5.31 Condenser tubes inlet pressure over time.	97
Figure 5.32 Axial profile of radial heat flux across condenser tubes.	98
Figure 5.33 Temperature axial profile across condenser tubes, 1 hr after shutdown.	99

Tables

Table 2.1 Horizontal in-tube condensation HTC's used in the analysis.	29
Table 3.1 Design specifications.	33
Table 4.1 Thermophysical properties of different ground materials.	63
Table 5.1 Proposed GHE geometrical parameters based on pure steam model.	68
Table 5.2 Proposed GHE geometrical parameters based on TRACE solution.	94

1. Introduction

1.1. Background

In the current energy climate, the ever-increasing demand for energy across the world is met with a difficult challenge: How can we continue to increase global energy production while reducing carbon emissions? To remain in line with the Paris agreement, the answer is well established, countries must invest and expand on the development and deployment of carbon neutral energy sources.

In many countries where the long-term vision is to become a carbon-neutral society, strenuous efforts are being made to reduce the carbon footprint. In Finland, the electricity production is 85 % from carbon-neutral sources with nuclear energy contributing alone with a share of 27.7 %, hence yielding a grid among the cleanest in Europe with a carbon intensity of only 63 gCO₂/kWh(e) (Finnish Energy, 2021b).

Nevertheless, as decarbonisation across all industries becomes more of a necessity, different applications for the use of nuclear technology are being explored. District heating for instance is one of the main energy sectors which comprises 46 % of space heating market share (Figure 1.1). The sector remains with relatively high carbon emissions powered almost 50 % from fossil fuel (Figure 1.2), with the specific emissions of district heating in 2020 totalling 127 gCO₂/kWh (Finnish Energy, 2021a). Which raises the question: “what are the options for sustainable heat production in the future?”

To answer the question, several studies (Paiho & Reda, 2016; Paiho & Saastamoinen, 2018) looked into the development of district heating for the next decades. These studies show a potential market for the use of nuclear reactors in this sector.

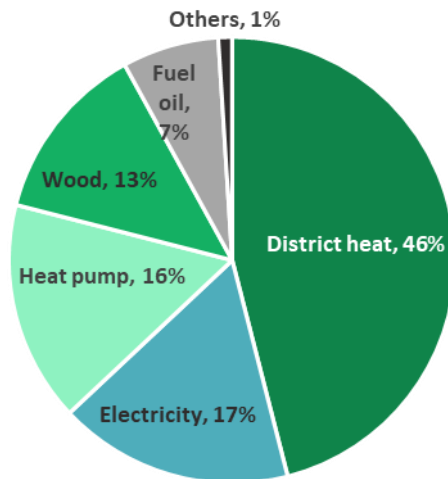


Figure 1.1 Market share of space heating in 2018 (Finnish Energy, 2021b).

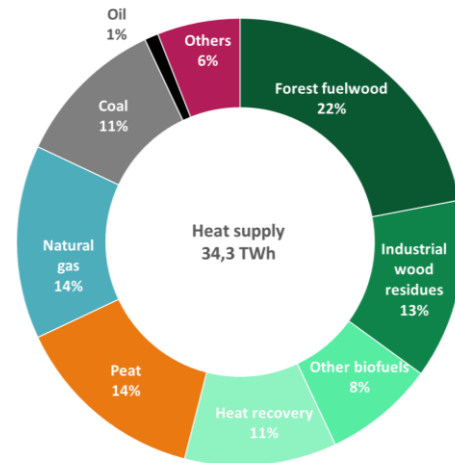


Figure 1.2 District heating energy sources in 2020 (Finnish Energy, 2021b).

Historically, the potential use of nuclear power in district heating has been considered since the seventies (Leppänen, 2021), but it was never realised due to legislative and economic reasons. However, as government policies changed in alignment with the energy transition strategy, the interest renewed in this technology. Some more recent preliminary techno-economic analyses (Leppänen, 2019, 2021; Tulkki et al., 2017; Värri & Syri, 2019) reviewed the feasibility of nuclear in district heating in the next 10-15 years. It was suggested in this literature that, nuclear power stands as a mature and economically viable option among carbon-neutral heating sources in future energy landscape. Consequently, this sparked the motivation at Lappeenranta University of Technology (LUT) for the development of the LUT Heating Experimental Reactor (LUTHER) of 6 MW_{th} and the commercialised version of 24 MW_{th} (Truong et al., 2021).

As part of the conceptual design, safety systems come at the heart of the design envelope. In nuclear reactors, decay heat is a major concern from a safety perspective. It is basically the heat produced by the decay of the radioactive fission products after the shutdown of the reactor. Therefore, it is vitally important to develop an adequate heat removal system for the proposed LUTHER reactor.

In this study, one of the options for the passive removal of decay heat power is studied, which is an innovative part of the design. The system is essentially a containment cooling loop that runs on natural circulation and transfers heat from the containment to the surrounding ground. The purpose of the system is to remove decay heat from the steam and

non-condensable gases (NCG) mixture in the containment via an underground pipe bundle condenser using the ground as a cold buffer. The heat is ultimately ejected to the atmosphere as a heat sink. Theoretically this should allow for the indefinite removal of decay heat via this mechanism.

1.2. Project Scope, Aim and Objectives

The scope of the work carried out in this report is to investigate the feasibility of removing decay heat via an underground loop using the ground material as a cold buffer. The study particularly reviews the effect of the presence of non-condensable gas which is air in this case on the heat transfer of the overall performance of the system.

Project aim:

The main aim is to propose preliminary design parameters for the piping lengths, diameters and number of parallel pipe network needed for adequate and reliable heat removal performance.

Thesis objectives:

- To research condensation in horizontal tubes with and without the presence of non-condensable gas, and critically review, understand, and describe a wide spectrum of theories and methods used in modelling the phenomena.
- To use engineering principles of heat and mass transfer to establish a theoretical framework for the design of an underground heat exchanger.
- To use thermal hydraulic system code for safety analyses of light water reactors (LWR) TRACE (USNRC, 2019), for the modelling and simulation of the proposed decay heat removal (DHR) system.
- To analyse, discuss and interpret obtained analytical and numerical simulation results to characterise the limiting factors in the heat transfer.
- To ultimately propose a preliminary optimal sizing and setting for the underground containment cooling design for LUTHER district heating reactor.

1.3. Methodology

This section outlines the methodology of the work carried out throughout the course of this thesis. The overall work is divided into five main stages as illustrated in Figure 1.3.

To start with, a thorough literature review was conducted to fully understand the condensation process and modelling methods used in heat exchanger designs. The review particularly focuses on passive safety systems in advanced light water reactors.

The following step was to set up a theoretical framework substantiated with relevant correlations and assumptions to carry out the analysis. Two theoretical models were created based on heat balance equation, momentum balance and continuity equation. The first model is for pure steam case to determine the geometrical and operational parameters of the heat exchanger. The second model was then established to examine the process more thoroughly with the presence of non-condensable gas and update the design accordingly.

Further on, numerical simulations using thermal hydraulic system code TRACE were performed to consolidate the findings from the theory and compare the results. Numerical studies are carried out for a single tube test as well as for the entire loop.

Finally, the results from both analytical and numerical studies are interpreted and limiting factors are discussed to determine the main key-findings of the analysis. The conclusion also highlights further suggestions for future work.



Figure 1.3 Flowchart of project work development.

2. Literature review

2.1. Small Modular Reactors

The Fukushima Daichi accident in 2011 was a historic event that changed the nuclear industry in many aspects. Technologically, research and development (R&D) focus shifted towards developing more robust, inherently safer designs relying more on passive safety. In the recent years, this has yielded a growing worldwide interest in the class of reactors that is known as Small Modular Reactors (SMRs). Reportedly offering additional safety, economic and technical advantages over large conventional Nuclear Power Plants (NPPs) (Locatelli, 2018). SMRs are set to be a potential game changer that could potentially revitalize the nuclear renaissance in the future energy landscape.

Small modular reactors are advanced fission reactors that produce a small power output less than 300 megawatts as classified by the International Atomic Energy Agency (IAEA, 2020). As compared with conventional reactors, the term modular in SMR refers to the scalability and the modularity of the systems components. Different parts and components could be manufactured in factories and assembled as multiple modules on site. Consequently, this allows the reduction of costs and make SMRs an attractive investment.

Various designs are being proposed around the world, ranging from: molten salt, high temperature gas cooled, lead cooled to super critical water cooled. Each offering a particular value for a specific use: power generation, desalination, district heating, industrial production (Locatelli et al., 2014) and even defence and space exploration (The White House, 2021). However, while most new technologies may require decades of R&D before hitting the market, the mature and proven technology of light water reactors such as Pressurised Water Reactor (PWR) has more potential to be deployed in the short-term future.

According to major developers in the nuclear arena, SMRs offers intrinsic safety features that could dramatically strengthen the nuclear safety case. Most new concepts aim to improve the overall safety of the plant by implementing innovative passive mechanisms as a mean of removing heat.

Description of LUTHER conceptual design

The LUT Heating Experimental Reactor (LUTHER) is a scalable light water pressure-channel reactor with a low power density. The design utilises light water as the moderator and the coolant. The core consists of fuel channels which enclose UO_2 fuel elements within pressure tubes, where the coolant circulates within these tubes at relatively low pressure and low temperature. In addition, these fuel channels are submerged in light water moderator in the calandria tank. The containment is made of reinforced concrete fully located underground and the reactor is to be manufactured by the Finnish industry. (Truong et al., 2021).

The design could be scaled up from 6 to 24 MWth. Figure 2.1 highlights the structure of the core which consists of 61 fuel channels, of which only 37 are needed for 6 MWth power generation and 61 for 24 MWth nominal power.

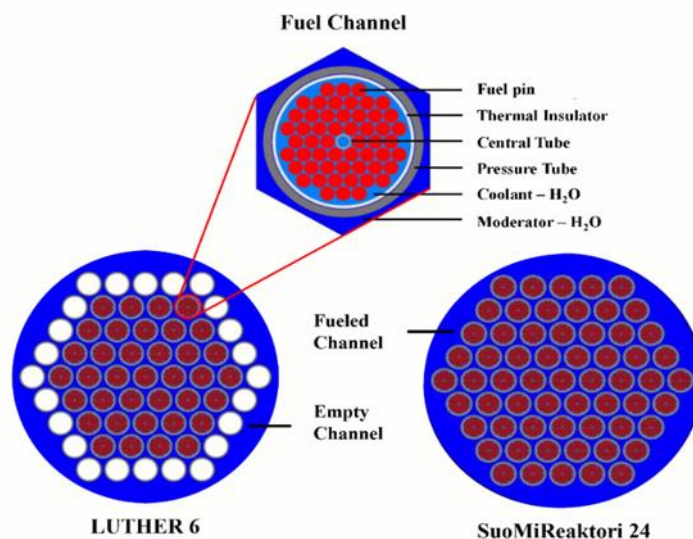


Figure 2.1 LUTHER core design.

For cooling, there are essentially three loops: the reactor primary loop, the intermediate loop, and the district heating network. The primary circuit is totally inside the containment: 0.2 MPa pressure, inlet temperature of 100 °C and outlet temperature of 120 °C, which is coupled to the intermediate loop that transfers heat to the district heating network. In the district heating loop pressure ranges from 0.6 to 1.6 MPa, the delivery temperature range 40 to 95 °C, and return temperature 20 to 60 °C. (Hyvärinen & Truong, 2020).

The LUTHER reactor is an advanced conceptual design that uses innovative safety systems. Unlike traditional designs, the reactor is to be located underground which requires the development and incorporation of innovative means to remove heat passively. Two different cooling loops are currently under consideration for the development of LUTHER Residual Heat removal (RHR) systems: One closed loop (Figure 2.2) directly connected to the reactor and another directly to the containment (Figure 2.3), similar to the Isolation Condenser and Passive Containment Condensers in modern Boiling Water Reactors (BWRs). The reactor loop might contain either single-phase coolant in the case of intact reactor or steam in the case of a postulated event leading to a broken reactor. Non-condensable gases could be present in the reactor loop, due to radiolysis in the reactor, but their volume fraction should be fairly small.

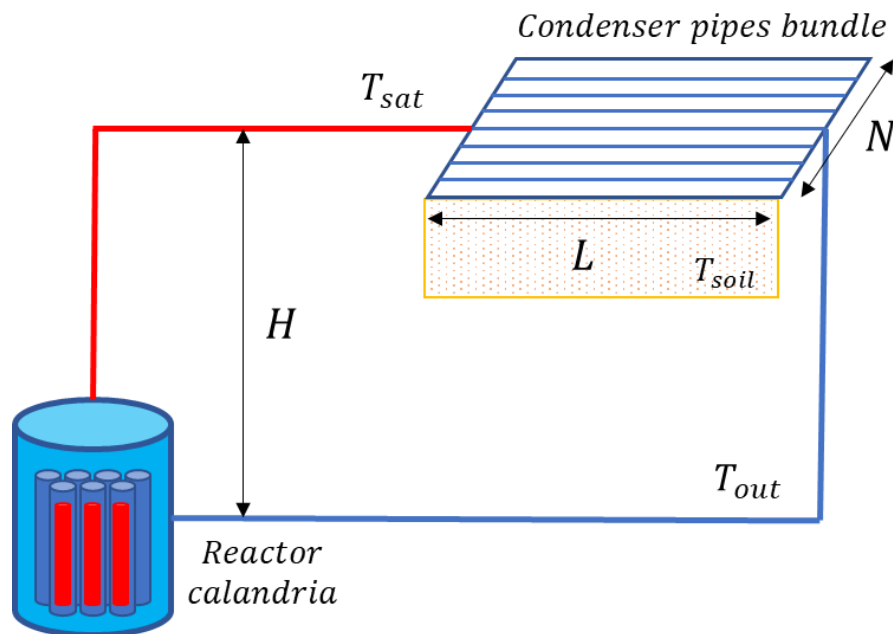


Figure 2.2 Simple scheme of LUTHER RHR closed loop.

The containment loop on the other hand would need to condense steam from a steam-air mixture using the ground as a buffer. Since the containment is usually filled with air, there will be significant amounts of NCG circulating in the cooling loop in addition to the steam from the reactor.

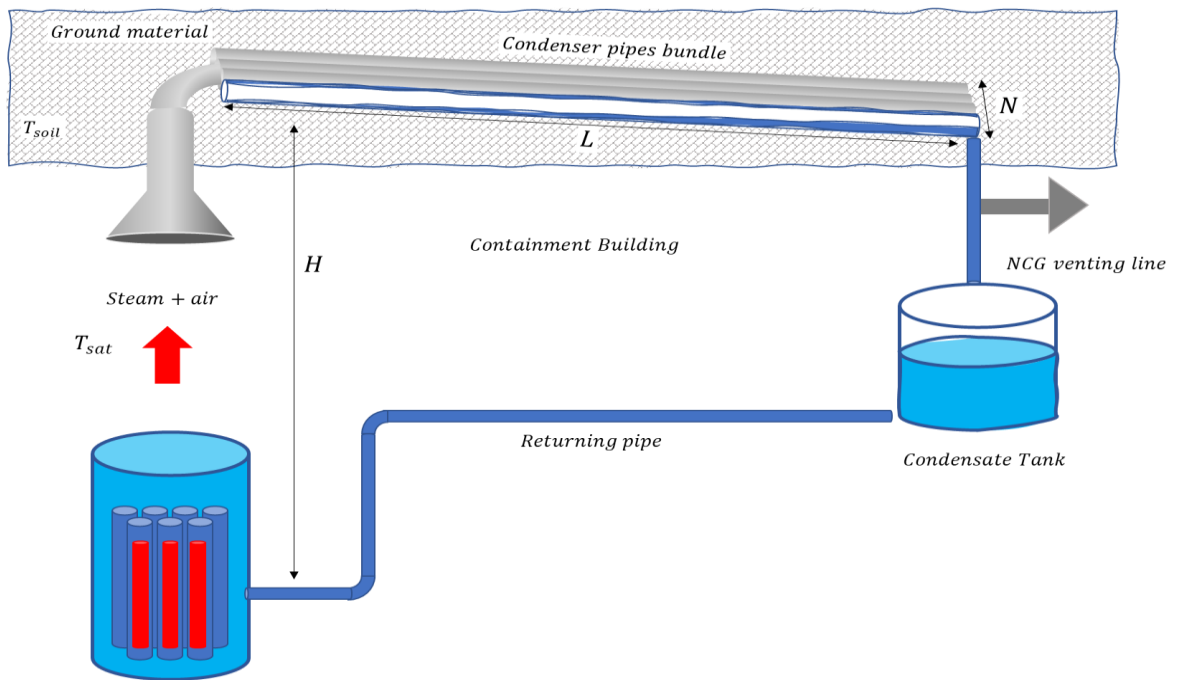


Figure 2.3 Simple sketch of open containment cooling loop.

The decay heat after shutdown is main source of power under these circumstances, which is calculated using the Wigner-Way formula:

$$P_d(t) = 0.0622P_o[t^{-0.2} - (t_o + t)^{-0.2}] \quad (2.1)$$

$P_d(t)$ = thermal power generation due to beta and gamma rays,

P_o = thermal power before shutdown,

t_o = time, in seconds, of thermal power level before shutdown which is assumed to be the duration of one cycle estimated at 9 months.

t = time, in seconds, elapsed since shutdown.

2.2. Passive Systems and Natural Circulation

Passive safety is a design approach in advanced nuclear reactors that aims to eliminate the dependence of systems on active components to a certain degree. As defined by the IAEA, passive safety systems in nuclear reactors are systems that operate in a manner that is independent of mechanical, electrical power supply and control instrumentations input or signal. The systems reliance is instead placed on natural laws, properties of materials and internally stored energy (IAEA, 1991). Furthermore, the concept of passivity is classified into several degrees.

Natural circulation is a fundamental working principle that underpins several passive safety systems. Since the phenomenon relies on nature forces with no need of pumps, it allows for the development of cooling systems that are intrinsically safer and simpler. This simplification of the system results in a reduction of costs as well as a significant improvement in the system reliability.

Traditionally, natural circulation loops have been used since first generations of nuclear power plants. Most popular application was the removal of decay heat system; as well as within steam generators operation in some designs (Vijayan et al, 2019, 41-68). However, their use was quite limited. It was post Fukushima aftermath that more research has been conducted in different facilities around the world, to better understand the mechanistic of the phenomenon for the development of innovative passive safety systems. With some new reactors nowadays designed with natural circulation being the primary mode of core cooling during normal operation, such us the Economic Simplified Boiling Water Reactor (ESBWR) (Shiralkar et al., 2007) and NuScale design.

2.2.1. Passive Containment Cooling Systems

The containment is an important safety barrier within the defence in depth concept. Containment plays an important role in mitigating the consequences in the event of Loss of Coolant Accident (LOCA), main steam line break (MSLB) and many other faults in conventional reactors. It also serves the purpose of the removal of decay heat ejected to the air. Without an effective heat removal system, pressure and temperature within the

containment may exceed the allowed maximum value as per regulations, compromising the containment integrity and consequently the safety of the reactor overall.

In the past, containments have been cooled using spray systems or fan coolers system (Bai et al., 2018) but since this equipment rely on power, passive systems can be made even more reliable. Fukushima accident showed that active components susceptibility to common cause failure in the event of station blackout could significantly deteriorate the safety functions. As a result, almost all new advanced light water reactors are designed with a Passive Containment Cooling System (PCCS) in one way or another.

PCCS is essentially a safety equipment that is used to eject decay heat from inside the containment to the environment without an external power supply (Ha et al., 2017). It was first incorporated in third generation innovative NPPs (Chen et al., 2021). The system design is independent of mechanical, electrical instrumentation and control systems. PCCS systems usually rely on natural forces or phenomena such as gravity, pressure difference, natural heat convection or natural circulation. This ensures the integrity of the containment and mitigate the effect of several design-basis and beyond design-basis scenarios.

Most recent licensed reactors such as the AP1000, AP600 and VVER-1200, in addition to the ESBWR, all incorporate a PCCS system. The containment cooling designs differ in certain aspects, but they all run on natural force principles. The AP1000 has a stainless-steel containment with good thermal conductivity allowing for the design to cool the external surface of the steel containment by spraying water passively from the water tank at the top of the containment. On the other hand, the other designs have a concrete containment which is known for a relatively poor heat conductivity and therefore the design is different (Bae et al., 2020). The VVER-1200 for example installs a heat exchanger at the inside of the containment passively supplying the cooling water (Bang et al., 2021).

Moreover, in the Advanced Boiling Water Reactor (ABWR), the PCCS shown in Figure 2.4 incorporates a horizontal heat exchanger that is submerged in a pool of water located outside the containment. As the steam is generated in the dry well, it flows through the PCCS with non-condensable gases where the steam ejects heat in the pool that is filled with cold water and condenses. The condensate is then returned to suppression pool wet well by gravity and pressure difference. The overall natural circulation flow is driven by the water head difference between the two elevations (Jeon et al., 2013a).

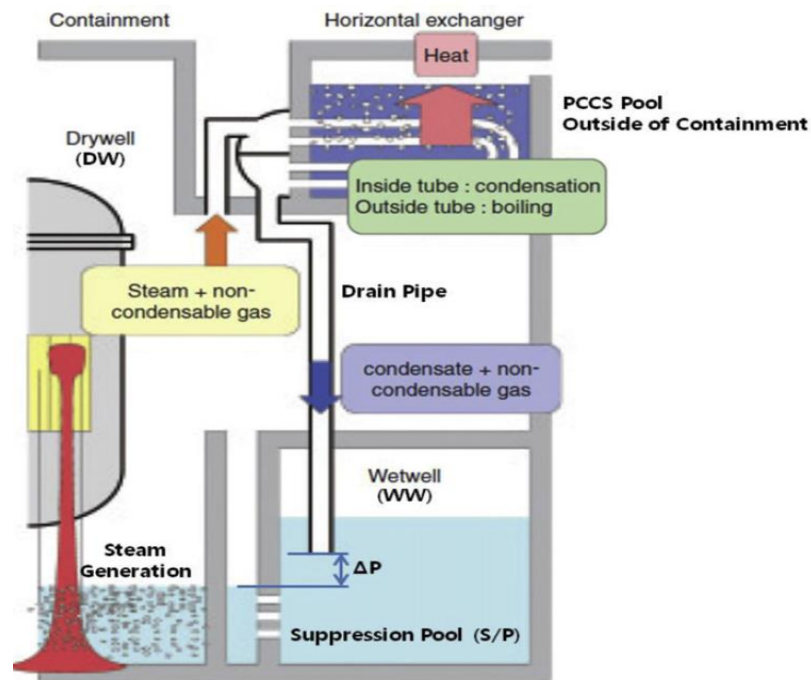


Figure 2.4 ABWR PCCS (Jeon et al., 2013a).

Similarly, the ESBWR employs a similar design but with slightly more advanced features, the condensing chamber pool is located within the containment and the non-condensable gases are separated from the condensate and returned separately to different pools as shown in Figure 2.5.

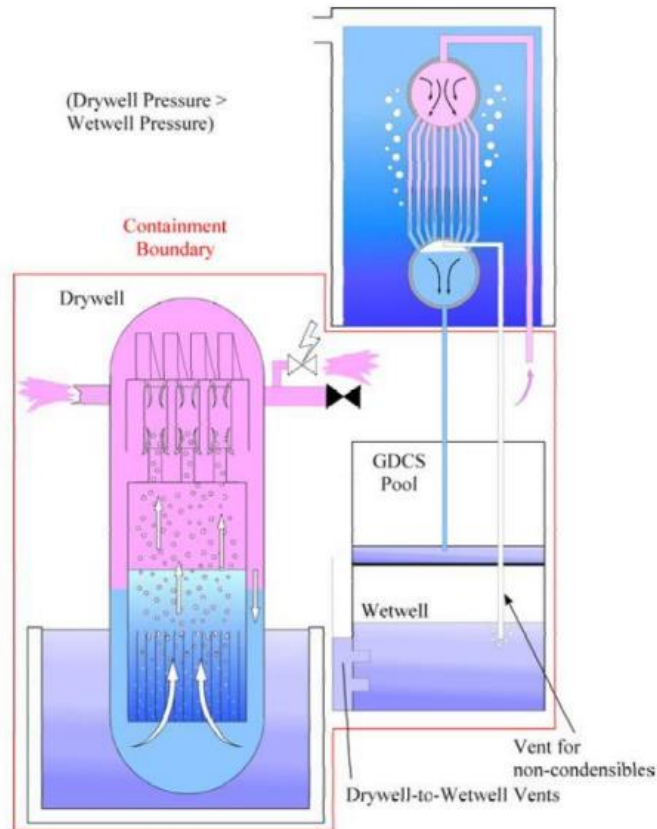


Figure 2.5 ESBWR PCCS (Silvonen, 2011).

Additionally, various other residual heat removal systems designs for SMRs use cooling towers employing the atmosphere as an ultimate heat sink (Ayhan & Sökmen, 2016; Na et al., 2020). However, RHR systems using the ground as an intermediate heat sink, there is not much in the open literature, only a few studies can be found for some theoretical designs (Sambuu & Obara, 2015).

Lastly, it is worth noting that most current traditional containment cooling systems employ a vertical condenser. Nevertheless, advanced designs under development, most incorporate a horizontal heat exchanger design. A Horizontal condenser is believed to have a higher heat removal capability. Also horizontal tubes have less fouling, higher earthquake resistance as well as an economic benefit as it allows the reduction of containment height and volume (Lee & Kim, 2011).

2.3. Condensation

Steam condensation is one of the most common phenomena encountered in many industrial applications in power plants. The mechanism underpins many passive safety systems in modern nuclear reactors due to its large heat removal capacity. The process is complicated to model analytically and various theoretical studies, semi empirical models as well as empirical correlations have been proposed for the prediction of heat transfer. Overall, there is not a single universal model that could be utilized under varying conditions.

Different models have been suggested for different configurations of flows and under various conditions (diameters range, flow velocity, fluid type, pressure.... etc). Even under the same conditions, discrepancies have been reported from one study to another (Jeon et al., 2013a).

Within the available literature, condensation has been investigated extensively for different settings: Flow on the outside of tubes, over a flat plate and internal flows in vertical and horizontal orientations. But, unlike vertical direction, studies on horizontal direction tend to be rather scarcer. There is not a wealth of literature for horizontal in-tube condensation (Garimella & Fronk, 2015).

2.3.1. Flow pattern maps

Predicting the two-phase flow morphology is crucial in heat transfer calculations because different flow regimes result in varying heat transfer coefficients and condensation rates. During film condensation inside tubes, different flow regimes are observed which depend on several factors: flow velocity, quality, void fraction (Garimella & Fronk, 2015) as well as the configuration and the dimensions of the tube, the heat flux, the mass flux, pressure and the fluid properties (Liebenberg & Meyer, 2006). Flow patterns along the length of the pipe could significantly change the heat and momentum transfer (Dobson & Chato, 1998), therefore it is important to determine the prevailing flow regime for the main part of the tube in order to calculate the in-tube heat transfer coefficient and the pressure drop with a good confidence (Liebenberg & Meyer, 2006).

Flow pattern maps are often used to describe two-phase flow inside tubes. The Baker map (1954) was the first universal flow pattern map for horizontal two-phase gas-liquid flow. However, there were different inconsistencies reported in several studies later for the use of the Baker map, mainly the diameter had huge influence on the applicability of this map (Shabestary et al., 2019). Several other maps were created in the following years, Medhan et al map 1974 is one of the mostly used maps for general purpose up to this day (Thome & Cioncolini, 2015). Nevertheless, most of these maps were developed based on empirical data which limited the range of applicability.

Based on mechanistic considerations, Taitel and Dukler in 1976 created a new flow pattern map that does not really depend on empirical data unlike all other maps. They defined five dimensionless groups that correspond to fluid dynamic parameters, tube geometry, and tube inclination angle. The flow map depicts annular flow, stratified wavy flow, stratified smooth flow, intermittent flow, and bubbly flow. This map is one of the most reliable and widely used flow maps, and it has served as a foundation for the development of more recent modern flow pattern maps.

It is worth noting that most previously mentioned maps are adiabatic maps for two-phase general-purpose flow that were mostly developed for air/water mixtures, they do not take into account the condensation characteristics (Garimella & Fronk, 2015). (Breber, 1980) proposed the first map specifically for condensation for multiple fluids, then (Tandon et al, 1982) followed on the same footsteps. Many more maps and models followed later.

From a practical point of view, the distinguishing between flow structures/regimes for condensation is only useful when the heat transfer mechanism varies considerably, therefore the most important regimes during horizontal condensation are mist, annular and stratified-wavy (Garimella & Fronk, 2015).

2.3.2. Condensation inside horizontal pipes

Condensation inside horizontal tubes is a rather more complex phenomenon compared to the unconfined external condensation. (Liebenberg & Meyer, 2006). This is due to the different dynamics of the vapour and condensate that occur simultaneously, in addition to the phase change process. Horizontal condensation is characterized by strong asymmetry and flow regime transitions, making it a bit more challenging to predict compared to vertical condensation.

As saturated vapour flows into a tube with lower walls temperature, some of the vapour condenses on the inner sides of the tube walls and forms a condensate film. This liquid film covering the cooled surface represents the bulk resistance to the heat transfer. In horizontal configuration, there are two forces that act on this film and the gas flow : gravitational force and vapour convective shear effect across the interface (Jeon et al., 2013a). The effect of each force depends on the mass flux value, and the balance between the two forces determines the dominating flow regime.

Essentially, there are two primary modes for horizontal in tube condensation, they are usually categorised depending on the velocity of the vapour: *laminar film condensation and forced convective condensation* which are illustrated in Figure 2.6 as depicted by (Palen et al., 1979). Forced convective condensation refers to high flux flow in the presence of a pressure gradient usually. On the other hand, film condensation refers to low mass flux or low vapour velocity (Liebenberg & Meyer, 2006).

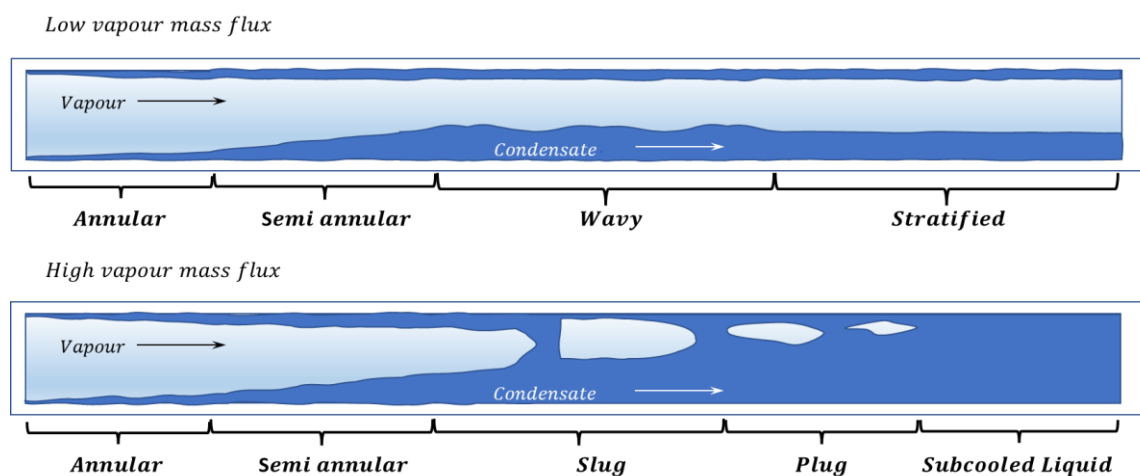


Figure 2.6 Flow regimes during in-tube condensation.

At high mass fluxes, the inertial forces dominate, making the effect of gravity insignificant, hence resulting in a more symmetrical pattern where the annular pattern prevails for a great section of the tube. Slug flow is then encountered, then plug flow, and eventually all the vapor is converted to liquid (Figure 2.6). Slug, plug, and bubbly flow all together account for only 10–20 % of the whole quality range. The plug and bubbly flow regimes are limited to the vapor quality range's bottom 1–2 % (Dobson & Chato, 1998). Since shear forces dominate heat transfer in this flow regime, larger mass fluxes will tend to enhance the heat transfer coefficient via two different mechanisms: relatively high vapours velocity will entrain droplets from the film into the vapour core, keeping the condensate film constantly thinner and hence less resistance to the heat transfer. Also, the high flow rates shear will create interfacial waves across the films which increase the heat transfer (Garimella & Fronk, 2015).

On the other hand, at low mass fluxes, gravitational forces dominate the flow field. A laminar film condensate is formed along the tube walls, it accumulates from the top wall of the tube towards the bottom and flows downstream, forming a relatively thicker liquid film at the bottom (Figure 2.6). In some studies, it was reported that the thickness of the film at the bottom is 100 times more than at the top (Thome & Cioncolini, 2015).

Because of this thicker film, the heat transfer through the bottom part of the tube is usually negligible, making most heat transfer across the top part of the wall sides where the film is relatively thinner (Chato, 1962). In this case, the vapour may not fully condense, and some vapour may even escape uncondensed due to lack of mixing and turbulence (Garimella & Fronk, 2015).

(Rifert & Sereda, 2019) lists all experimental work that has been carried out for condensation inside tubes for low and high vapour velocities. Examining experimental values of condensation heat transfer coefficients (HTCs) in these studies, clearly demonstrates that heat transfer behaviour differs considerably between the primary flow regimes, and they should always be treated differently. Usually, the regimes considered are either annular for shear dominated flows or stratified for gravitational dominated flows. Hence, the same approach is adopted in the development of the analytical models in the following sections.

2.3.3. Heat transfer calculations

For heat transfer calculations dealing with in-tube condensation, the available work in the literature could be categorised depending on the studied flow regime, mainly: annular and stratified-wavy (Jeon et al., 2013a). For the annular flow, the models are classified into three types: shear-based models, boundary-layer models, and two-phase multiplier models (Dobson & Chato, 1998).

Among the earliest models developed for steam condensation is the Nusselt model in 1917, who is considered a pioneer in this area (M. Ghiaasiaan, 2017). Nusselt studied condensation in a range of pipe configurations: Flow on the outside of tubes, over a flat plate and internal flows. His work is considered the foundation for many other works developed later.

Several correlations have been proposed for in-tube horizontal tubes over the years. Perhaps one of the earliest models is Akers and Rosson (1960). They studied condensation for refrigerants with a model of Reynolds number and they dealt with both mechanisms of condensation, annular and stratified. Then later (Chato, 1962) focused his studies on low velocity condensation where he developed a model that is considered a slight Nusselt modification. In this model the heat transfer is more considerable in the upper part of the pipe.

Additionally, (Shah, 1979) is also one of the widely used and recommended correlations in the literature, it is a two phase multiplier model and adopted for the use in some well-known thermal hydraulic codes like RELAP5 and MARS (Jeon et al., 2013b).

(Dobson & Chato, 1998) then improved the initial model of Chato and developed an improved flow map. They considered the bottom part of the film in the heat transfer which was ignored in (Chato, 1962) early model. This proved to have some significance in the case of vapour with high velocity (Jeon et al., 2013a).

Then (Cavallini et al., 2002) study was one of the main studies that achieved significant improvement in this field. They developed a new map for condensation flow and a model for pressure drop and heat transfer coefficient. The model was later further updated (Cavallini et al., 2006).

Lastly, it is necessary to keep in mind that when selecting a correlation, it is important to select one whose parameters fit within the range of applicability for which the original model

was developed. Especially for parameters such as the diameter and fluid in question, these have been reported to affect the results significantly when correlation was applied outside the applicability range (Garimella & Fronk, 2015).

Table 2.1 Horizontal in-tube condensation HTC's used in the analysis.

Model	Correlation	Annular/stratified	Applicability range
Shah 1979	$H = 0.023 Re_L^{0.8} Pr_L^{0.4} \left[1 + \frac{3.8}{Pr^{0.38}} \left(\frac{x}{1-x} \right)^{0.76} \right] \left(\frac{k_L}{D} \right)$	No account of flow regimes	$7 \leq D_h \leq 40\text{mm}$ $10 < G < 20 \text{ kg/m}^2\text{-s}$
Chato 1962	$H = 0.725 \left[\frac{\rho_L(\rho_L - \rho_V) h_{fg} g D^3}{k_L \mu_L (T_{sat} - T_w)} \right]^{1/4} \left(\frac{k_L}{D} \right)$	stratified	for $Re_V < 35,000$.

2.3.4. Pressure drop

For naturally circulating flows, it is crucially important to predict pressure drop across the loop with a good confidence to ensure that the driving force is maintained. While the driving force is generated by the temperature difference which consequently create a density difference stimulating the buoyancy effect. Parasitic losses on the other hand are attributed to frictional and form forces throughout the pipes system. From a heat transfer standpoint, determining the pressure drop is as equally important as the heat transfer calculations since the two are strongly coupled (Garimella & Fronk, 2015).

Generally, the overall pressure gradient of a condensing flow across a pipe system is composed of the following pressure gradients: the frictional pressure gradient (f), hydrostatic head (g) and spatial fluid deceleration (a, due to condensation) which is caused by change in fluid momentum and temporal mixture acceleration (Garimella & Fronk, 2015).

$$\left(-\frac{dP}{dz} \right)_T = \left(-\frac{dP}{dz} \right)_f + \left(-\frac{dP}{dz} \right)_g + \left(-\frac{dP}{dz} \right)_a \quad (2.2)$$

Within a naturally circulating loop, two parameters are important: the height available and the parasitic losses due to frictional forces. It is also worth mentioning that when significant phase change is present, then the acceleration/deceleration due to density change also becomes significant.

The frictional pressure drop across a condensing flow in a tube is attributed to two main mechanisms: the tube wall friction and the two-phase interface shear.

The concept of phase multiplier is used in condensation pressure drop calculations. There are several empirical and semi-empirical correlations, as well as analytical formulas that have been proposed for the phase multiplier. The multipliers are separately defined for homogeneous and for separate flow models.

Homogenous

In the homogenous model, the two phases are assumed to have the same velocity with no slip. The phase multiplier ϕ_{i0}^2 is a function of the steam quality and is given from reference (M. Ghiaasiaan, 2017) as:

$$\Phi_{i0}^2 = \left[1 + x \frac{\mu_L - \mu_G}{\mu_G} \right]^{-\frac{1}{4}} \left[1 + x \left(\frac{\rho_L}{\rho_G} - 1 \right) \right] \quad (2.3)$$

It should be noted that most of the available correlations for the phase multipliers in the literature are provided for adiabatic flows where the phase quality is constant. However, since the steam quality is changing in this case, the pressure drop can be calculated numerically in a stepwise approach.

Alternatively, with a few simplifying assumptions (dx/dL is constant), we could also perform the integration analytically to obtain the pressure via the following formula which is proposed for boiling flow in (M. Ghiaasiaan, 2017):

$$\Delta P_{fr} = \left(-\frac{\partial P}{\partial z} \right)_{fr,f0} \int_0^x \Phi_{f0}^2(x) dz = \left(-\frac{\partial P}{\partial z} \right)_{fr,f0} \frac{L}{x} \int_0^x \Phi_{f0}^2(x) dx \quad (2.4)$$

Although the integral provided from $x=0$ to $x=1$ which is for boiling, mathematically speaking, the integral for condensation will have the same value.

$$\frac{L}{0-x} \int_x^0 \Phi_{f0}^2(x) dx = \frac{L}{x} \int_0^x \Phi_{f0}^2(x) dx \quad (2.5)$$

Using the frictional multiplier for the homogeneous model, and assuming a linear change, one can obtain the following formula, which is suggested in (Collier & Thome, 1994, 46) for the homogenous model:

$$\Delta p = \frac{2f_{TP}LG^2v_f}{D} \left[1 + \frac{x}{2} \left(\frac{v_{fg}}{v_f} \right) \right] \quad (2.6)$$

Where f_{TP} is calculated by Blasius's correlation (M. Ghiaasiaan, 2017).

Separate flow models

Separate flow models are more realistic in modelling two phase flows encountered in nature and industrial applications. Most of the work developed has been empirical in this field.

(Martinelli & Nelson, 1948) pioneered this approach. They proposed the phase multiplier as a correlation between the two-phase frictional pressure drop and the frictional drop of the flow being either entirely liquid or vapour.

$$\left(-\frac{dP}{dz}\right)_{TP} = \Phi_L^2 \left(-\frac{dP}{dz}\right)_L \quad (2.7)$$

They proposed the Martinelli parameter, which is the square root of ratio of pressure drop from all flow being liquid over pressure drop of all flow being vapour.

$$X^2 = \frac{\left(-\frac{dP}{dz}\right)_L}{\left(-\frac{dP}{dz}\right)_V} \quad (2.8)$$

While useful as an introduction, the Martinelli's approach suffers from different limitations and discontinuities in the applicability range. Nonetheless, the Lockhart–Martinelli two-phase multiplier served as the foundation for several models developed later for condensation. Alternatively, (Friedel, 1979) two-phase multiplier is one of the most often employed. Over 25,000 data points were used to formulate this empirical correlation. (Garimella & Fronk, 2015).

2.3.5. Effect of non-condensable gas

One of the main important factors that affect the heat exchange is the presence of non-condensable gases. Condensation in the presence of NCG is a far complex phenomenon than pure steam condensation, and the effect varies depending on how much of it is present in the system (Collier & Thome, 1994). The existence of NCG in condensing mixtures has been shown to drastically reduce the heat transfer, making it a primary concern for all passive safety systems. Therefore, it is of great importance to thoroughly and carefully use a model that could adequately predict the behaviour of such phenomenon.

Othmer (1929) conducted one of the earliest experimental investigations into the subject, using steam–air mixtures in a vertical copper tube with a 7.62-cm diameter. In the presence of only 0.5 percent air in the inlet steam, he observed a 50 % reduction in heat transfer as a result (M. Ghiaasiaan, 2017). Several experimental and theoretical studies were performed to investigate the effect of non-condensable gases, they are mostly all listed in (Huang et al., 2015) and (Rifert & Sereda, 2019). According to (Ren et al., 2015), studies for condensation in the presence of NCG are generally very scarce. However, whereas studies of this phenomenon in vertical tubes are more prevalent, investigations in horizontal tubes are even rarer. It is only recently that more research has been carried out in this field due to the growing interest in the development of passive systems.

The influence of the non-condensable gas should be less significant in forced flow condensation since there is greater mixing, which brings the steam more in contact with the condensate film, improving the condensation process (Sparrow et al., 1967). As in contrast to the case of stagnant or very low vapour velocity, where the NCG accumulates at the bottom due to the density difference, forming a boundary layer at the interface between film–gas that adds an additional thermal resistance (Figure 2.7). The mixing effect is not observed in passive containment cooling systems since the experimental data indicate that for most, if not all of PCCS operating conditions, the condensate film is laminar (Kuhn et al., 1997). As a result, in most typical containment cooling systems, the influence of NCG becomes very considerable and necessitates careful investigation.

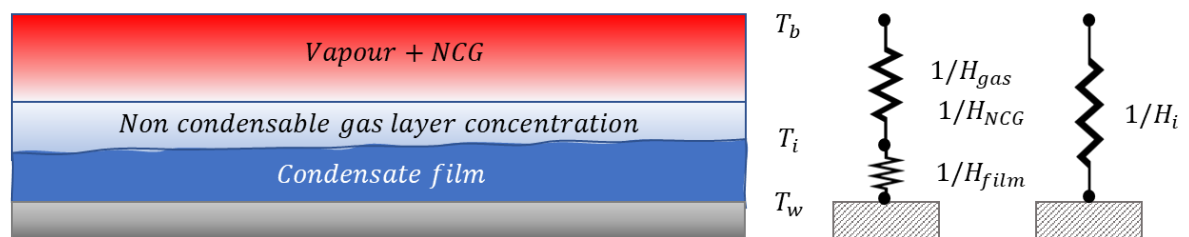


Figure 2.7 Schematic illustration of thermal resistance during film condensation with NCG.

3. Theoretical Framework/Analytical Study

In this chapter, the theoretical framework for carrying out the analysis is established. Two models are presented, each with corresponding theory and balance equations as well as assumptions embedded. In the first section, the basic theory for global heat transfer and pressure drop are presented to determine the geometric and operational design parameters for the decay heat removal system. The initial proposed geometry is based on the case of pure steam.

In the second section, a more detailed approach is adopted to examine the performance of the initially proposed system with consideration of the effect of non-condensable gases in the system. The second model calculates the local heat transfer parameters. The system's geometry is then updated accordingly. Table 3.1 outlines the design specifications of the system.

Table 3.1 Design specifications.

Design specification	Parameters
Reactor power	24 MWth nominal power
Elevation	6 m
Heat exchanger heat removal capacity	Removal of decay heat (2 % nominal power)
Pressure	2 bar
Steam saturation temperature	120 °C

Assumptions

The following assumptions are considered in the analysis:

- We assume steady-state heat transfer analysis
- Heat losses in the connecting piping of primary systems are negligible
- Axial conduction in the condenser pipes bundle is negligible
- Pressure remains constant during condensation within the closed loop (2 bar)
- Condensation happens at a constant temperature (saturation temperature at system pressure) inside the tube and cooling only starts after the whole flow condenses when quality $x = 0$

3.1. Pure Steam Case Model

3.1.1. Heat transfer calculations

The heat transfer balance equations are set up in this section, initially in the radial direction and then in the axial direction.

Radial direction

First, the heat balance across the different interfaces is set up, Figure 3.1 illustrates the interfaces across which the heat flux flows for a pipe buried underground.

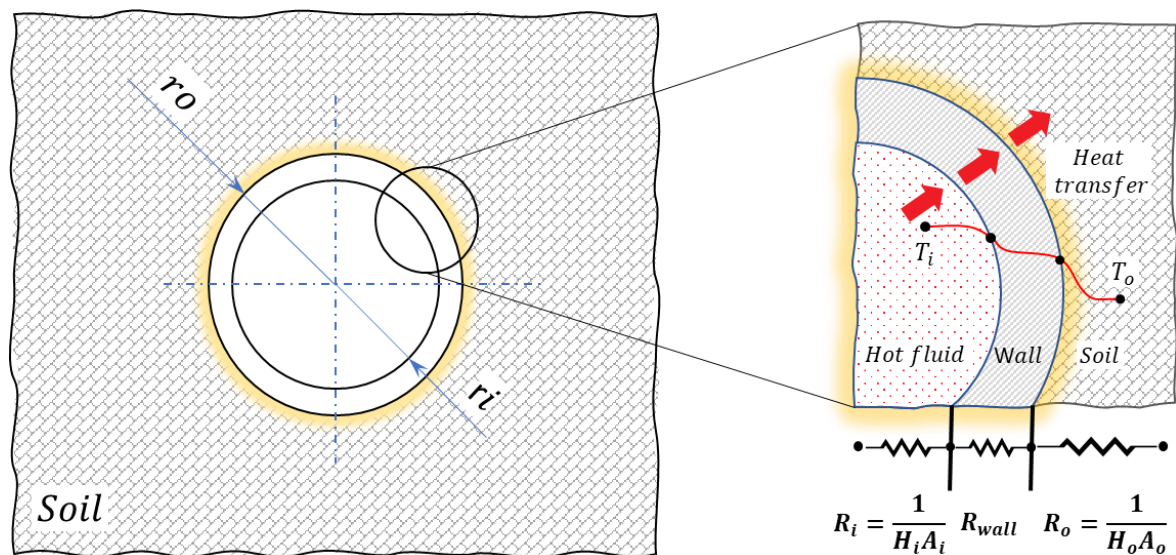


Figure 3.1 Radial cross section view for a buried pipe underground.

By establishing the very basic heat fluxes in the system per unit length:

The heat transfer from the hot fluid inside the pipe to the pipe inner wall:

$$q' = H_i 2\pi r_i (T_{vapour} - T_{pipe\ inner\ surface}) \quad (3.1)$$

q' is linear heat flux [W/m]

H_i is the internal heat transfer coefficient. It accounts for the heat transfer via convection and conduction as well as the thermal resistance introduced by the forming condensate film along the pipe wall.

r_i is the inner radius of the pipe.

The heat transfer across the pipe wall via conduction:

$$q' = \frac{2\pi k_p}{\ln(r_o/r_i)} (T_{pipe\ inner\ surface} - T_{pipe\ outside\ surface}) \quad (3.2)$$

k_p is the thermal conductivity of the pipe wall material.

r_o is the outer radius of the pipe.

Heat transfer via conduction from the pipe outer surface through to the surrounding ground:

$$q' = H_o 2\pi r_o (T_{pipe\ outside\ surface} - T_{ground}) \quad (3.3)$$

H_o is the outer heat transfer coefficient of the surrounding ground.

r_o is the outer radius of the pipe.

By rearranging these three equations (3.1), (3.2) and (3.3) and adding them all up we obtain

$$q' \left(\frac{1}{H_i} + \frac{\ln(r_o/r_i)(r_i)}{k_p} + \frac{r_i}{H_o r_o} \right) = 2\pi r_i (T_{hot\ fluid} - T_{ground}) \quad (3.4)$$

The overall thermal resistance is taken as:

$$R_{tot} = \frac{1}{H_i} + \frac{\ln(r_o/r_i)(r_i)}{k_p} + \frac{r_i}{H_o r_o} \quad (3.5)$$

The following expression, gives the ground effective heat transfer coefficient which is provided by the course guidelines (Hyvärinen, 2020):

$$H_o = \frac{k}{\sqrt{\pi a t}} \quad (3.6)$$

k is the thermal conductivity of the surrounding material of the ground,

t is the time,

a is the ground thermal diffusivity and it is given as:

$$a = \frac{k_g}{\rho c_p} \quad (3.7)$$

c_p is the specific heat capacity of the ground material,

ρ is the density of the ground material,

k is the thermal conductivity of the ground material.

It should be noted that these material properties will differ depending on the chosen ground material in the study. Depending on the depth and the geological location, the material could range from wet or dry soil, gravel or sand, or crystalline rock. For this model, the material chosen is soil (mixture). The material properties used are from (Zohuri & McDaniel, 2019).

The heat transfer balance equation (3.4) becomes:

$$q' R_{tot} = 2\pi r_i (T_{hot\ fluid} - T_{ground}) \quad (3.8)$$

$$q' = \frac{2\pi r_i}{R_{tot}} (T_{hot\ fluid} - T_{ground}) \quad (3.9)$$

$$q' = \frac{2\pi r_i}{R_{tot}} \Delta T \quad (3.10)$$

By substituting partially, the constant part of the thermal resistance by R (3.11) (excluding the internal HTC resistance) in (3.5)

$$R = \frac{\ln(r_o/r_i)(r_i)}{k_p} + \frac{r_i}{H_o r_o} \quad (3.11)$$

The heat equation (3.10) becomes:

$$q' \left(\frac{1}{H_i} + R \right) = 2\pi r_i \Delta T \quad (3.12)$$

Axial direction

In the axial direction, the pipe is essentially divided into two parts, two heat balance equations are set up accordingly. In the first part, condensation is taking place and therefore the latent heat transfer is considered. In the second part, after all the steam condenses, the condensate is being cooled down and therefore the sensible heat transfer balance is set up.

Condensation (latent heat transfer)

In the longitudinal direction of the pipe, we set up the thermal energy microbalance for a finite control volume of the pipe as illustrated in Figure 3.2. Starting by the generic energy balance equation per unit length:

$$\frac{dE}{dl} = in - out + production - dissipation \quad (3.13)$$

$$\frac{dE}{dl} = q_{min} h_{in} - q_{mout} h_{out} - q \quad (3.14)$$

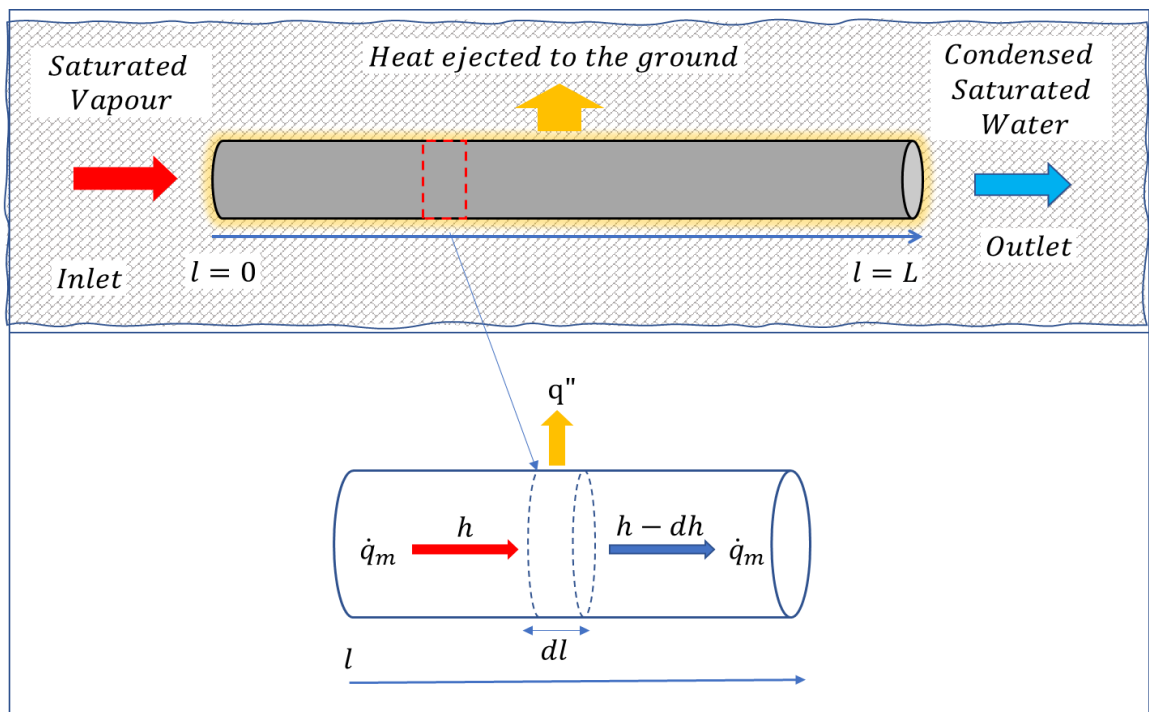


Figure 3.2 Schematic view for flow in the axial direction.

By applying the steady state condition and assuming the energy change is due to the enthalpy change in the finite control volume, and the mass flow rate is constant (Figure 3.2), the following expression is obtained:

$$q_m dh = -q' dl \quad (3.15)$$

q_m is the mass flow rate in the pipe [kg/s]

q' is the linear heat flux [W/m]

dh is the enthalpy difference [J/kg]

By replacing the linear heat flux in the balance equation (3.15) by its expression (3.10), we get:

$$q_m dh = -\frac{2\pi r_i}{R_{tot}} \Delta T dl \quad (3.16)$$

$$q_m R_{tot} dh = -2\pi r_i \Delta T dl \quad (3.17)$$

The enthalpy is a function of the steam quality given as:

$$h = h_g x + (1 - x)h_L \quad (3.18)$$

$$h = h_L + h_{fg} x \quad (3.19)$$

By differentiating the enthalpy function (3.19) in terms of steam quality x , one will get:

$$\frac{dh}{dx} = h_{fg} \quad (3.20)$$

$$dh = h_{fg} dx \quad (3.21)$$

Substituting dh expression in terms of dx equation (3.21) in equation (3.17), we get:

$$q_m R_{tot} h_{fg} dx = 2\pi r_i \Delta T dl \quad (3.22)$$

Substituting thermal resistance R_{tot} by combining its expressions (3.5) and (3.11) in equation (3.22), it becomes:

$$q_m \left(\frac{1}{H_i} + R \right) h_{fg} dx = 2\pi r_i \Delta T dl \quad (3.23)$$

R is a constant part of the thermal resistance irrespective of the flow regime whilst $1/H_i$ will depend on the condensation regime, diameter range and pressure.

According to (Bergman & Lavine, 2017), from a heat transfer calculations perspective, there are two main regimes for condensation in horizontal tubes that are worth accounting for: annular and stratified-wavy, these depend on the velocity of the vapour mainly. As shown in (Figure 3.3), the condensation in (a) is for annular flow regime with high vapour velocity, whilst (b) is for a stratified regime condensation flow with low vapour velocity. Consequently, two different correlations are considered in this model: Shah correlation (1979) which is more common for mode (a) although it does not account specifically for flow regimes and Chato correlation which is more convenient for mode (b) of the condensation.

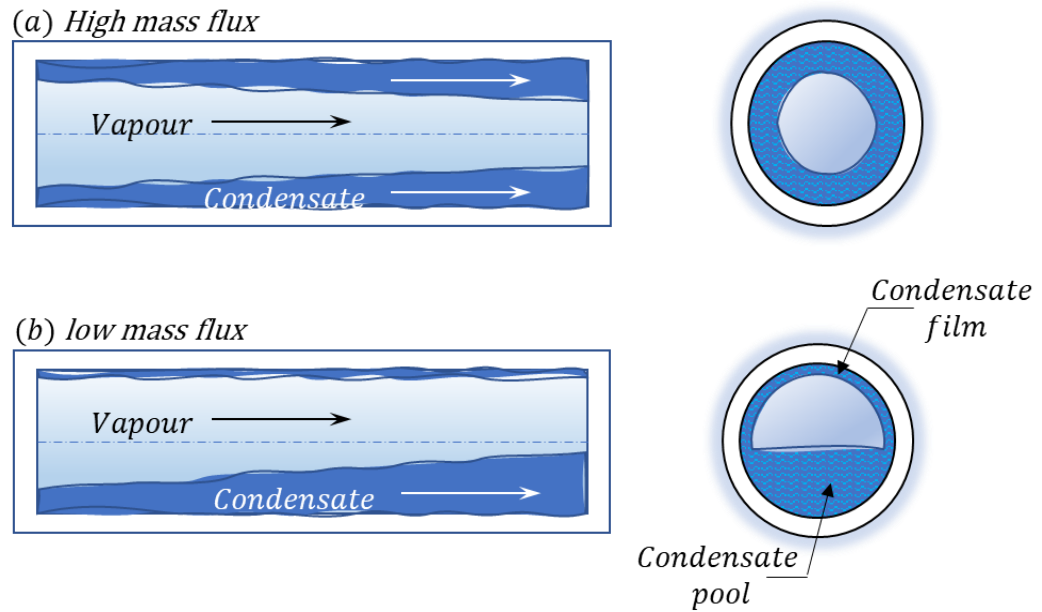


Figure 3.3 Illustration of main dominant regimes during in-tube condensation.

Shah' s correlation (1979) has a recommended range for the mass flux of $10.8 < G < 1599$ $\text{kg/m}^2 \cdot \text{s}$ and is given as:

$$\frac{H_i}{H_{L0}} = (1 - x)^{0.8} + \frac{3.8x^{0.76}(1 - x)^{0.04}}{P_r^{0.38}} \quad (3.24)$$

H_{L0} is the condensation heat transfer coefficient if all flow is assumed to be liquid only. Which is calculated using (Dittus and Boelter, 1930) correlation:

$$H_{L0}D/k_L = 0.023(GD/\mu_L)^{0.8}Pr_L^{0.4} \quad (3.25)$$

P_r is the reduced pressure

$$P_r = \frac{P}{P_{cr}}, \quad P_{cr} = 220.6 \text{ bar} \quad (3.26)$$

P_{cr} is the critical pressure

If we replace the correlation (3.24) in balance equation (3.23), we get:

$$q_m \left[\frac{1}{\left[(1 - x)^{0.8} + \frac{3.8x^{0.76}(1 - x)^{0.04}}{P_r^{0.38}} \right] H_{L0}} + R \right] h_{fg} dx = 2\pi r_i \Delta T dl \quad (3.27)$$

By integrating over x , we can solve the equation to obtain the pipe length L needed to condense the flow for a certain mass flow rate:

$$\int_{x=1}^{x=0} q_m \left[\frac{1}{\left[(1-x)^{0.8} + \frac{3.8x^{0.76}(1-x)^{0.04}}{P_r^{0.38}} \right] H_{L0}} + R \right] h_{fg} dx = \int_{l=0}^{l=L} 2\pi r_i \Delta T dl \quad (3.28)$$

$$\begin{aligned} q_m h_{fg} \left\{ \frac{1}{H_{L0}} \int_{x=0.99}^{x=0} \left((1-x)^{0.8} + \frac{3.8x^{0.76}(1-x)^{0.04}}{P_r^{0.38}} \right)^{-1} + \int_{x=1}^{x=0} (R) \right\} dx \\ = 2\pi r_i \Delta T \int_{l=0}^{l=L} dl \end{aligned} \quad (3.29)$$

By performing integration numerically, the following expression was obtained for the pipe length:

$$\frac{q_m h_{fg} \left\{ \frac{1}{H_{L0}} \int_{x=1}^{x=0} \left((1-x)^{0.8} + \frac{3.8x^{0.76}(1-x)^{0.04}}{P_r^{0.38}} \right)^{-1} dx + R(x_f - x_i) \right\}}{2\pi r_i \Delta T} = L \quad (3.30)$$

Similarly, for relatively low velocity vapour flows, where the stratified regime is observed, (Chato, 1962) correlation is used instead.

For horizontal tubes with small velocity flow, Chato (1962) recommends expression from reference (Cengel & Ghajar, 2020):

$$H_{\text{internal}} = 0.555 \left[\frac{g \rho_l (\rho_l - \rho_v) k_l^3 h'_{lv}}{\mu_l (T_{\text{sat}} - T_s) D} \right]^{1/4} \quad (3.31)$$

Where:

$$h'_{lv} = h_{fg} \left[1 + \frac{3 C_{PL} (T_{\text{sat}} - T_w)}{8 h_{fg}} \right] \quad (3.32)$$

where h'_{lv} is an improvement to the Nusselt theory (Ghiaasiaan, 2011, 445). It accounts for the condensation subcooling and the temperature jump across the film (Lu et al., 2019).

Similarly, replacing correlation (3.31) in (3.23) and performing the integration, we get the expression needed to calculate the condensing pipe length (3.35):

$$\int_{x=1}^{x=0} q_m R_{tot} h_{fg} dx = \int_{l=0}^{l=L} 2\pi (r_i) \Delta T dl \quad (3.33)$$

$$- q_m R_{tot} h_{fg} x = 2\pi (r_i) \Delta T L \quad (3.34)$$

$$\frac{-q_m R_{tot} h_{fg} (x_f - x_i)}{2\pi r_i \Delta T} = L \quad (3.35)$$

Therefore equation (3.30) is used when $G > 10.8 \text{ kg/m}^2 \cdot \text{s}$ whilst expression (3.35) is used when $G < 10.8 \text{ kg/m}^2 \cdot \text{s}$.

Additionally, as can be seen from equation (3.31), the HTC in this case depends on the wall temperature. Initial assumption is made that the pipe surface temperature is equal to the ground temperature.

In the following time steps of the calculation, the inner wall temperature needed for the calculation of the heat transfer is calculated by considering the heat balance across only two interfaces: the pipe wall Eq.(3.2) and the ground Eq. (3.3), this gives expression (3.36). Since the assumption made is that the heat transfer across all the interfaces is the same therefore:

$$\frac{Q}{L} \left(\frac{\ln(r_o/r_i)}{2\pi k_p} + \frac{1}{H_o(2\pi r_o)} \right) = (T_{inner\ pipe} - T_{ground}) \quad (3.36)$$

Q in this expression is the heat ejected through the Ground Heat Exchanger (GHE) from the previous time step, it is calculated as:

$$Q = q_m (h_{in} - h_{out}) \quad (3.37)$$

By rearranging (3.36), we get the final expression for the new average global inner wall temperature:

$$T_{inner\ pipe} = q' \left(\frac{\ln(r_o/r_i)}{2\pi k_p} + \frac{1}{H_o(2\pi r_o)} \right) + T_{ground} \quad (3.38)$$

The cooling part (Sensible heat transfer)

In this section, the sensible heat balance for the second part of the tube is examined. After all flow is condensed, the condensate encounters cooling in the remaining part of the tube.

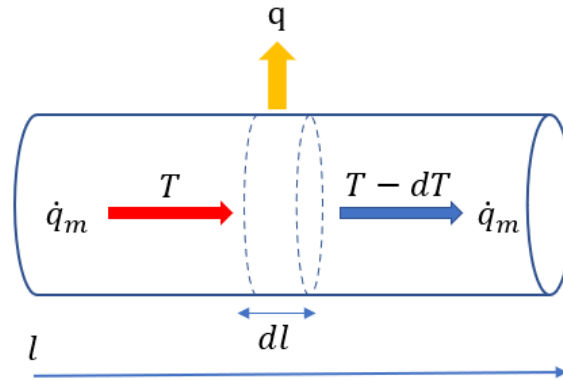


Figure 3.4 Scheme of sensible heat transfer balance.

Starting with equation (3.15) of the energy balance:

$$q_m dh = -q' dl \quad (3.15)$$

As can be seen in Figure 3.4, by assuming the energy change is due to internal energy change in this case, equation (3.15) becomes:

$$q_m c_{pl} dT = -q' dl \quad (3.39)$$

Replacing the linear heat flux by its expression (3.10) in equation (3.39) we get:

$$q_m c_{pl} dT = -\frac{2\pi (r_i)}{R_{tot}} (T - T_{ground}) dl \quad (3.40)$$

T is the condensate temperature

Rearranging:

$$q_m c_{pl} \frac{1}{(T - T_{ground})} dT = -\frac{2\pi r_i}{R_{tot}} dl \quad (3.41)$$

Integrating (3.41) over the length available for subcooling:

$$q_m c_{pl} \int_{T=T_{in}}^{T=T_{out}} \frac{1}{(T - T_{ground})} dT = -\frac{2\pi (r_i)}{R_{tot}} \int_{l=0}^{l=L} dl \quad (3.42)$$

$$q_m c_{pl} \ln \frac{(T_{out} - T_{ground})}{(T_{in} - T_{ground})} = -\frac{2\pi (r_i)}{R_{tot}} L \quad (3.43)$$

This provides the formula for calculating the condensate exit temperature at the GHE outlet:

$$T_{out} = (T_{in} - T_{ground}) \exp\left(\frac{-2\pi r_i}{R_{tot} \dot{m} c_{pl}} L\right) + T_{ground} \quad (3.44)$$

It should be mentioned that all thermophysical properties of steam and water at relevant temperature and pressure values are used from the database provided by National Institute of Standards and Technology (NIST, 2021).

Pipe wall and ground material

With regards to pipe wall material and ground material, the pipe wall material chosen is stainless steel 306 due to its regulated use in the nuclear industry. For the soil material, the type of ground material selected heavily influences the heat transfer. Since soil material varies geographically and based on the depth as well, there is a wide spectrum of materials that could be used. In this initial study for determining the geometrical parameters, the soil material (mixture) is chosen which tends to be at the lower end of the spectrum in terms of favourable thermal physical properties. This is taken as a conservative approach.

For more detailed analysis regarding the effect of ground material, a more comprehensive simulation is performed numerically using the TRACE code. The ground materials tested are listed in heading 4.3.1 and corresponding results in section 5.2.1.

Lastly, it should be noted that the choice to use Chato and Shah correlations in the analytical calculations was determined following a comprehensive literature review of low vapour velocity studies. The two correlations were reported to predict the results significantly well with only 3% deviation compared to many other correlations (Jeon et al., 2013a).

3.1.2. Pressure drop calculations

In this section, the pressure drop encountered by the flow within the loop is examined. The frictional pressure drop can be calculated from the momentum balance equation:

$$\xi \frac{\rho V^2}{2} - g \oint \rho dz = 0 \quad (3.45)$$

ξ is the hydraulic resistance from friction and form losses.

Since it is a steady state assumption, by integrating throughout the whole loop, one ends up with only two terms where basically the driving force has to offset the frictional force:

$$\Delta P_{friction} = \Delta P_{Driving} \quad (3.46)$$

Assuming a closed loop, the hydrostatic driving force and the acceleration terms become zero.

The driving force is calculated with the following expression:

$$\Delta P_{Driving} = (\rho_{out} - \rho_{in}) g H \quad (3.47)$$

ρ_{in} is the density of the fluid at the heat exchanger inlet

ρ_{out} density of the fluid at the heat exchanger outlet

H is the elevation difference

g is the specific gravity constant

The hydraulic resistance is due to frictional forces and form losses and is given as:

$$\Delta P_{friction} = \left(\sum f_D \frac{L}{D_H} + \sum K \right) \frac{\rho V^2}{2} \quad (3.48)$$

This is calculated slightly different in the case of a single-phase flow or a two-phase flow.

Pressure drop in a single phase flow

The pressure-drop for single phase flow using the Darcy equation from (Cengel & Ghajar, 2020) for all types of flow is given as:

$$\Delta p_{f,sp} = f \frac{L}{d_i} \frac{\rho V^2}{2} \quad (3.49)$$

L is the length of the tube

d_i internal diameter

ρ is the fluid density

V is the flow velocity

f is the fanning friction factor, this depends on Reynolds number, and it is calculated for a single-phase flow using the following formulae from (Bai et al., 2017):

$$f = \begin{cases} \frac{64}{\text{Re}} & \text{Re} \leq 2000 \\ 0.3164\text{Re}^{-0.25} & 2000 < \text{Re} \leq 3.0 \times 10^4 \\ 0.184\text{Re}^{-0.2} & 3.0 \times 10^4 < \text{Re} \leq 2.1 \times 10^6 \\ 0.01 & \text{Re} > 2.1 \times 10^6 \end{cases} \quad (3.50)$$

Expression (3.49) is for one single phase, which could be used for the pressure drop across the hot riser and the main pipe downcomer, as well as in the part of the heat exchanger after the flow has fully condensed.

The same expression for Darcy equation could be written in terms of G

$$G = \frac{q_m}{A} = \rho V \quad (3.51)$$

By substituting:

$$\Delta p_{f,sp} = f \frac{L}{d_i} \frac{G^2}{2\rho} \quad (3.52)$$

Conversion in terms of G is required for the implementation in the MATLAB script.

Pressure drop for two phase flows across the condenser

To obtain the pressure drop due to friction during two-phase flow in the heat exchanger, one can make use of the phase multiplier explained earlier in 2.3.4 as in equation (3.53):

$$\Delta p_{f,tp} = \phi_{l0}^2 f \frac{L}{d_i} \frac{\rho V^2}{2} \quad (3.53)$$

ϕ_{l0}^2 is the phase multiplier if all fluid is assumed to be liquid only, it is obtained either from homogenous or from separate flow model.

If we consider the (Martinelli-Nelson 1948) method, values for the integral of the separate model phase multiplier for a varying steam quality are tabulated and provided in graphs by (Thom, 1964) and (Collier & Thome, 1994), this approach is reported to provide more realistic values when compared to the homogeneous model (M. Ghiaasiaan, 2017).

For instance, the value of the integral for steam-water mixture from $x=0$ to $x=1$ for a 2 bar pressure flow can be read from figure 2.5 in (Collier & Thome, 1994, 56):

$$\frac{1}{x} \int_0^x \Phi_{f0}^2(x) dx = 300 \quad (3.54)$$

This value is read from the graph and is used in the calculations. So basically, the value obtained for frictional forces from assuming all fluid to be liquid is multiplied by this value.

It should be noted that the value of Reynolds number used to obtain fanning factor f depends on the phase multiplier used and whether we consider the homogenous model or separate flow model. If we take all liquid phase multiplier ϕ_{l0}^2 , then the Reynolds number is calculated for all liquid flow only, not the vapour inlet conditions. If the homogenous model is used, then there are different formulas for the Reynolds number using the averaged two phase density and viscosity formulas as found in (M. Ghiaasiaan, 2017). The following formula for Reynolds number is taken in this case accordingly with the multiplier.

$$Re = GD/\mu_L \quad (3.55)$$

Therefore, two phase flow pressure drop across all pipes of the GHE during condensation is given by:

$$\Delta P = \sum_{N=1}^N \frac{L_{condenser\ tube}}{x} \int_0^x \Phi_{i0}^2(x) dx * \frac{f}{D_{condenser\ tube}} \frac{\rho_{i0} V_{i0}^2}{2} \quad (3.56)$$

If we consider the single-phase flow pressure drop for the subcooling of the condensate as well, the overall expression for the pressure drop across the GHE becomes:

$$\Delta P_{GHE} = N \left(\frac{L_{condensing}}{x} \int_0^x \Phi_{i0}^2(x) dx * \frac{f}{D_{condenser\ tube}} \frac{G^2}{2\rho_{i0}} + \frac{f L_{subcooling}}{D_{condenser\ tube}} \frac{G^2}{2\rho_{i0}} \right) \quad (3.57)$$

Pressure drop from local losses is due to abrupt contractions, elbows, flow expansion... etc

$$\Delta P_{local\ losses} = \sum K \frac{\rho V^2}{2} \quad (3.58)$$

In terms of G:

$$\Delta P_{local\ losses} = \sum K \frac{2G^2}{\rho} \quad (3.59)$$

The overall total pressure loss across the loop is hence given by Eq. (3.61)

$$\begin{aligned} \Delta P_{loss\ total} = & \Delta P_{hot\ riser(vapour)} + \Delta P_{condenser\ (two\ phase+single\ phase)} \\ & + \Delta P_{downcomer(liquid)} + \Delta P_{local\ losses} \end{aligned} \quad (3.60)$$

$$\begin{aligned} \Delta P = & \left[f_D \frac{L_{hot\ riser}}{D_{hot\ riser}} \frac{\rho_v V_v^2}{2} + N \left(\frac{L}{x} \int_0^x \Phi_{i0}^2(x) dx \frac{L_{condenser\ tube}}{D_{condenser\ tube}} \frac{\rho_L V_L^2}{2} + \frac{f L_{subcooling}}{D_{condenser\ tube}} \frac{\rho_L V_L^2}{2} \right) \right. \\ & \left. + f_D \frac{L_{main\ piping}}{D_{main\ piping}} \frac{\rho_L V_L^2}{2} + \sum K \frac{\rho V^2}{2} \right] \end{aligned} \quad (3.61)$$

The values for the loss coefficient factors K are used from (ASHARE, 2017). For instance, for 90 degrees elbow, K= 0.45.

After a preliminary calculation, it was noted that pressure drop in the main pipework during single phase flow (hot riser, downcomer, returning pipe) is insignificant compared to the condenser, and therefore was considered negligible.

Calculating the mass flow rate of the steam

Initially, we assume that the condensate has not yet returned to the calandria. By setting up the mass balance in the calandria, taking the control volume as the water volume in the calandria, starting with the continuity equation:

$$\frac{dm}{dt} = -q_m \quad (3.62)$$

$$\frac{d(\rho_L V_L)}{dt} = -q_m \quad (3.63)$$

For the energy balance:

$$\frac{dE}{dt} = -Q_m + P_d \quad (3.64)$$

Where P_d is the decay power generated in the reactor, and Q_m is the energy escaping as steam

$$\frac{d(h_L \rho_L V_L)}{dt} = -q_m h_v + P \quad (3.65)$$

$$h_L \frac{d\rho_L V_L}{dt} = -q_m h_v + P \quad (3.66)$$

Substituting the mass balance equation (3.63) into the energy balance (3.66) we get:

$$h_L q_m = -q_m h_v + P \quad (3.67)$$

Rearranging:

$$q_m = \frac{P}{h_v - h_L} \quad (3.68)$$

Equation (3.68) is used in the initial time step where the liquid is assumed to be at saturation temperature. When setting up the steady state balance with the condensate returned to the calandria, equation (3.69) is obtained. In the latter one, the condensate returned to the calandria is not necessarily at saturation conditions, the condensate is subcooled in this case.

$$q_m = \frac{P}{h_{in} - h_{out}} \quad (3.69)$$

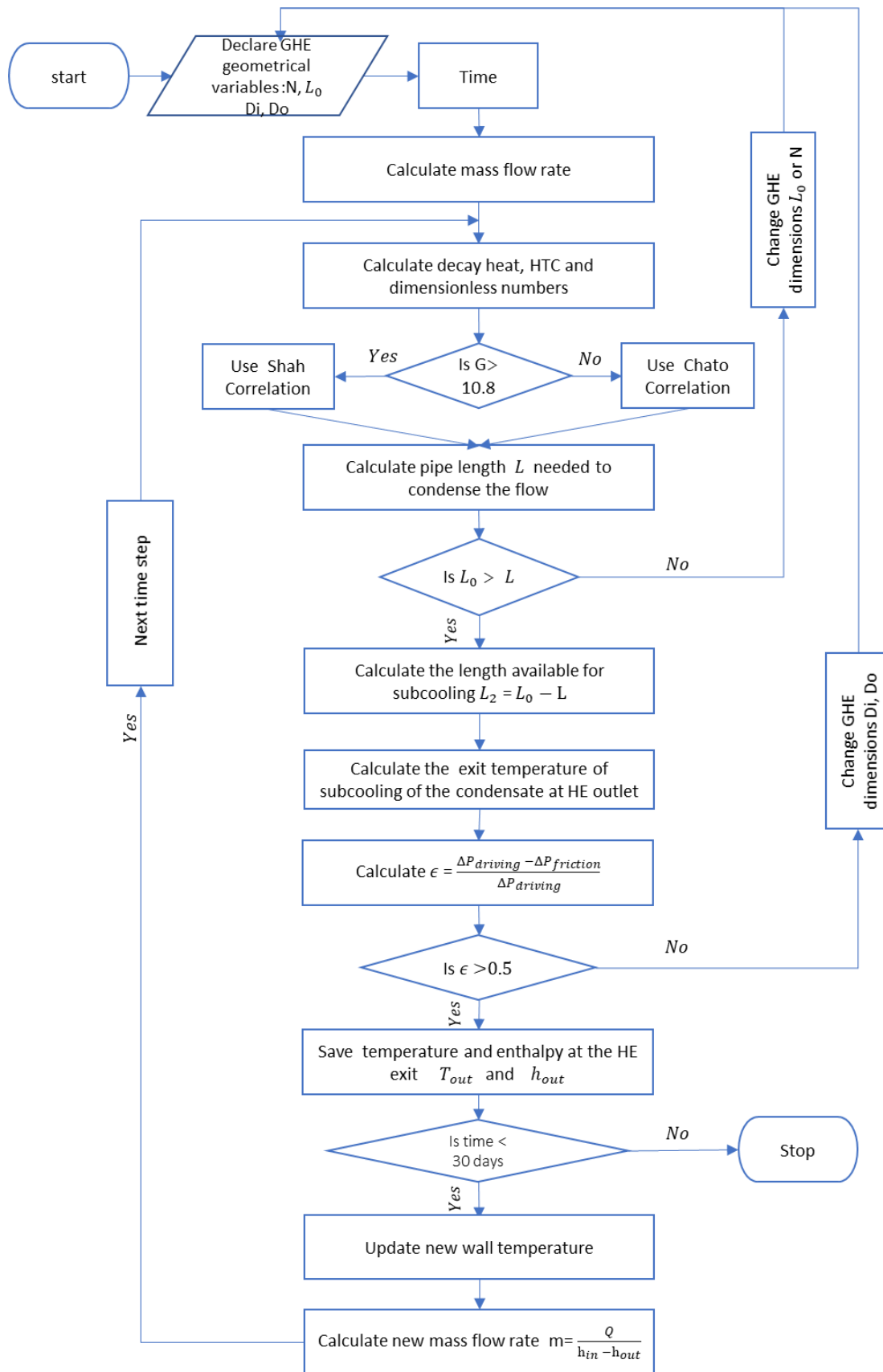


Figure 3.5 MATLAB Calculation script for pure steam case.

3.2. Steam and Non-Condensable Gas

To account for the effect of non-condensable gas on the heat transfer process, a more detailed condensation heat transfer model is developed in this section. As reported in (Wu & Vierow, 2006), it is important to treat the top and the bottom parts separately in condensation heat transfer calculations to assess the overall process, therefore the same approach is adopted.

The adopted model uses the (Lee & Kim, 2011) degradation factor, which was selected in this particular application because it is one of the very few empirical correlations that has been validated for horizontal in-tube condensation. Compared with available studies in the literature, it is a simple, more inclusive model that builds on previous works of (Kuhn et al., 1997; Siddique et al., 1993; Sparrow et al., 1967). Although Lee & Kim correlation is suggested for different tube diameters, the conditions for which the factor was developed also falls within the same geometrical and operating parameters of the heat exchanger in this study. It was experimentally tested for low vapour velocity, small tube diameters of 13-27.5 mm and a pressure of 0.2 MPa. Unlike other works, the model also accounts for the effect of surface shear that the Nusselt model is lacking and was not considered in previous works mentioned above.

In this model, both heat transfer through the top part of the tube and the bottom portion are calculated separately. Using the approach recommended in (Lee & Kim, 2011) and (Sereda et al., 2021), for the top part, the Chato correlation is employed:

$$H_{\text{pure,top}} = H_{\text{Chato}} = 0.725 \left[\frac{g\rho_l(\rho_l - \rho_v)k_l^3 h'_{lv}}{\mu_l(T_{\text{sat}} - T_w)D} \right]^{1/4} \quad (3.70)$$

And for the bottom part, the Nusselt film heat transfer coefficient is employed:

$$H_{\text{pure,bot}} = H_{\text{Nusselt}} = \left[\frac{g\rho_l(\rho_l - \rho_v)k_l^3 h'_{lv}}{4\mu_l(T_{\text{sat}} - T_w)l} \right]^{1/4} \quad (3.71)$$

Where l is the length along the tube, a detailed explanation on the derivation of Eq. (3.71) is found in (Polo, 1998, 8-9).

The improved latent enthalpy is calculated using (Rohsenow, 1952) correlation:

$$h'_{lv} = h_{fg} \left[1 + 0.68 \frac{C_{pL}(T_{sat} - T_w)}{h_{fg}} \right] \quad (3.72)$$

For this analysis, the surface area for the bottom and top parts of the wall will vary along the length of the tube. The corresponding surface areas depend on the condensation film accumulating along the bottom downstream. This is usually determined using the angle of flooding (θ_{flood}) which is illustrated in Figure 3.6.

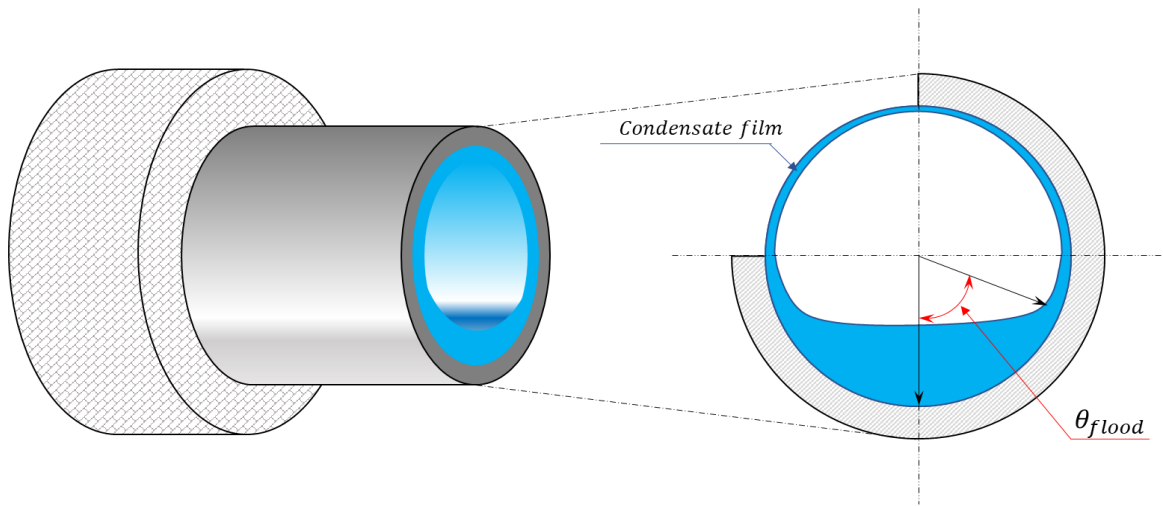


Figure 3.6 Pipe cross section view illustrating flood angle.

The flooding angle determines the wetted surface and is calculated using the Biberg correlation (3.73), which employs the use of the void fraction. Biberg correlation according to (Sereda et al., 2021) is:

$$\theta_{flood} = \pi(1 - \varepsilon) + \left(\frac{3\pi}{2} \right)^{\frac{1}{3}} \left[1 - 2(1 - \varepsilon) + (1 - \varepsilon)^{\frac{1}{3}} - \varepsilon^{\frac{1}{3}} \right] - \frac{1}{200} (1 - \varepsilon)\varepsilon[1 - 2(1 - \varepsilon)][1 + 4((1 - \varepsilon)^2 + \varepsilon^2)] \quad (3.73)$$

where ε is the void fraction.

Many correlations for the void fraction have been proposed. The correlations are generally categorised into four categories: Homogeneous, slip ratio, based on Lockhart -Martinelli parameter and lastly the drift flux model. They are all listed in (Shen et al., 2017). In (M. Ghiaasiaan, 2017), there are further correlations and even categorised into five categories.

In this particular model, the (Butterworth correlation, 1975) equation (3.74) is used, which is basically the empirical fit for graphical data presented by (Lockhart & Martinelli, 1949). The Lockhart-Martinelli work is chosen for this model because it was developed using a database of air-water mixtures and steam. Also, the diameter range in the original study works here, in addition to the fact that it has been particularly reported to provide good results in the condensation heat transfer calculations (Sereda et al., 2021), although it was developed for adiabatic flow conditions.

$$\varepsilon = \frac{1}{1 + 0.28 \left(\frac{1-x}{x}\right)^{0.64} \left(\frac{\rho_s}{\rho_l}\right)^{0.36} \left(\frac{\mu_1}{\mu_g}\right)^{0.07}} \quad (3.74)$$

Once the void fraction as well as the angle of flooding is determined within the specified node/control volume, the surface area for the heat transfer for the top and bottom parts can be determined accordingly.

For the top part, the heat transfer rate is therefore calculated according to expression (3.75) which is obtained by setting up the heat balance:

$$q_{top} \left(\frac{1}{H_{top}} + R \right) = 2(\pi - \theta)(r_i) \Delta T dL \quad (3.75)$$

For the bottom part:

$$q_{bot} \left(\frac{1}{H_{bot}} + R \right) = 2\theta(r_i) \Delta T dL \quad (3.76)$$

Where the heat transfer coefficients are the ones obtained for the pure case multiplied by Lee and Kim degradation factor.

The degradation factor depends on the air-steam mixture, is given by following correlation:

$$f = H_{\text{exp,mix}}/H_{\text{pure}} = \tau_{\text{mix}}^{*0.3124} (1 - 0.964W_{\text{nc}}^{0.402}) \quad (3.77)$$

where:

τ_{mix}^* is the dimensionless shear stress

W_{nc} is the mass fraction of the non-condensable gas in the air-steam mixture

The correlation is applicable for the following conditions:

$$\begin{aligned} 0.06 < \tau_{\text{mix}}^* < 46.65 \\ 0.038 < W_{\text{nc}} < 0.814 \end{aligned} \quad (3.78)$$

The dimensionless stress is:

$$\tau_{\text{mix}}^* = \frac{\tau_{\text{mix}}}{g\rho_f L} = \frac{1/2\rho_{\text{mix}}u_{\text{mix}}^2 \cdot f}{g\rho_f L} \quad (3.79)$$

The mixture velocity is calculated

$$u_{\text{mix}} = \frac{\text{Re}_{\text{mix}} \mu_{\text{mix}}}{\rho_{\text{mix}} D} \quad (3.80)$$

The characteristic length is

$$L = (v_f^2/g)^{1/3} \quad (3.81)$$

The friction factor is

$$f = f(x) = \begin{cases} 16/\text{Re}_{\text{mix}}, & \text{Re}_{\text{mix}} < 2300 \\ 0.079\text{Re}_{\text{mix}}^{-1/4}, & \text{Re}_{\text{mix}} > 2300 \end{cases} \quad (3.82)$$

Once the degradation factor is obtained, it is then used to obtain the real HTCs and hence the heat transfer rate. The new mixture properties are then updated in the following node.

The viscosity of the gas mixture of (air + steam) is calculated using the (Wilke, 1950) formula, which is proposed to give accurate results in (Ghiaasiaan, 2011, 21).

$$\mu = \sum_{j=1}^n \frac{X_j \mu_j}{\sum_{i=1}^n X_i \phi_{ji}} \quad (3.83)$$

X is the molar fraction. And ϕ_{ji} given by the following expression:

$$\phi_{ji} = \frac{\left[1 + (\mu_j/\mu_i)^{1/2} (M_i/M_j)^{1/4}\right]^2}{\sqrt{8}\left[1 + (M_j/M_i)\right]^{1/2}} \quad (3.84)$$

The initial mass fraction of NCG declared in terms of mass fraction is converted into the molar fraction:

$$X_l = \frac{m_l M}{M_l} \quad (3.85)$$

Where M and M_l represent the molar masses of the mixture and the chemical-specific l , respectively, the chemical species here are considered to be the steam and the dry air. It is worth noting that the air is treated as an element after calculating its relevant properties, although it is a mixture itself.

So, the molar mass of the mixture (air + steam) is calculated with equation (3.86):

$$\frac{1}{M} = \sum_{j=1}^N \frac{m_j}{M_j} \quad (3.86)$$

m_j is the mass fraction of the specific component

The amount of steam removed is calculated by taking the balance equation (3.15) across the specified small finite volume:

$$q_m dh = -q' dl \quad (3.15)$$

Replacing equation (3.21) into (3.15)

$$q_m h_{fg} dx = -q' dl \quad (3.87)$$

And therefore, the portion of steam quality condensed in a specified node is calculated as:

$$dx = \frac{Q}{q_m h_{fg}} \quad (3.88)$$

Q is the accumulative heat transfer removed by the specified node,

q_m is the mixture mass flow rate,

h_{fg} is the specific latent heat of vaporization.

Once the amount of steam condensed is obtained, the new gas mixture quality is updated to be used in the calculations in the following cell:

$$x = 1 - dx \quad (3.89)$$

It is worth noting that the gas quality in this model represents the quality of both air + steam mixture and therefore when the steam has fully condensed the quality is not zero but equals the initial air mass fraction W_{nc} .

The degradation factor depends on the mixture properties, which is changing along the length of the tube. Therefore, the tube spatial length is discretised using a relevant mesh size into small control volumes and calculations are performed in a step wise approach per node.

Steam mass flow values for each time step are imported from the pure steam case model results, the total mixture mass flow is assumed constant in the axial direction, heat transfer is calculated using (3.75) and (3.76) for the top and bottom parts of the tube respectively, the total heat flux obtained is then used to calculate the amount of steam condensed in the specified node according to equation (3.88) which is then used to find the new gas quality as per equation (3.89) in the following spatial node as shown in the algorithm flowchart (Figure 3.7).

Similarly to the pure steam case model in section 3.1.1, since both HTC's expressions for Chato (3.70) and Nusselt (3.71) depend on the wall temperature, this is calculated in the following time step in a similar way to the pure steam model, using Eq. (3.38). Unlike the first model however, which calculates the global average temperature, in this model, the local updated temperature is calculated separately in each node.

Additionally, several assumptions are embedded within the analysis:

It is assumed that the vapour and non-condensable mixtures are in saturation conditions and thermal equilibrium, this is the case usually for real life evaporators and condensers (Ghiaasiaan, 2011, 16).

$$T_v = T_{air} = T_{mix} = T_{sat}(P_v) \quad (3.90)$$

where subscript v denotes the vapour.

It is also assumed that the treated gases (steam and dry air) follow Dalton law (Ghiaasiaan, 2011, 12).

$$P = \sum_{l=1}^n P_l \quad (3.91)$$

Where P is the total pressure of the mixture and P_l is the partial pressure of species l .

Moreover, the assumption during condensation is that the heat removed is all via latent heat transfer from the steam portion while the air (non-condensable gas) mass flow remains constant at constant saturation temperature and pressure.

The flowchart in Figure 3.7 outlines the whole MATLAB calculation procedure step by step.

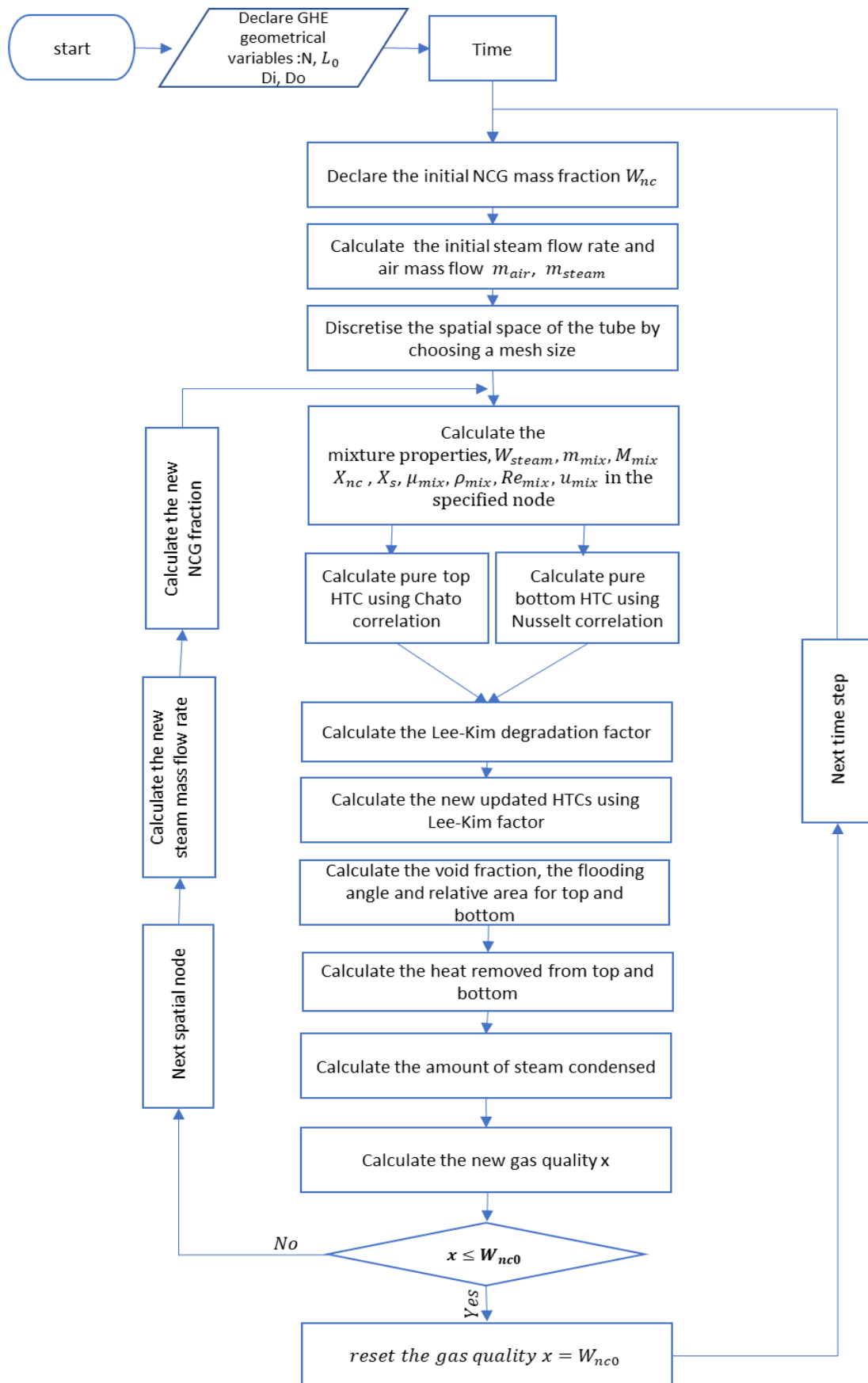


Figure 3.7 MATLAB calculation procedure with NCG presence.

4. Computational Study/Numerical Model

This chapter starts with a brief introduction on system codes, then examines the used system code TRACE, its field equations, condensation models employed and input models nodalization.

4.1. Thermal Hydraulic System Codes

System codes are powerful computational tools that are very important in nuclear safety analyses. The use of system codes over the years has been an integral part of the design, licensing, and operation of nuclear power plants. With the advance of computers over the recent years, system codes reached a level of sophistication enabling to perform some advanced calculations that were not practically possible using simple theory models in the past.

System codes are used to simulate the behaviour of nuclear power plants during many postulated events and transients. The value of the code lies in saving time and resources to carry out the events on real-life large-scale experimental facilities or actual plants. The codes however must be verified and validated against relevant separate effects tests and integral effects tests experimental data before they can be considered reliable. Currently, various numerical system codes are used in the industry worldwide, to mention a few: TRACE, RELAP and APROS.

System codes are of one dimensional (1D) nature with very limited 3D capabilities. 1D description is possible due to the clear main flow paths in the cooling loops. They are based on the so-called “two-fluid model” with separation of the water and vapor phases, resulting in systems with at least six balance equations. The six-equation model is based on the conservation equations of **mass**, **momentum**, and **energy** for the two phases separately in addition to non-condensable gases.

Typical system codes include model hydrodynamics, heat transfer between structures and fluids, modelling of fuel, reactor kinetics models, and control systems. In a nutshell, the code is composed of the following (Prošek, 2020):

1. **Field (conservation) equations**- provide code capability to address global processes.

2. **Closure equations**-mainly empirical which provide code capability to model and scale particular processes.
3. **Numerics**- execute computations in an efficient and accurate manner.
4. **Components and control**- This focuses on the ability of the code to model plant geometry and execute efficient and accurate plant computations.

4.2. TRACE Code

As defined in the theory manual: “*The TRAC/RELAP Advanced Computational Engine (TRACE - formerly called TRAC-M) is the latest in a series of advanced, best-estimate reactor systems codes developed by the U.S. Nuclear Regulatory Commission for analyzing transient and steady-state neutronic-thermal-hydraulic behavior in light water reactors. It is the product of a long term effort to combine the capabilities of the NRC’s four main systems codes (TRAC-P, TRAC-B, RELAP5 and RAMONA) into one modernized computational tool.*” (USNRC, 2019)

4.2.1. Field equations

In the two-phase model, two phases are considered separately, and the continuity equation, momentum and energy equations are averaged over time. In addition to Reynolds’s averaging, since the flow in system codes is one dimensional, the equations are also averaged over channel areas and applied to each phase separately.

The coefficients terms utilised in these equations whether for heat transfer, friction, and pumps coefficients needed for the closure, are usually empirical values obtained through experiments or semi-empirical correlations.

4.2.2. Trace calculation algorithm and condensation models

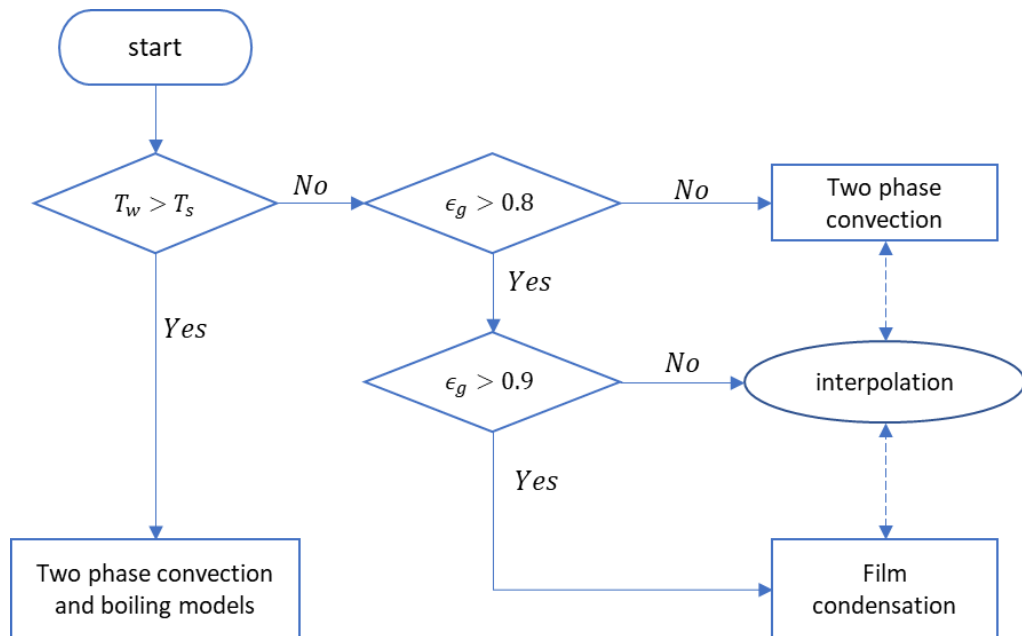


Figure 4.1 TRACE heat transfer regime selection logic for condensation, source TRACE Manual (USNRC, 2019, 278)

For condensation, TRACE makes use of three different regimes: film condensation, two-phase convection, and an interpolation method. Film condensation is activated in the code if the void fraction is higher than 90%, and the wall temperature is lower than the saturation temperature of the gas (Figure 4.1). Film condensation is the primary standard model for condensation heat transfer, but this could be changed depending on the type of pipe used. When the pipe type is changed to PIPETYPE = 12 which is “Horizontal Tube”, the stratified condensation model using Jaster and Kosky correlation (4.1) is employed instead. (USNRC, 2019). Both models are examined in the following sections.

$$\text{Nu} = \frac{\bar{H}D}{k_L} = 0.728 \epsilon^{3/4} \left[\frac{\rho_L(\rho_L - \rho_V)gh'_{fg}D^3}{k_L\mu_L(T_{\text{sat}} - T_w)} \right]^{1/4} \quad (4.1)$$

The film condensation calculates the Nusselt number for the heat transfer across the film and relative thickness of the film depending on several flow conditions and whether the film is laminar or turbulent. This model is substantiated by empirical correlations which differ in

the case of turbulent or laminar. The empirical correlation of Kuhn, Schrock and Peterson is used for laminar and for the turbulent case several different correlations are used.

In the presence of non-condensable gas, TRACE currently utilises a special model for film condensation that was developed by (Kuhn et al in 1994) specifically for the development of passive containment cooling systems (USNRC, 2019). This model calculates the normal heat transfer coefficients wall to liquid described above but the effect of NCG is considered by employing the mass transfer model which increases the thermal resistance across the interface when NCG is present. This is calculated in an iterative scheme.

4.3. Model Nodalization

The following section illustrates the model nodalization used for the study simulations as well as the necessary settings for both the single pipe test and the entire loop simulation.

4.3.1. Single pipe test

The initial study is carried out for a simple single tube surrounded by ground material. The tested length was only 3 m in this case, which represents part of the tube. The pipe in the horizontal orientation was tested for a variety of conditions and parameters that are believed to influence the heat transfer process. Two different types of pipes were used: "No Accumulator" which uses the falling film condensation model and the "Horizontal Tube" which is validated for stratified condensing flows. The obtained results are used to guide the design for the entire loop of the decay heat removal system.

The heat flux is tested for the following conditions/parameters:

- Ground material
- Pressure
- Inclination angle
- Amount of non-condensable gas

Material thickness

In order to simulate a semi-infinite soil material surrounding the pipe as is the assumption in the theoretical model, a thickness of 10 m was given to the ground material. Which is basically a cylindrical shape surrounding the pipe. This was determined following several simulations where the thickness of the material was varied to observe a change in the outside surface temperature. A heat flux of 0 W/m^2 was applied as an outer boundary condition for the ground heat structure. At a thickness of 10 m, there was no change in the outside surface temperature after 1 month simulation time. The real boundary conditions applied may vary according to the depth at which the system is located which is not yet determined at this stage.

Ground material properties

Thermo-physical properties of the ground materials considered in the study are presented in Table 4.1. Soil (mixture) properties are the same used in the analytical solution which is taken from reference (Zohuri & McDaniel, 2019). Finnish granite thermal conductivity ranges from 1.6 to 5 W/ (m K). In terms of conductivity property, Finnish granite tends to be at the upper end of the world's granite spectrum. In several studies, the mean value for Finnish granite conductivity is reported as 3.5 W/ (m K) in (Oosterbaan et al., 2017) which is employed in the simulation. The rest of the material properties have been extracted from the latest up to date available database which is developed specific for geothermal applications (Dalla Santa et al., 2020).

Table 4.1 Thermophysical properties of different ground materials.

Ground Material type	C_p [J/(kg K)]	ρ [kg/m ³]	k [W m ⁻¹ K ⁻¹]
Soil (mixture)	1840.00	2050	0.52
Granite	835.96	2697.5	2.74
Clean gravel (dry)	725.00	2000	0.4
Heterometric gravel with sand (wet)	725.00	2000	1.08
Medium sand (dry)	598.75	2000	0.4
Medium sand (wet)	1047.62	2100	1.9
Silt (dry)	788.16	1900	0.55
Silt and clayey silt (wet)	1079.76	2100	1.45
Finnish granite	714.00	2635	3.5

Inclination angle

Condensation for inclined tubes is not as much extensively researched in the literature as compared to vertical and horizontal. such studies are considered to be rare according to a state of art report reviewing inclined tubes condensation by (Lips & Meyer, 2011). According to the studies, there is an optimum angle that enhances the heat transfer and has no effect on pressure drop. The optimum angle varies but it falls within the range of 10-40 (Lips & Meyer, 2011) and according to some other studies between 10 and 30 degrees downward (Olivier et al., 2016).

Inclination for stratified regime condensation has been proven to enhance the heat transfer coefficient for the bottom part of the tube since the condensate will drain faster. Although it practically had no impact on the top part HTC (Ahn et al., 2019). It is therefore investigated in this section to determine a suitable inclination that may be used in the final proposed loop geometry.

Single pipe input model

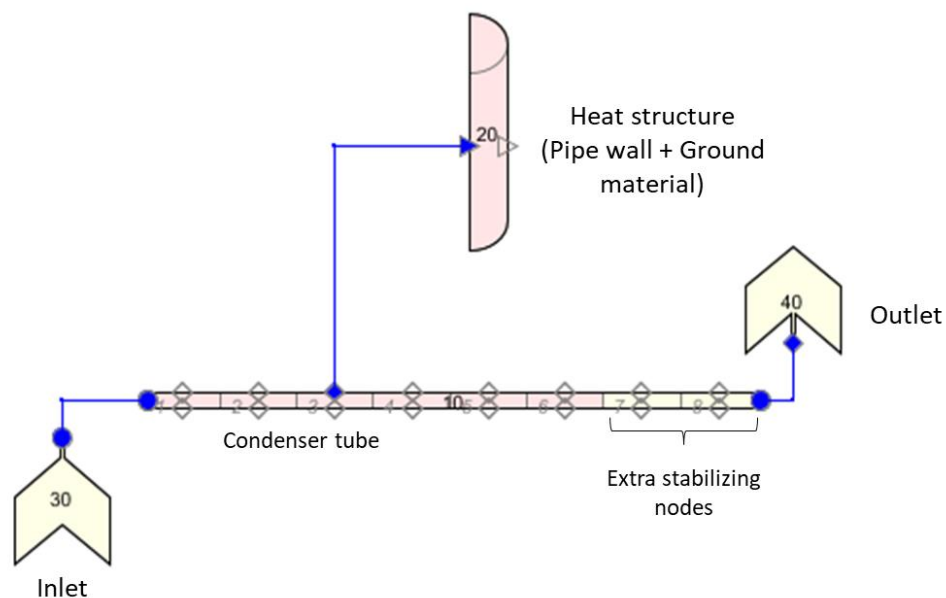


Figure 4.2 Single pipe TRACE input model.

The used nodalization is illustrated in Figure 4.2. A FILL component is used for the inlet, BREAK component for the outlet, and a heat structure HTSTR for both pipe wall and ground material surrounding the flow. The pipe was discretised into 6 control volumes in addition to more stabilizing nodes in the axial direction with 0.5 m each. The discretization of the heat structure in the radial direction varied between the “No Accumulator” and the “Horizontal Tube”. In the first case, 81 elements with 161 nodes were used, whilst the second pipe required more elements (193 elements, 385 nodes), the use of any lower number of discretization elements resulted in very long simulation times.

At the outlet, two extra nodes were added at the end of the heated part of the pipe, these serve to stabilize the results of the obtained heat flux and the NCG pressure and mass, which oscillated in a preliminary simulation conducted initially without the addition of these nodes. It was already reported in other studies in the literature that such effect has been observed (Park, 2015).

For the inlet, the FILL type used in the study is a Generalised state which deemed the most suitable. The simulations were tested for four different FILL types: “Constant Velocity”, “Constant Mass Flow”, “Constant Generalized State”, and “Generalized State”. The FILL component with a constant mass flow and constant generalized state had some inlet effect which distorted the heat flux results. Similarly as reported in (Park, 2015).

Simulations with the single pipe test were run for an equivalent time of 1 week after initiation of the event in each case.

4.3.2. Loop study

The full TRACE input model for the proposed RHR loop is shown in Figure 4.3. The “sliced nodalization” technique was adopted for the discretization of the loop. The calandria and hot riser on the left-hand side of the loop were discretised into control volumes with boundaries at the same elevation as the control volumes of the pipes on the right-hand side of the loop. This technique is proven to reduce the uncertainties associated with calculations in loops with natural circulation (Bajs et al., 2000).

The following configurations were set for the model:

- Axial conduction is considered
- Mesh option: Finite element
- The non-condensable gas selected as air

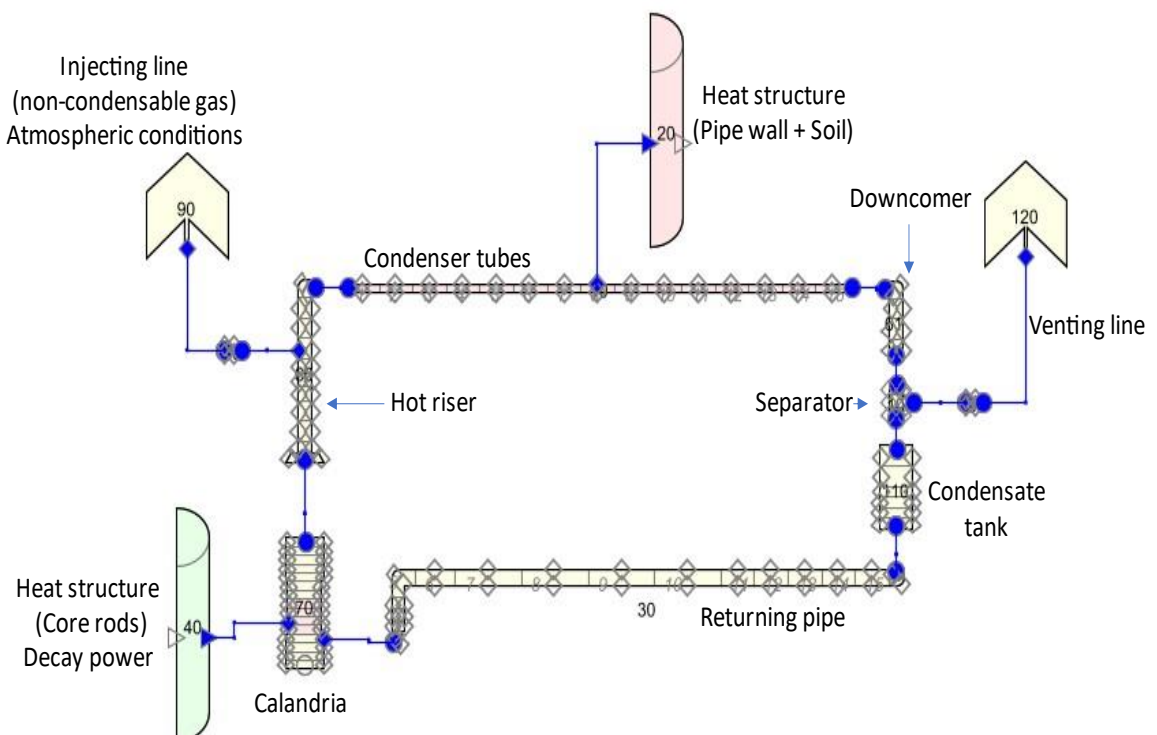


Figure 4.3 TRACE input model for proposed LUTHER RHR loop.

Heat structures (HTSTR) are used for the reactor core and (Pipe wall + Soil) modelling. The core is modelled as illustrated in Figure 2.1 with 3294 fuel elements, full geometry is provided in (Hyvärinen & Truong, 2020), the decay power was then assigned according to the Wigner-Way formula (2.1).

Both Injecting and Venting lines are modelled using BREAK components. The BREAK component represents a constant volume with atmospheric pressure, which injects NCG into the system automatically when the loop pressure falls below that. The amount of NCG injected is proportional to the pressure difference. Backflow was prevented in the reverse flow for the non-condensable gas injection line to prevent the steam generated in the reactor from escaping the loop. Similarly, the backflow at the end of the venting line was prevented to eliminate any gas from entering the loop at that end. Additionally, to prevent the injected gas from providing a cooling route by cooling down the steam and then being vented, the initial condition of injected air is assumed to be at the same saturation temperature as the steam.

The separator is an “ideal separator” which separates the two phases, ejecting the gas through the venting line and returning the liquid to the “Condensate tank” as shown in Figure 4.3.

The simulation loop is run for 2 hrs just to demonstrate the operability of the RHR system.

5. Results and discussion

The results for the analytical and numerical studies are presented in this chapter.

5.1. Analytical Results

The first model for pure steam calculates the global heat transfer parameters for the purpose of determining the surface area needed for the heat exchanger. Whilst the second model presents the results for the local heat transfer parameters in the presence of NCG.

5.1.1. Pure steam case results

The heat exchanger geometry in Table 5.1 was determined using the MATLAB calculations for a decay heat removal surface area that could sufficiently remove decay heat over a period of one month in the case of pure steam, according to the procedure's flowchart in Figure 3.5.

Table 5.1 Proposed GHE geometrical parameters based on pure steam model.

Number of pipes	Pipe length [m]	Internal diameter D_i [mm]	Outer diameter D_o [mm]
247	30	20	23

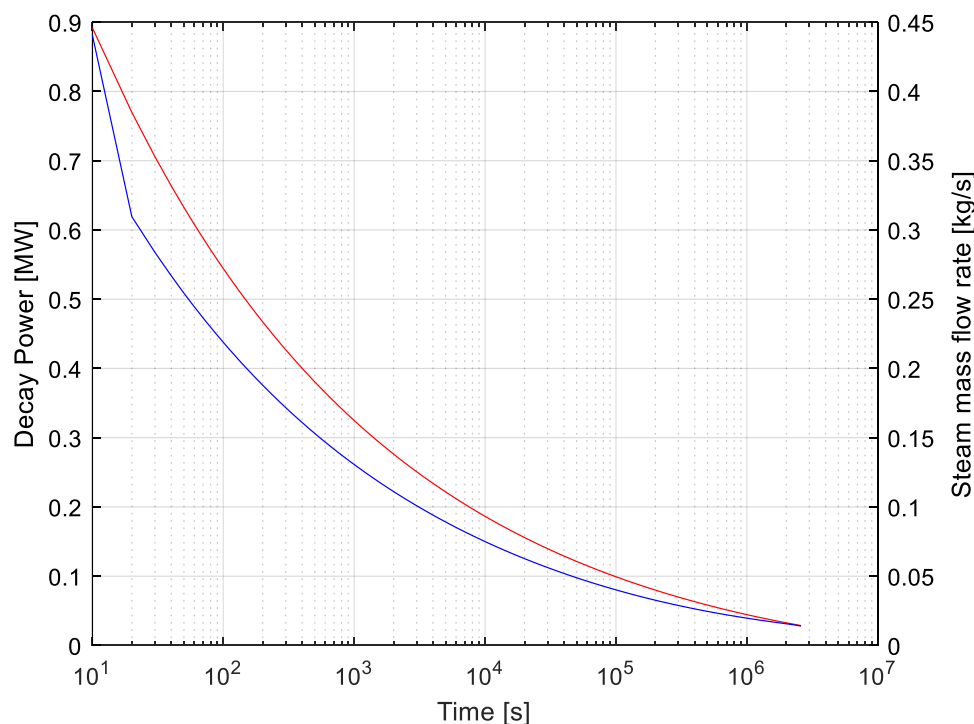


Figure 5.1 Decay heat power and total steam mass flow rate over time.

Figure 5.1 shows that the amount of steam generated correlate with the decay heat released in the reactor, both show an exponential decay. This is based on the assumption that all heat released is transferred to the calandria fluid. In real situations, there will be more heat dissipation to the surrounding structure and the environment through the calandria walls, and hence the generated steam flow rate would be lower.

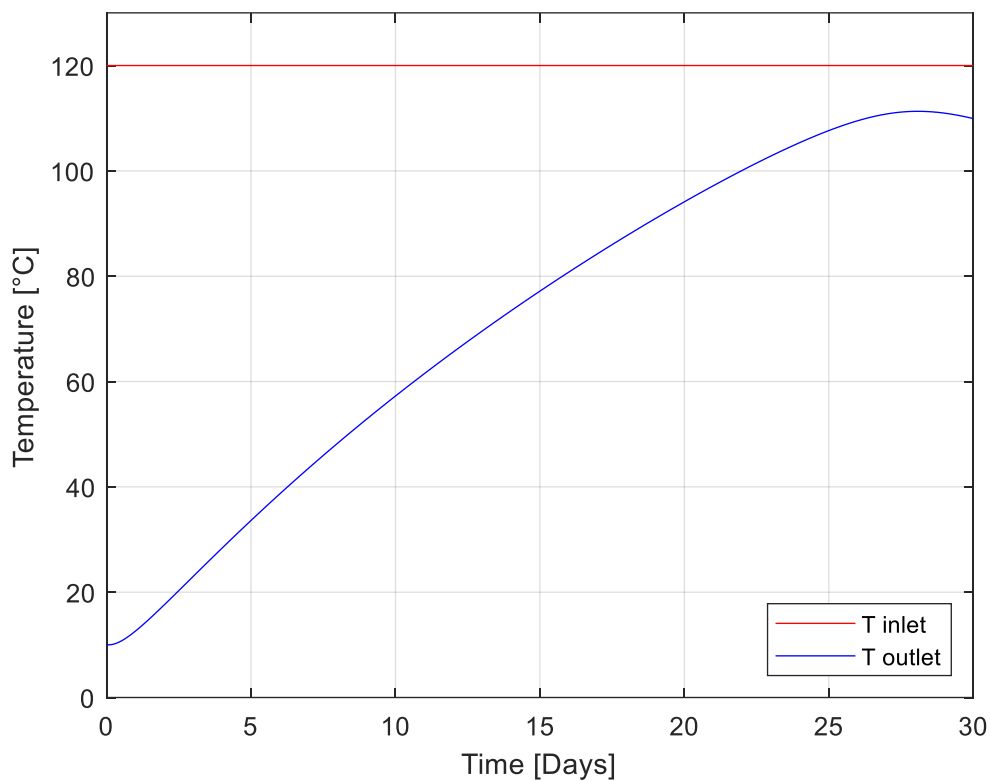


Figure 5.2 Temperature across heat exchanger inlet and outlet over time.

As can be seen in Figure 5.2, the heat removal capacity/capability of the proposed pipe bundles deteriorates over time but remain sufficient to eject all decay heat and condense the generated steam even after 1 month time following the initiating event. The temperature of the condensate at the exit of the heat exchanger is constantly increasing over time which is attributed to the heat up of the surrounding ground.

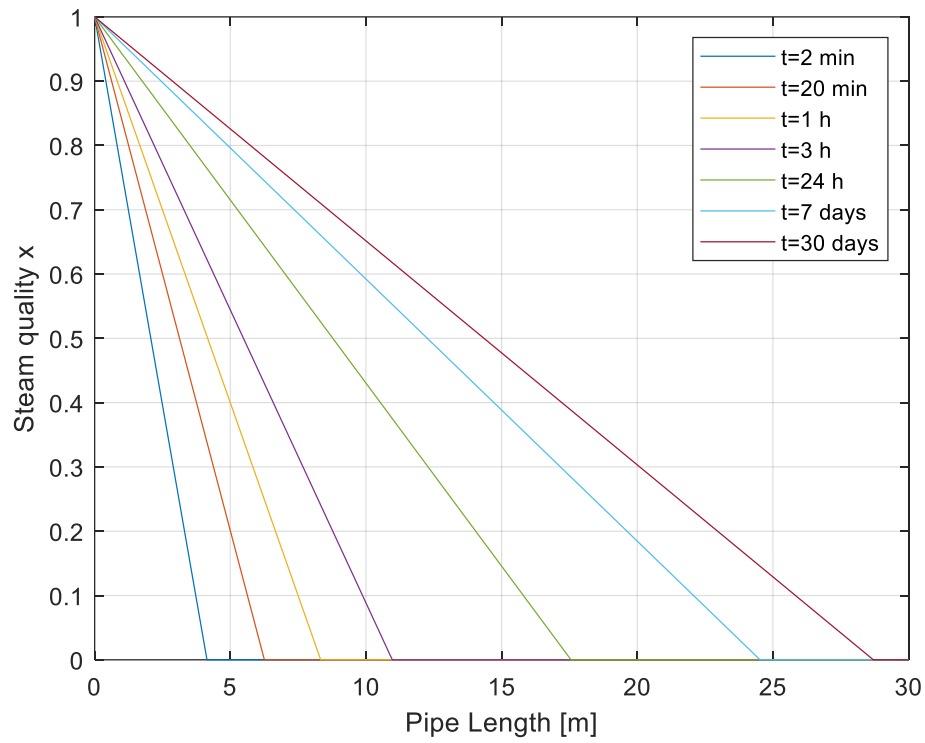


Figure 5.3 Steam quality axial profile across condenser pipe for different times.

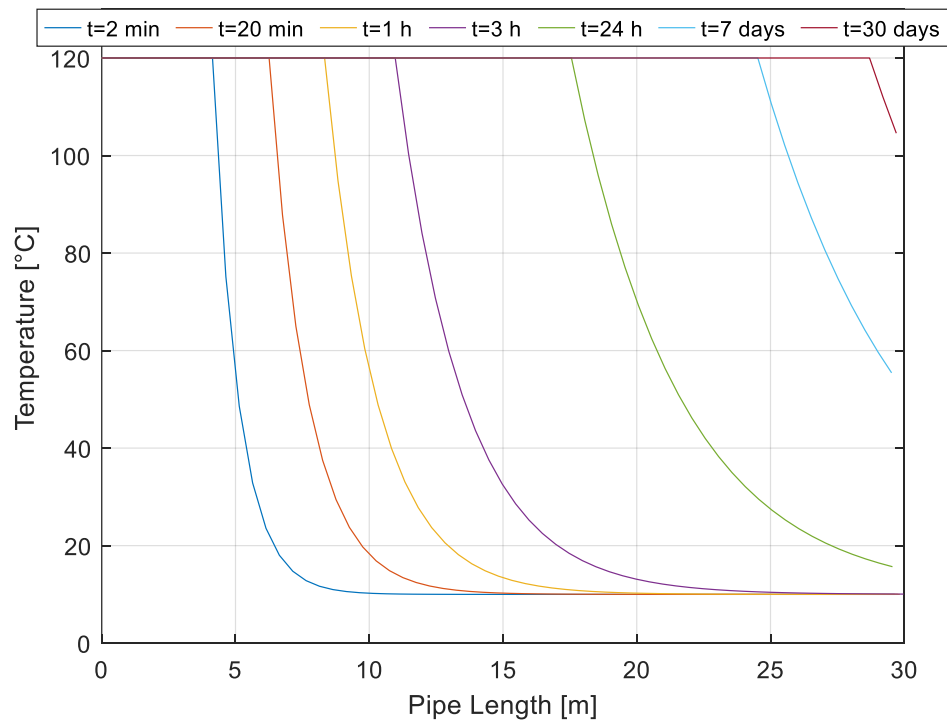


Figure 5.4 Fluid bulk temperature across condenser pipe for different times.

Although the decay heat is exponentially decreasing over time, the ground HTC is deteriorating aggressively in parallel, showing an exponential decay pattern at a faster pace (Figure 5.5). Consequently, resulting in a more surface area needed for decay heat removal 30 days after shutdown, then 2 min after shutdown. Figure 5.3 and Figure 5.4 show that after 30 days, almost all length of the pipe is needed just to condense the steam without barely any considerable cooling to the condensate.

This is due to the thermophysical properties of the chosen soil material which is characterised by very poor thermal conductivity and specific thermal heat capacity. As a result, the soil material heats up rapidly making the ground HTC in Eq. (3.6), the parameter that dictates the heat transfer and consequently the decisive factor in the geometry of the GHE.

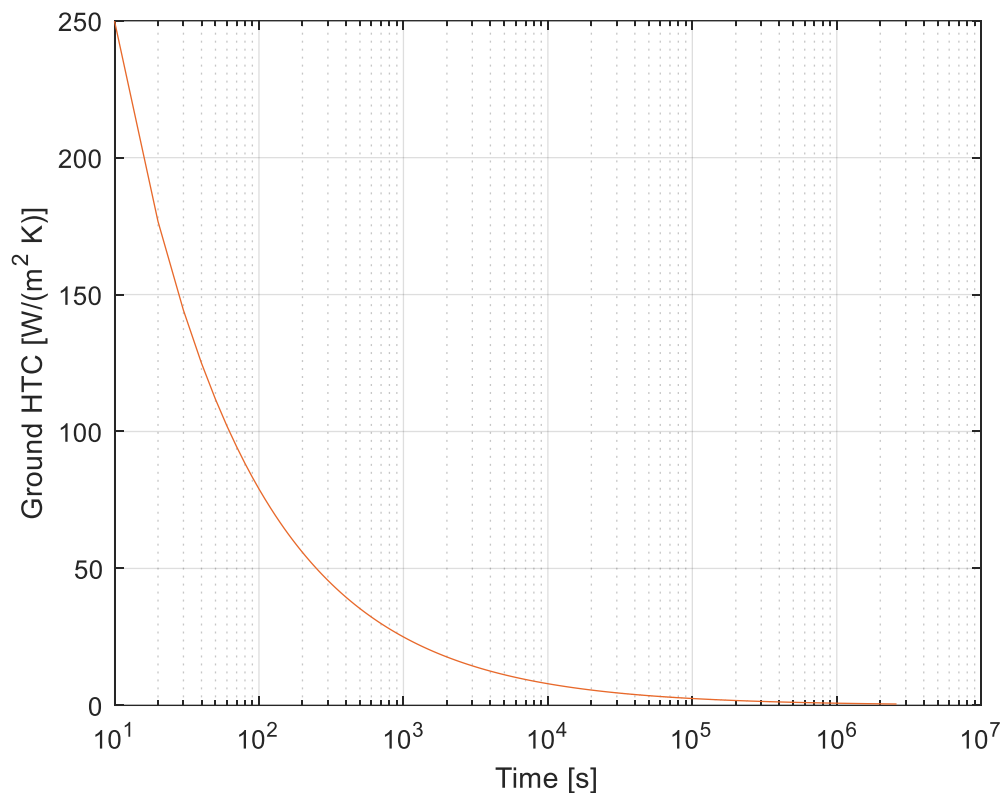


Figure 5.5 Ground HTC deterioration over time.

5.1.2. Model with NCG and Lee Kim degradation factor

The second model calculates the local heat transfer coefficients and local heat fluxes for the top and the bottom parts separately. With this model, a more thorough examination is enabled to determine the influence of the presence of NCG in the system with good confidence. The tested pipe has the same dimensions presented in Table 5.1. The length of pipe shown in each figure corresponds to the length needed to fully condense the flow at that time step.

Mesh sensitivity study

Initially, the theoretical model with NCG was first validated against (Lee & Kim, 2011) experimental data for test 99 for low vapour velocity of 1 g/s, 0.202 MPa pressure and an air mass fraction of 5.1 %. As shown in Figure 5.6, the theoretical results correlate quite well with the experimental data. The model also has low mesh sensitivity, Figure 5.6 demonstrates that varying mesh sizes result in minor deviation. Therefore, a mesh size of 0.125 m was deemed reasonable for carrying out the GHE simulations, without requiring too much computational power and space.

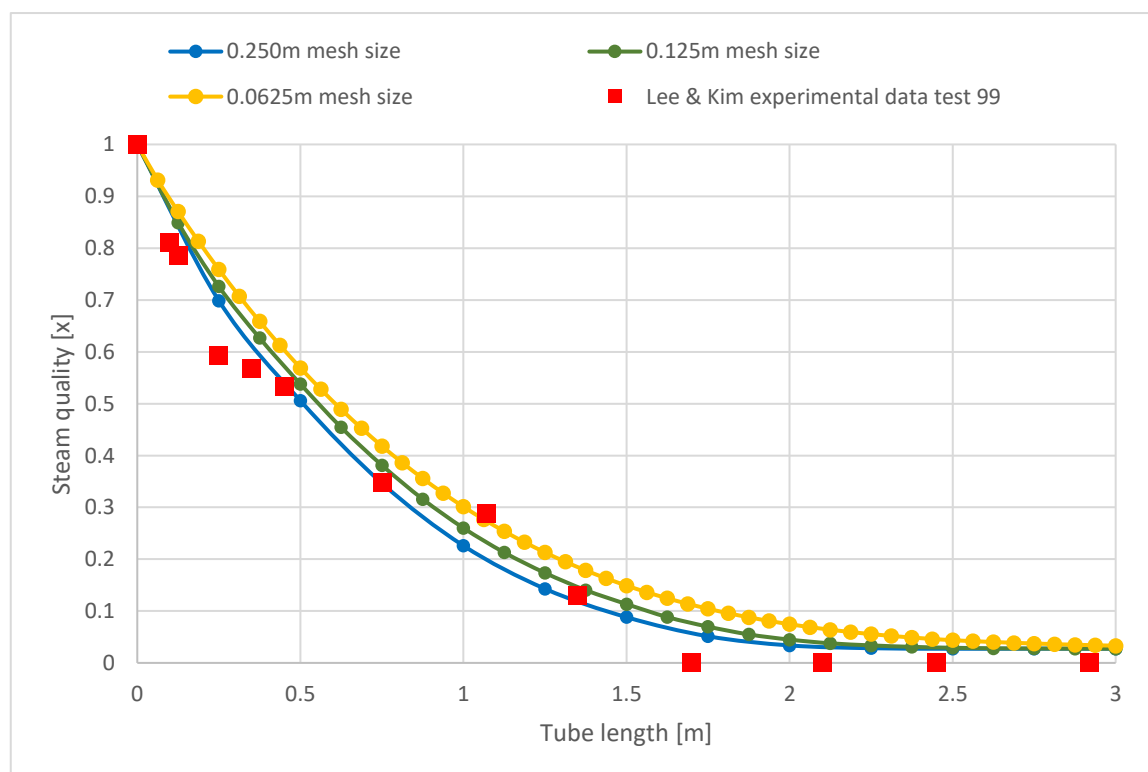


Figure 5.6 Theoretical model validation and mesh sensitivity study.

Initial results are plotted for 2 minutes after shutdown, HTC and heat flux values at that time step are plotted against relevant partial length needed for condensing the flow. The effect of NCG is also examined for the plotted parameters in the following figures.

Heat Transfer Coefficients

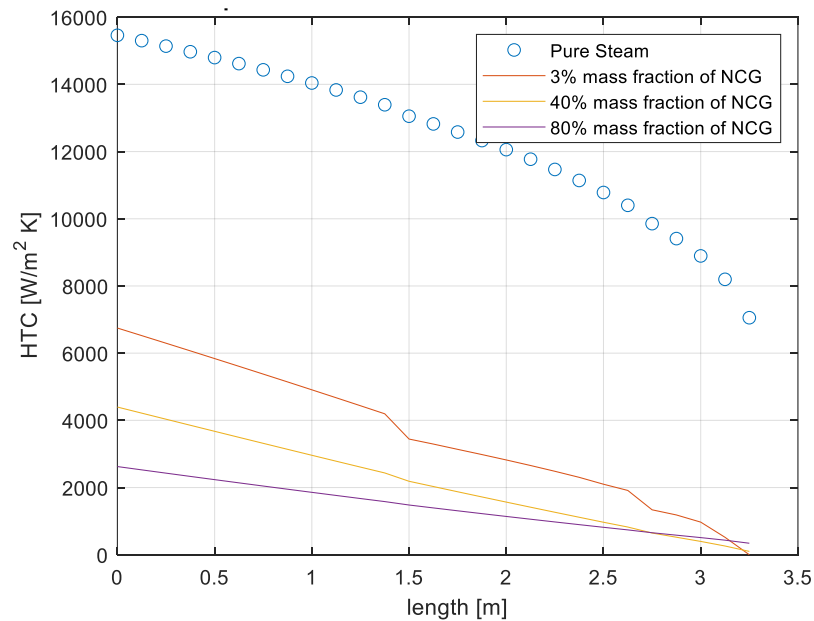


Figure 5.7 Top internal HTC axial profile for different (Steam +NCG) mixtures, 2 minutes after shutdown.

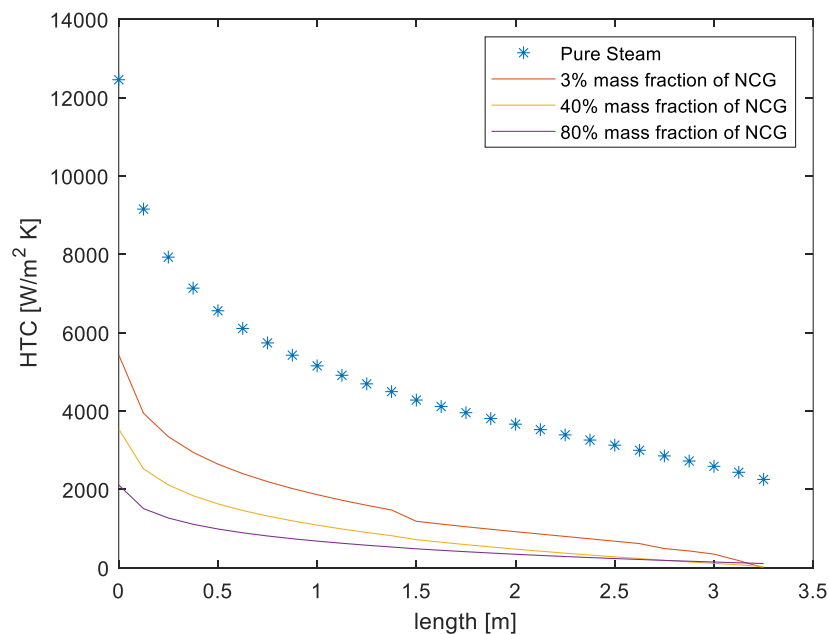


Figure 5.8 Bottom internal HTC axial profile for different (Steam +NCG) mixtures, 2 minutes after shutdown.

Figure 5.7 and Figure 5.8 show the internal HTC for top and bottom part of the tube respectively against the required length (3.25m) to condense the flow 2 minutes after shutdown. The pure steam HTC for the top part shown in (Figure 5.7) is relatively higher compared to the bottom part (Figure 5.8) and does not seem to decrease as severely along the pipe as the bottom HTC does. This is mainly due to the accumulation of the condensate film at the bottom of the pipe forming a much thicker layer, which consequently introduces more thermal resistance. The thickness of the layer continues to increase along the pipe downstream.

Additionally, the presence of non-condensable gas seems to deteriorate the condensation heat transfer coefficient value significantly for both top and bottom HTCs. A presence of as small as 3 % mass fraction of NCG, reduces the internal HTCs by over 60 %. The higher the fraction of the NCG, the more significant effect it has on the internal heat transfer coefficient. A mass fraction of 80 % reduces the HTC in initial node by over 80 % of that of pure steam case for the same steam mass flow.

Furthermore, the effect of NCG is constantly becoming more evident along the length of the pipe in comparison to the first node. Since the steam condenses in that direction, the mass fraction of the NCG continues to increase along, and hence further reducing the value of the HTC.

Heat Flux on the outer surface of the pipe

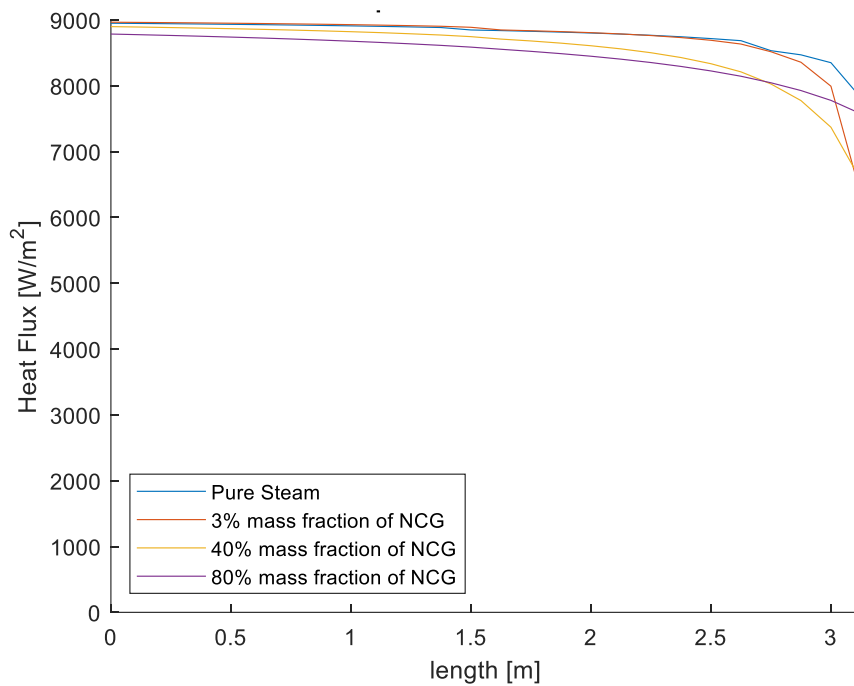


Figure 5.9 Axial profile of top radial heat flux for different (NCG + steam) mixtures, 2 minutes after shutdown.

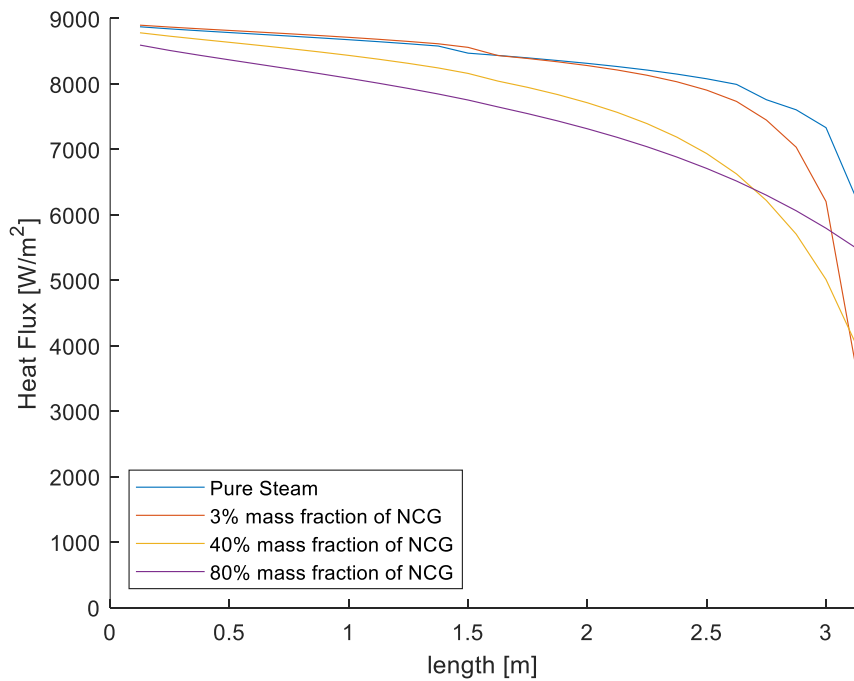


Figure 5.10 Axial profile of bottom radial heat flux for different (Steam + NCG) mixtures, 2 minutes after shutdown.

Figure 5.9 and Figure 5.10 show the heat flux 2 minutes after shutdown across the outer surface of the pipe, the heat fluxes do not show the same pattern as the corresponding internal HTC shown in Figure 5.7 and Figure 5.8 for top and bottom parts respectively. Although both HTCs decrease significantly for both top and bottom parts due to the presence NCG, the corresponding heat flux 2 minutes after shutdown does not seem to be influenced by the presence of NCG. This is because the thermal conductivity of the soil material surrounding the pipe is very poor. Resulting in relatively higher thermal resistance at the interface from the pipe outer surface to the surrounding ground which remains significantly higher than the thermal resistance added by the presence of NCG as in expression (5.1). Hence the heat removal from the pipe is dictated by the soil material thermal properties.

$$R_{tot} = \frac{1}{H_i} + \frac{\ln(r_o/r_i)(r_i)}{k_p} + \frac{r_i}{H_o r_o} \quad (3.5)$$

$$\frac{1}{H_o} \gg \frac{1}{H_i} \quad (5.1)$$

Although the internal HTC decreases severely, NCG tends to have little to no influence in this case on the overall heat transfer across the pipe outer wall. The thermal resistance of the soil is considerably larger just 2 minutes after shutdown (Figure 5.12) and continues to increase exponentially over time (Figure 5.11) making it the key factor in the whole heat transfer.

Thermal resistance

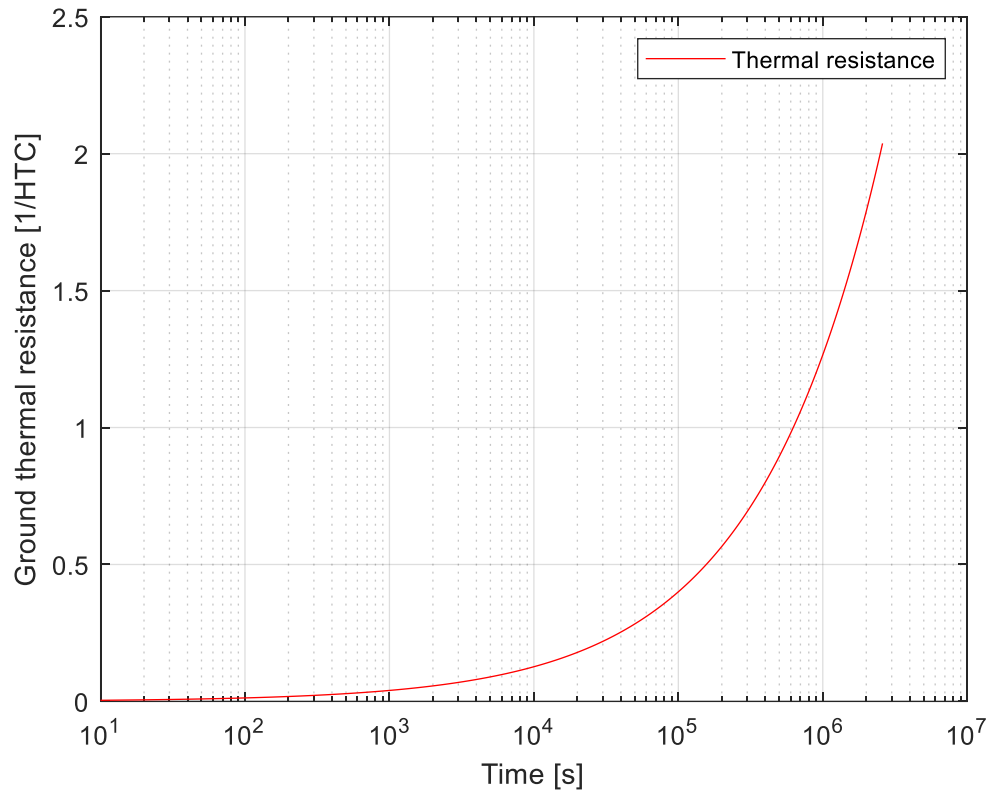


Figure 5.11 Ground thermal resistance over time.

As can be seen from the plot, the thermal resistance of the soil material is increasing exponentially over time. The soil is dictating the heat transfer process making the additional thermal resistance introduced by the extra layer of NCG later in time totally insignificant in this case.

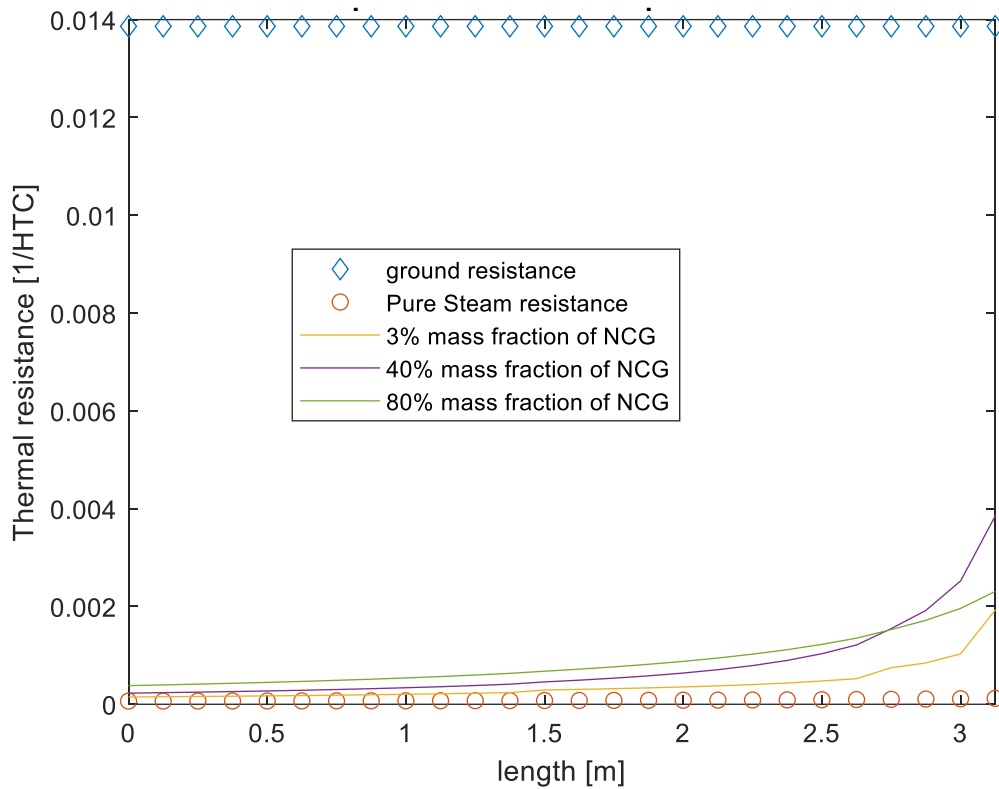


Figure 5.12 Thermal resistance profile across the top part of the tube for gas mixtures with varying NCG fractions, 2 minutes after shutdown.

It is worth noting that the case illustrated in Figure 5.9 and Figure 5.10 for the heat flux, to show the effect of NCG is considered just 2 minutes after the initiating event. At that point of time, the thermal resistance of the ground is at its lowest value but already considerably higher compared to the resistance induced by the steam + NCG (Figure 5.12). This is therefore the most susceptible the system should be to the effect of NCG. As time progresses, with the exponential growth of the ground thermal resistance as can be seen in Figure 5.11, it can be projected that any additional thermal resistance postulated later will have almost no effect on the heat transfer process. All in all, the soil material thermal properties dictate the heat removal capability of the proposed heat exchanger.

Radial heat flux across the pipe outer walls over time

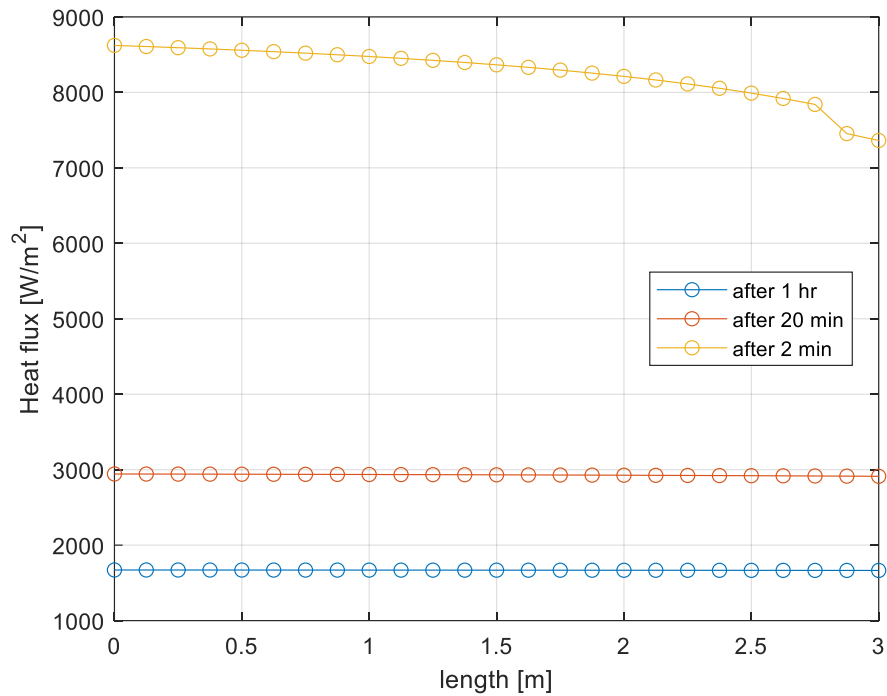


Figure 5.13 Axial profile of top radial heat flux across a partial pipe length for a gas mixture with 80 % air at different time steps.

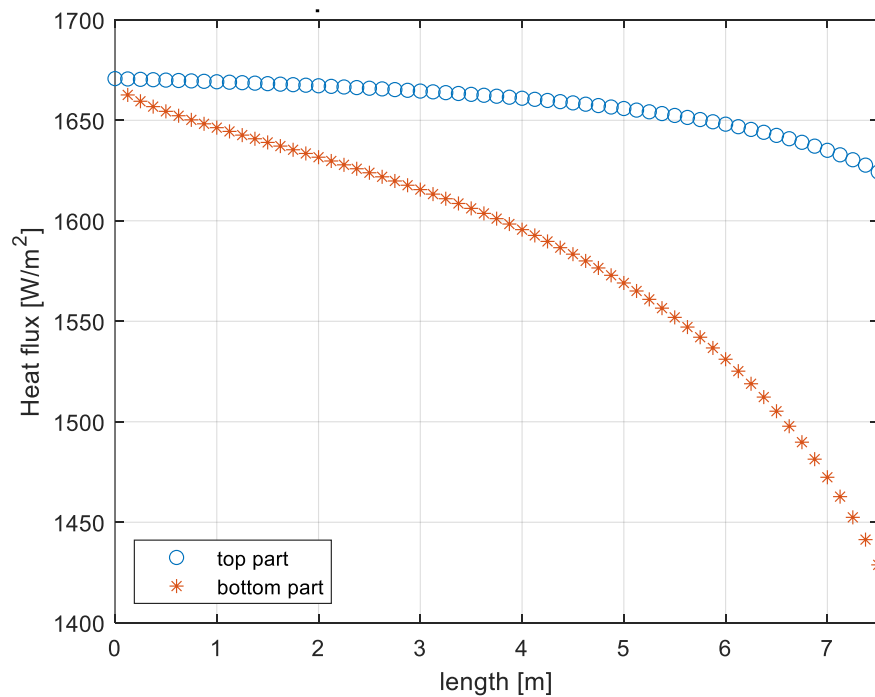


Figure 5.14 Axial profile of radial heat flux for top and bottom parts of the tube, 1hr after shutdown for a gas mixture with 80 % air.

Figure 5.13 shows the deterioration of the heat flux over time through the condenser pipe walls for a partial length of the tube. The heat flux recorded one hour after the initiating event and is around 20 % of that 2 min after the shutdown. Moreover, when examining the heat flux one hour after the shutdown against needed length for full flow condensation, top and bottom parts separately as shown in (Figure 5.14), the upper part has a relatively higher flux. This is influenced by the flow regime during condensation (stratified). The lower part heat flux is lower due to two main reasons: the film layer is considerably thicker and hence results in more resistance. The employed Nusselt HTC also provides relatively lower value than the Chato correlation. Since both HTCs depend on the wall temperature, this is higher for the upper part than the lower part of the tube as well, as can be seen in Figure 5.15.

Temperature axial profile

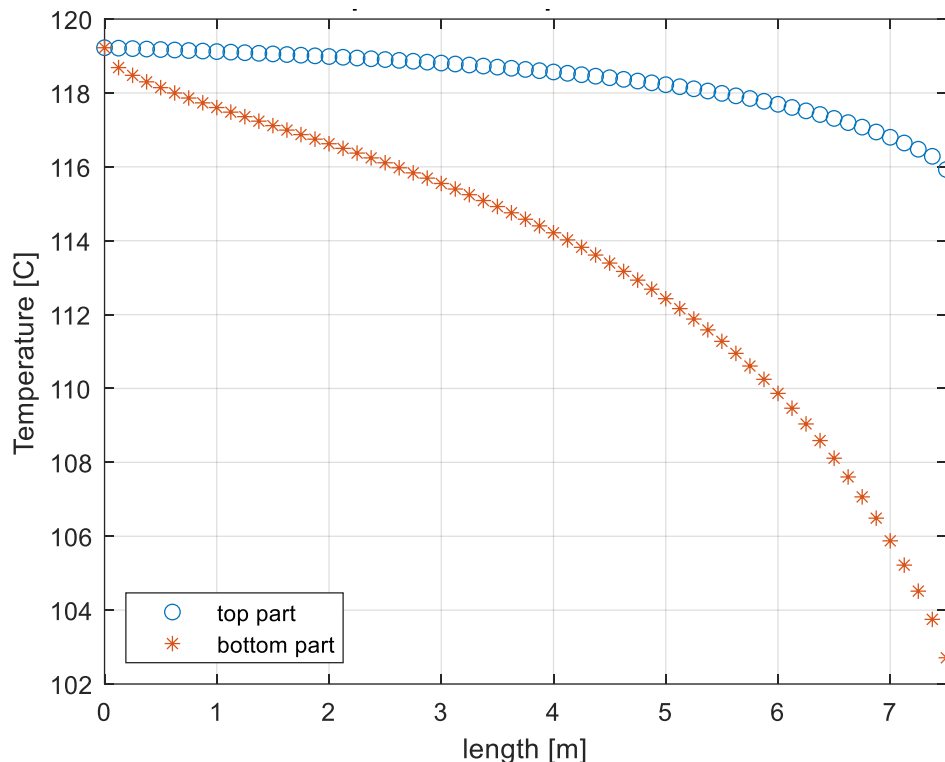


Figure 5.15 Axial profile of inner wall temperature for top and bottom parts of the tube, 1 hr after shutdown.

When comparing the axial temperature profile 1 hr after the shutdown for the top and bottom parts, the bottom part of the tube remains slightly cooler than the upper part (Figure 5.15). The condensate film formed along the tube provides a layer of insulation.

All in all, from the results obtained using the theoretical model with Lee-Kim factor, it is safe to say that the effect of the NCG is already accounted for and bounded by the ground thermal resistance. Therefore, the initially proposed geometry from the case of pure steam remains valid for condensing air-steam mixtures composed of up to 80 % NCG.

5.2. TRACE Numerical Simulations Results

Results from the numerical simulations with the TRACE code are presented in this section, initially for the single pipe test compared to the analytical solution and for the loop simulation results.

5.2.1. Single pipe results and comparison with analytical model

The pipe was tested for a wide range of conditions and configurations that could potentially influence the heat transfer in the tube. The different results obtained from the single tube test are studied to understand how such parameters could influence the overall loop design. The obtained results are then fed into the design metrics for determining the final overall geometry proposed for the loop, to ensure efficient removal of decay heat under the studied conditions.

Comparison of TRACE condensation models and analytical results

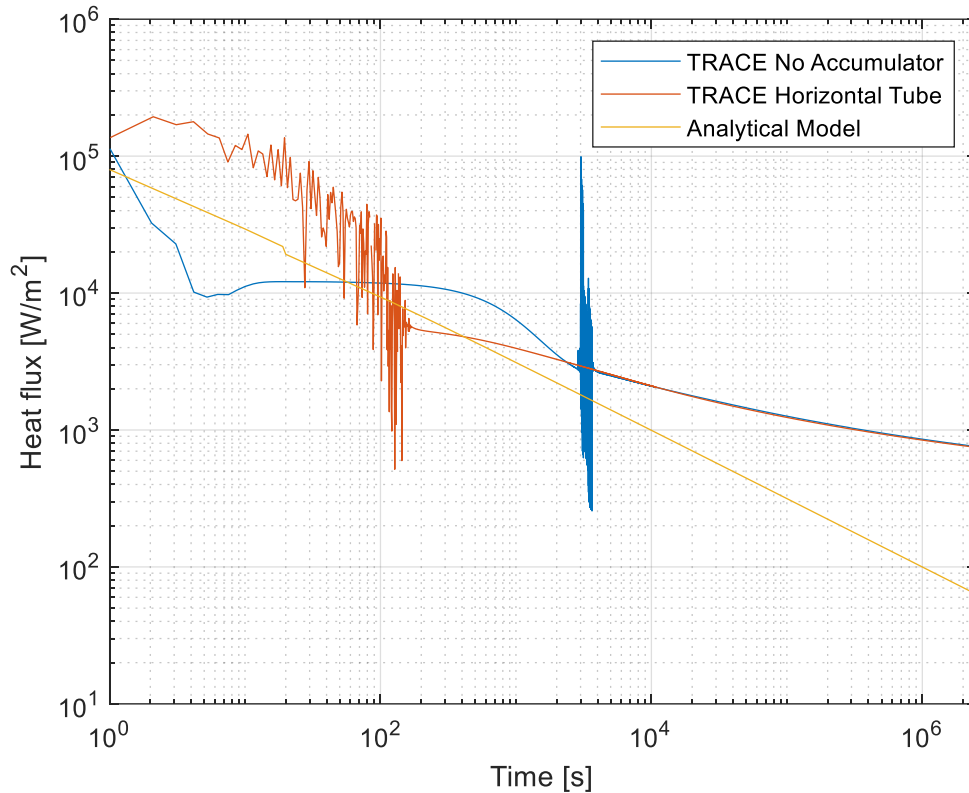


Figure 5.16 Radial heat flux in the 1st node over time, comparison of analytical and numerical results, 1 month simulation.

Figure 5.16 shows a comparison of analytical and TRACE numerical simulation results for a single pipe. Each pipe type selected in TRACE code employs a different condensation model. The “No Accumulator” pipe utilises the default falling film condensation model. In this model the falling film condensate accumulates as a significant film along the pipe wall. Whilst the “Horizontal Tube” is validated for stratified condensing steam heat transfer. The horizontal stratified flow regime prevails where the condensed film on the wall drains along the tube wall and accumulates at the bottom pool, leaving the upper part of the tube more exposed to the steam with relatively very thin film. Which explains the higher heat flux observed in the initial part of the simulation using the “Horizontal Tube”. The correlation used in this case is Jaster and Kosky correlation (USNRC, 2019).

The discrepancy between the two TRACE profiles in Figure 5.16 is mainly observed within the first 2000 s since the wall temperatures are not that high and thus the condensate film thermal resistance plays a more decisive role in the heat transfer, however as wall temperature rises with time and it reaches the same value after 1 hr for both the “No

Accumulator” and “Horizontal Tube” (Figure 5.18), at that point, the ground thermal resistance is significantly large, and the discrepancy between the two models is no longer holding. This results in both models yielding the same results. It is worth mentioning that more oscillations are observed in the “Horizontal Tube” calculations, which can be explained by the way the correlation is implemented into TRACE calculation algorithm where a temperature ratio has to be multiplied by the correlation since it depends on the temperature. In the theory manual page 396 it is mentioned that *“In general, condensation heat transfer can be very oscillatory and inclusion of this ratio into TRACE wall heat transfer contributed to the oscillations”*(USNRC, 2019)

Although calculations using the “Horizontal Tube” would be more representative for the low vapour velocity case in this study, it was observed that calculations using such model are more computationally expensive and require more nodes in the radial direction for the results to converge. It was also more difficult for the results to converge with the presence of NCG and thus the decision to carry on with “No Accumulator” type for the rest of the simulations in the study. This was after a thorough examination along the length of the tube of the two models for a case over a one-month time simulations where the results between the two models did not vary significantly after 1 hr as can be seen in Figure 5.16 .

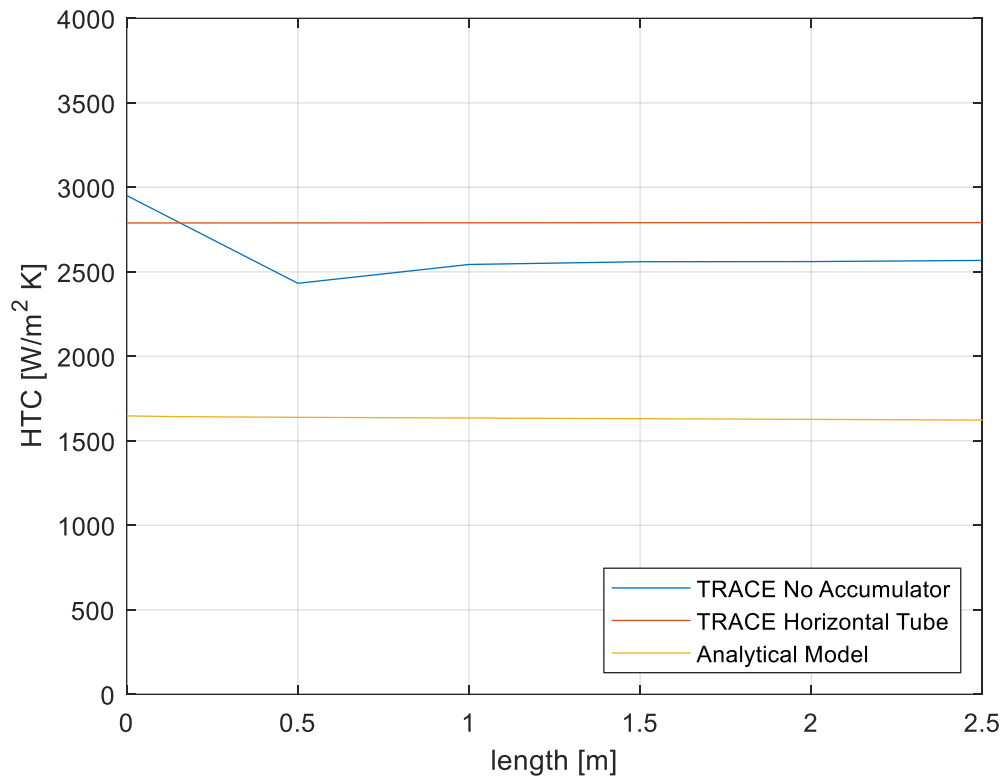


Figure 5.17 Axial profile of radial heat flux 1 hr after shutdown for partial length of the tube, comparison of analytical and numerical solutions.

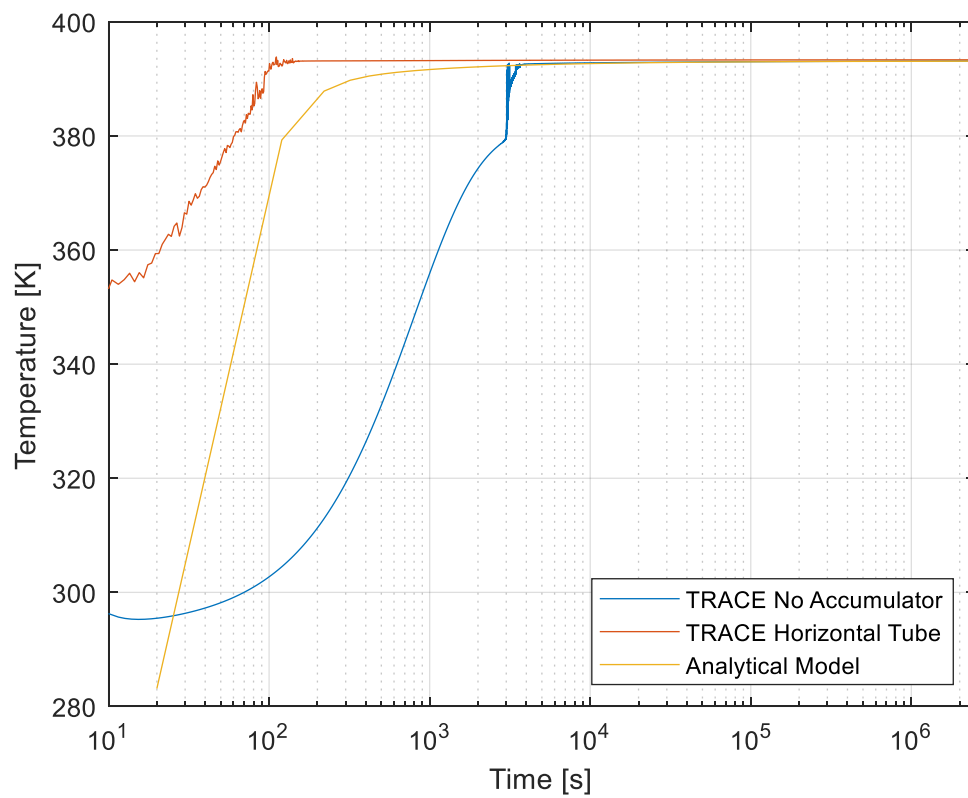


Figure 5.18 Inner wall temperature over time in the 1st node for numerical and analytical solutions.

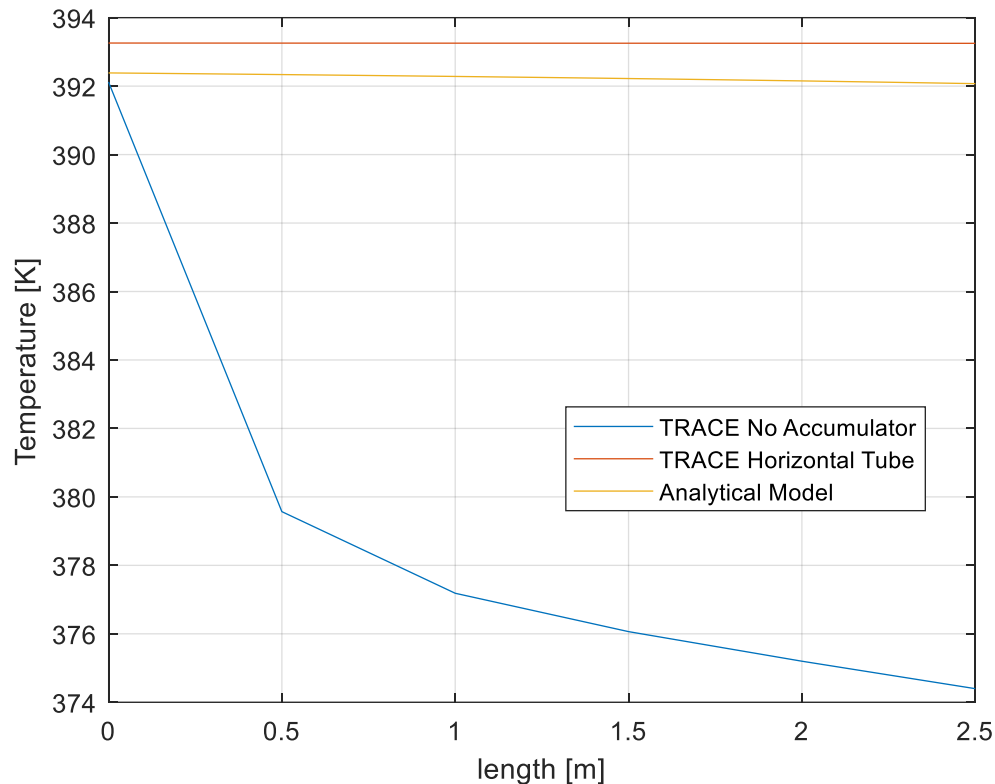


Figure 5.19 Axial profile of inner wall temperature for analytical and numerical solutions.

Figure 5.17, Figure 5.18, and Figure 5.19 show that the analytical model solution is more similar to the TRACE "Horizontal Tube" model than to the "No Accumulator" option. Since the analytical solution and the Horizontal tube model in the code both account for the stratified regime. The two correlations used after all are also very similar Chato Eq.(3.7) and Jaster and Kosky Eq. (4.1).

The "No accumulator" model however uses the falling film model, which is more suitable for the annular regime as is the case in vertical pipes. In this regime, the film forms along the walls of the tube for both top and bottom parts and continues to grow in that direction downstream, adding an extra layer of film thermal resistance between the bulk fluid temperature and the wall temperature. This explains the relatively low inner surface wall temperature compared to the top part of the tube as can be seen in Figure 5.19.

In the following sections, results for different soil materials, pressure values, inclination angle and varying NCG + steam mixtures are examined. The plotted radial heat flux from TRACE results was recorded at the inner surface of the pipe wall.

Different soil materials

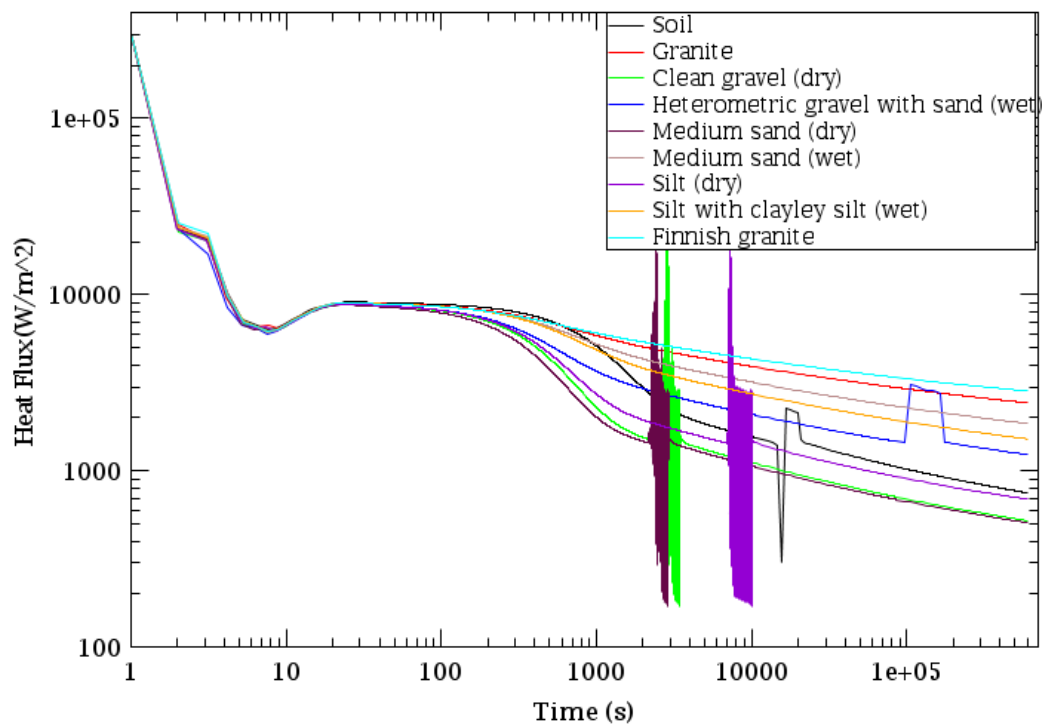


Figure 5.20 Comparison of radial heat flux over time in the 1st node for different ground materials.

Figure 5.20 shows that overall, the heat flux for all soil materials deteriorates over time due to the temperature rise in the inner wall temperature as ground material heats up quickly after the initiation of the event. Each soil material results in a varying heat flux across the outer surface pipe. The oscillations in the heat flux are only observed for materials that are dry, with relatively lower thermal properties which could explain the oscillations due to some convergence issues when the thermal properties are very low.

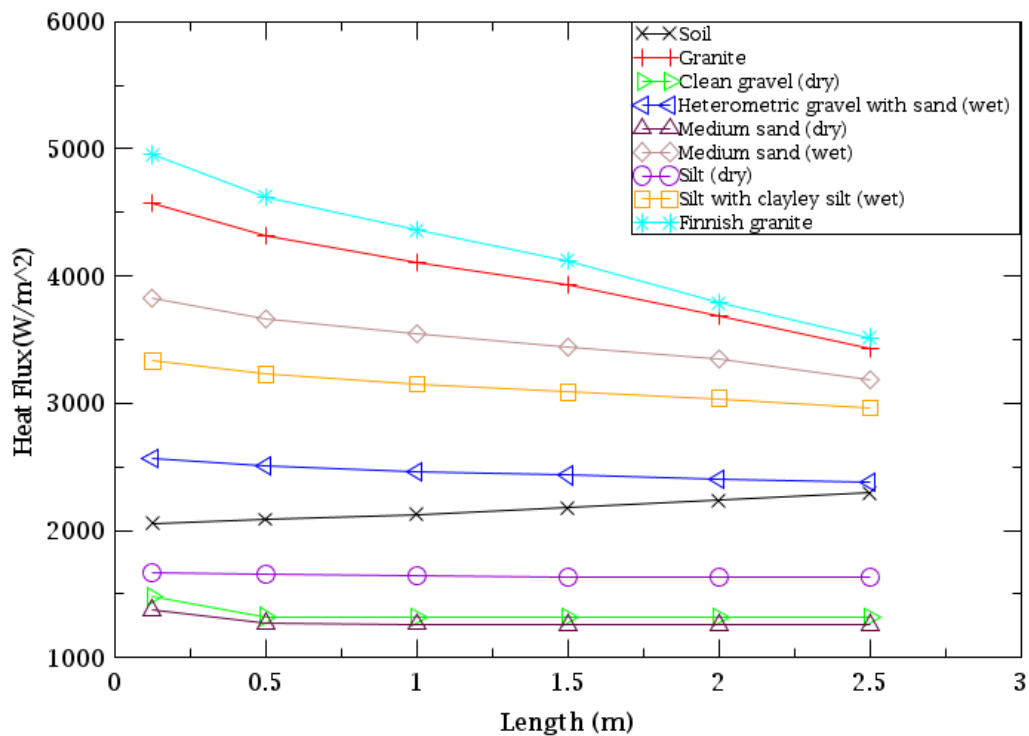


Figure 5.21 Axial profile of radial flux for the initial part of the tube tested with different ground materials, 1 hr after shutdown.

Figure 5.21 examines the axial heat flux for all considered materials 1 hr after shutdown. Clearly, the most favourable option is granite which has a relatively high thermal conductivity. Dry sand and gravel on the other hand, tend to be at the very lower end of the spectrum with very poor conductivity resulting in a heat flux 1/3 of that of granite. It is also worth noting that the presence of water in the soil material tends to enhance the thermal properties of the ground material. Based on this analysis, granite is clearly the most favourable option from a heat transfer point of view. Additionally, locating the underground reactor in a depth corresponding to a bedrock of granite offers several other benefits according to a separate study. With a bedrock location of 100 m to 300 m deep, the reactor has a greater margin of safety for design-basis as well as beyond design basis accidents and particularly better protection against seismic hazards or other external hazards. (Myers & Mahar, 2017).

Different pressures

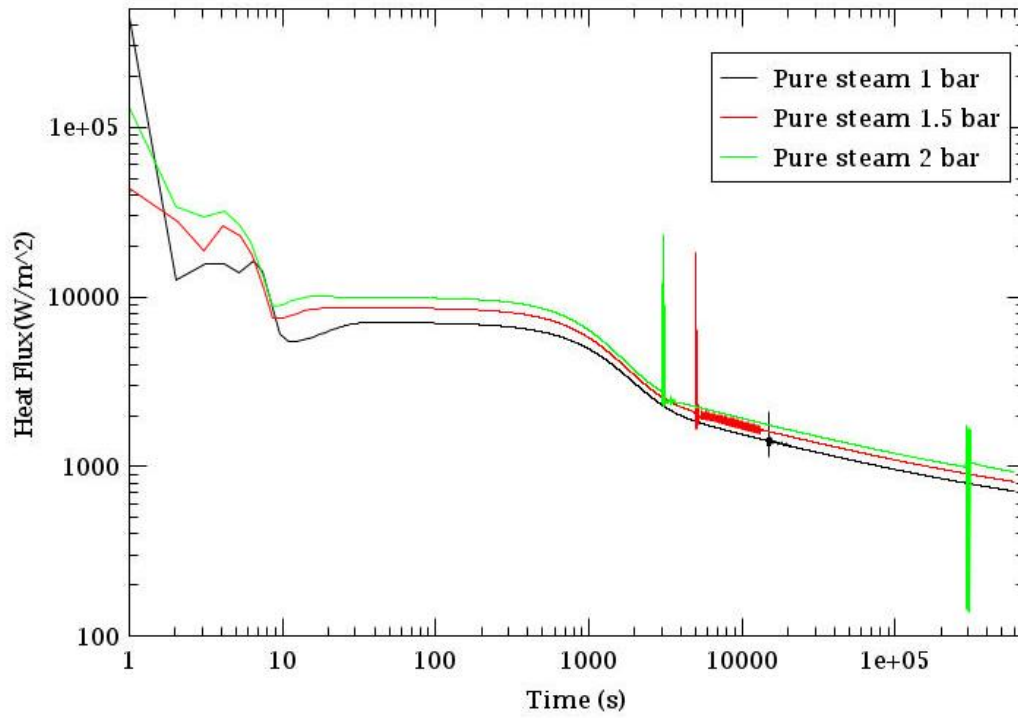


Figure 5.22 Comparison of heat flux over time in the 1st node for different saturation pressures.

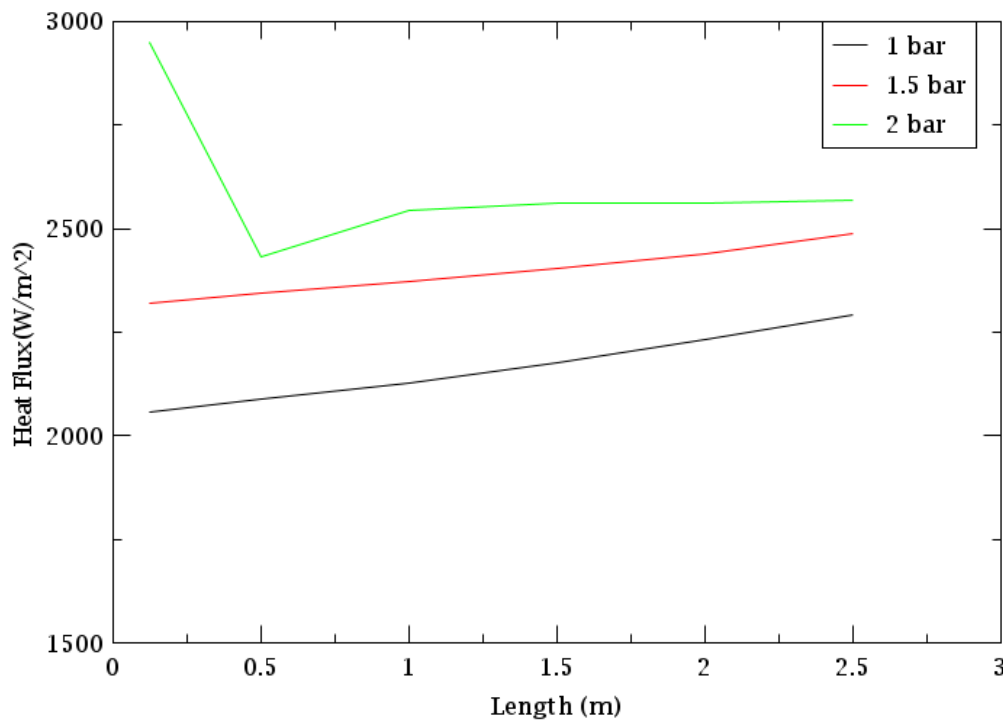


Figure 5.23 Axial profile of radial heat flux for different saturation pressures 1 hr after shutdown.

Figure 5.22 and Figure 5.23 show that higher pressure results in higher saturation temperature and consequently a higher temperature gradient which enhances the heat transfer rate

Inclination angle effect

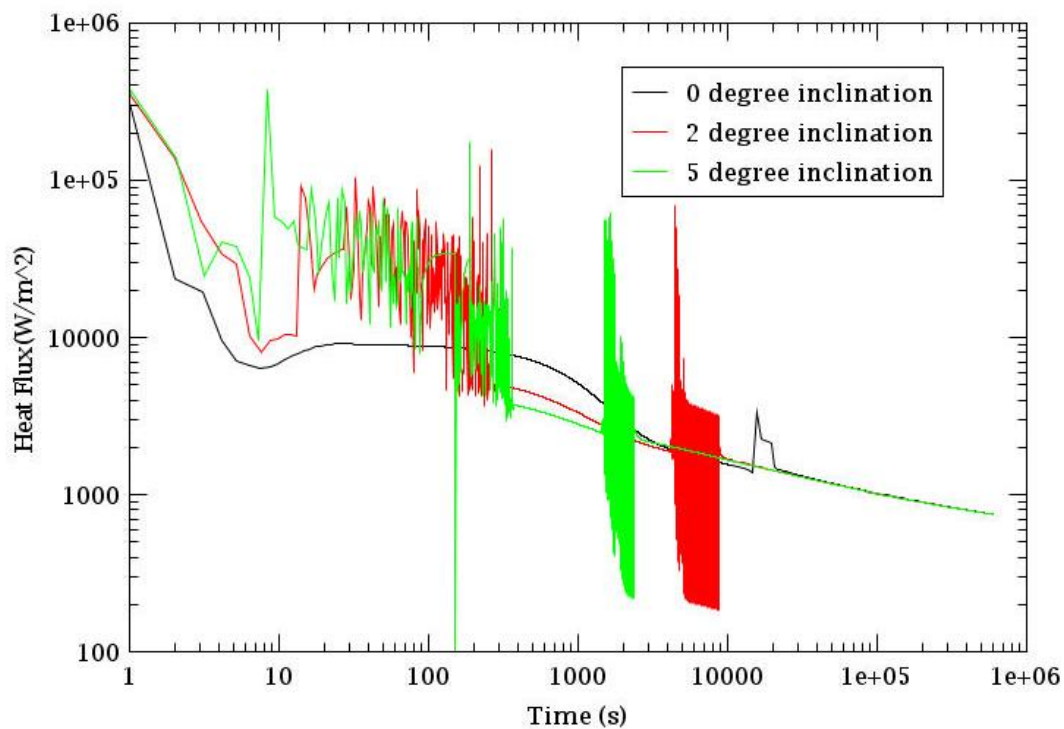


Figure 5.24 Comparison of heat flux over time in the 1st node for different inclination angles.

Figure 5.24 shows that pipes with an inclination angle have higher heat flux within the first 2 min compared to the perfectly horizontal pipe. The inclination angle enhances the heat transfer initially since it helps removing the condensing film faster as it flows downward with the help of gravity, the wall temperature at this point is also relatively cool. However, since the film is removed, the inner wall is more exposed to the hot steam and the temperature of the soil rises faster as in the case of the horizontal pipe where the condensate film acts as an insulation. Which explains the deterioration of the heat flux after 300 s where both inclined pipes have lower flux than the horizontal pipe. Before all 3 cases have the same heat flux roughly 1 hr after shutdown, when the wall temperature reaches the same value for the three cases.

It should be noted that the inclination angle activates the stratified condensation model although the “No Accumulator” was selected. Jaster and Kosky correlation for this model is reported to compare particularly well to experimental data with inclination in TRACE theory manual (USNRC, 2019).

Although there may not be a significant benefit for heat transfer in this case with an inclined angle, the final loop system should have a slight inclination to help with the flow of the condensate downward.

Non-Condensable gases effect

The effect of NCG was tested for different ground materials (soil and granite) which are both at the opposite ends of the spectrum in terms of thermal properties. It is also worth noting that when specifying the amount of NCG in the system, the partial pressure is used in TRACE calculations rather than mass fraction since the code specifies it in that way.

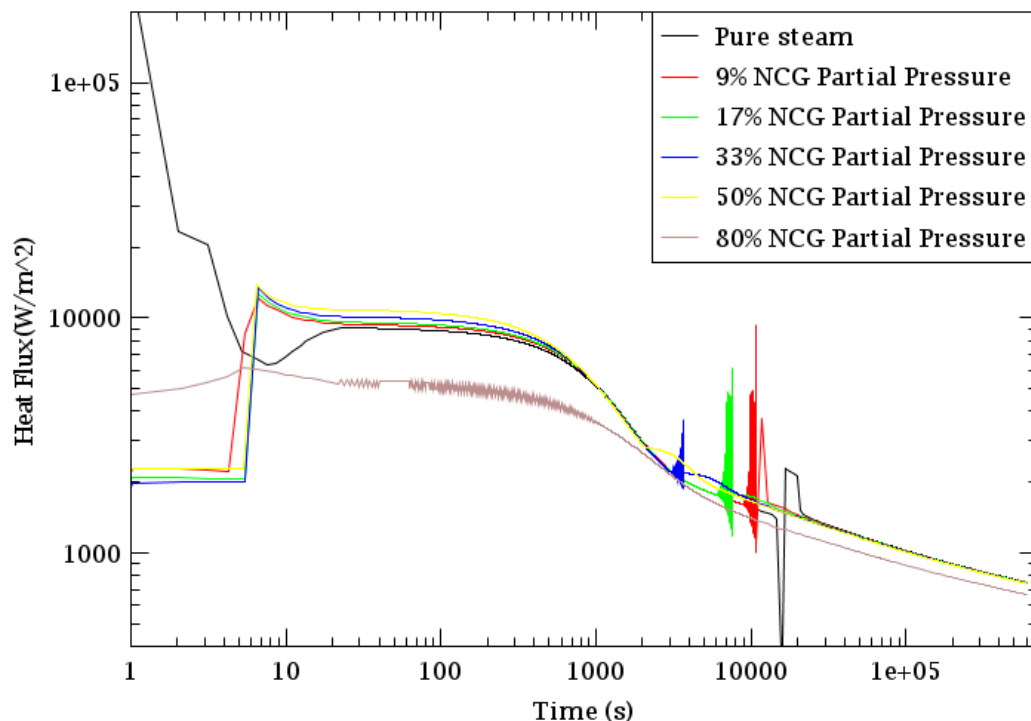


Figure 5.25 Comparison of heat flux over time in the 1st node for varying (Steam + NCG) fractions with selected ground material “soil (mixture)”.

Figure 5.25. shows that NCG partial pressure fractions up to 50 % of the (steam + air) mixture had almost no effect on the heat transfer as compared to the pure steam case. As steam condenses internally in a tube, the water accumulates at the bottom due to gravitational forces, the steam remains in the top part but the air being denser than steam accumulates at the liquid-steam interface forming an additional layer of thermal resistance (Ren et al., 2015). Since the soil material had relatively lower thermal properties (heat conductivity, specific heat capacity), this made the NCG thermal resistance insignificant in this case. It is only for fractions up to 80 % partial pressure where the effect is observed. The same pattern is observed when the ground material is changed to granite Figure 5.26.

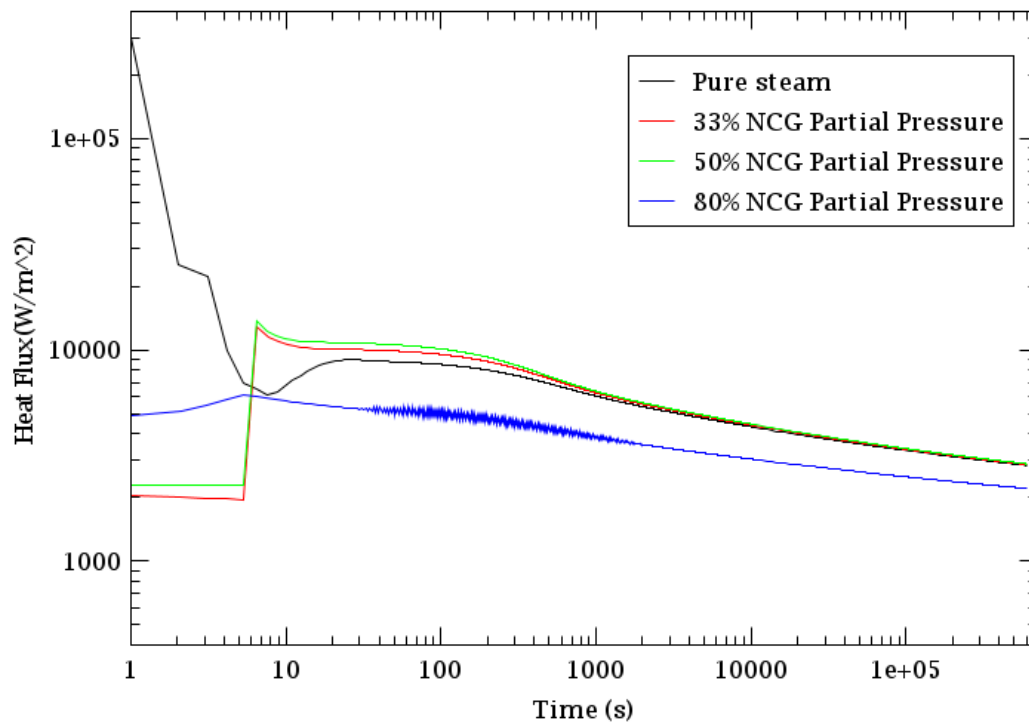


Figure 5.26 Comparison of heat flux over time in the 1st node for varying (Steam + NCG) fractions with selected ground material “Finnish granite”.

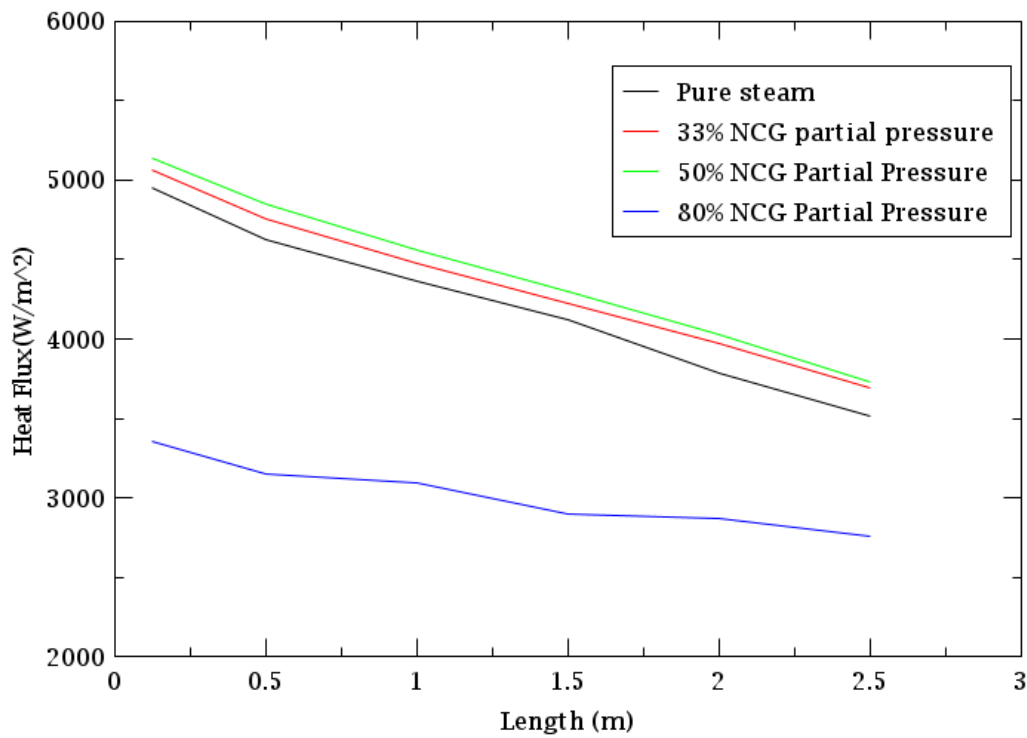


Figure 5.27 Axial profile of radial heat flux for initial partial length of the tube for different (Steam + NCG) mixtures 1 hr after shutdown, with selected ground material Finnish granite.

The NCG effect simulation was run for both the soil (mixture) material as well as Finnish granite. The hypothesis was that the NCG effect could be more evident in the case of granite since it has relatively superior thermal properties than other soils and therefore the variation extent is examined. Nevertheless, after running the simulations, although NCG effect was slightly more evident in the case of granite, it remained insignificant as can be seen in Figure 5.26 and Figure 5.27. After one hour, 80 % partial pressure NCG (air) reduces the heat flux only by 30 % of that of pure steam case.

An 80 % partial pressure results in a mass fraction of around 87 % air when using Eq. (5.2), which provides the NCG mass fraction based on the partial pressure according to (Siddique et al., 1993):

$$W_{nc} = \frac{P_{tot} - P_s(T_{in})}{P_{tot} - \left(1 - \frac{M_s}{M_{nc}}\right) P_s(T_{in})} \quad (5.2)$$

Comparison of NCG effect in TRACE and analytical model

The main difference between the analytical results and the numerical simulations is that the ground material heats up more rapidly and the ground HTC deteriorates faster in the case of the analytical solution. This is due to the way the ground HTC is modelled over time according to expression (3.6):

$$h_o = \frac{k}{\sqrt{\pi at}} \quad (3.6)$$

On the other hand, the numerical solution takes into account the heat conductance through the ground material over time. TRACE code solves the time dependent diffusion equation which results in slower heating of the ground material as in the analytical case and the ground HTC is not as badly deteriorating in this case. Therefore, the heat exchanger surface area needed to remove the decay heat based on TRACE calculations reduces to essentially a quarter of that obtained via the analytical solution.

Since the ground material does not heat as rapidly as the case in the analytical solution, the effect of NCG is a bit more evident in TRACE simulations. Although small amounts up to 50 % partial pressure of air have almost no influence on the heat flux, the effect of a partial pressure of 80 % can be observed when tested for the ground material with the best conductivity (Finnish Granite).

5.2.2. Loop simulation results

The results for the overall cooling loop model are presented in this section. The geometry needed for the loop to remove decay heat in this case for one month period based on previous TRACE single pipe simulations, is presented in Table 5.2. The surface area needed in this case is about $\frac{1}{4}$ the surface area needed in the case of the analytical calculations.

Table 5.2 Proposed GHE geometrical parameters based on TRACE solution.

Number of pipes	Pipe length [m]	Di [mm]	Do [mm]
120	15	20	23

Reactor core power and GHE heat removal rate

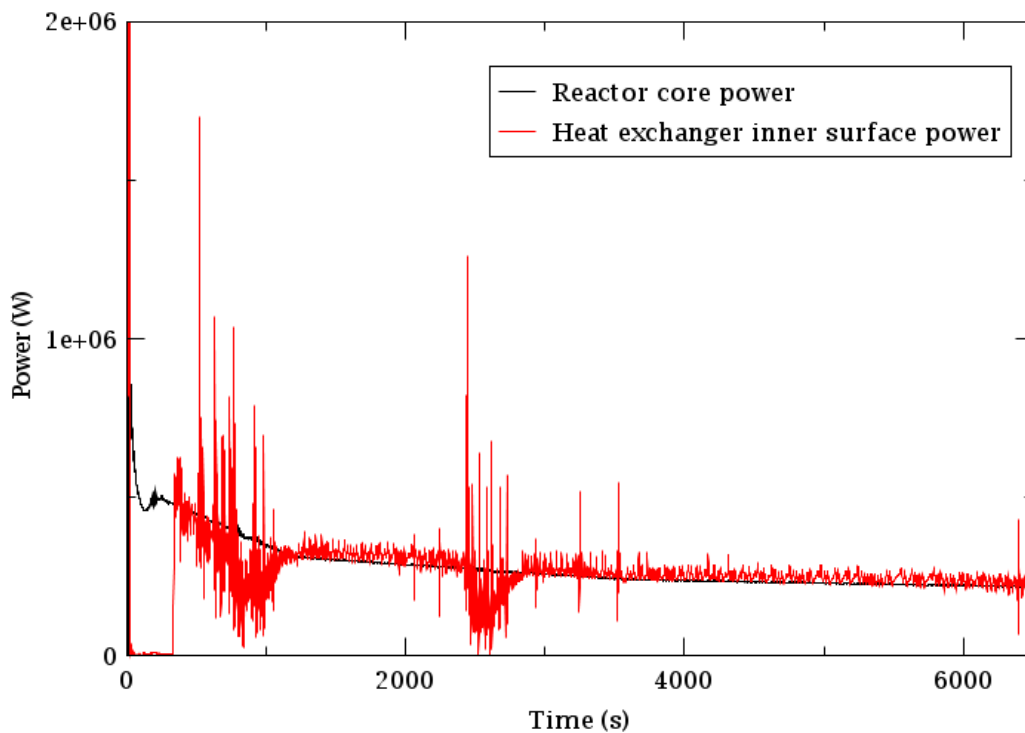


Figure 5.28 Reactor decay power and condenser heat removal rate over time.

In Figure 5.28, the plot in black is the decay heat power generated in the reactor core whilst the plot in red represents the heat removal rate of the heat exchanger. During the time of simulation, it can be seen that all the decay heat is adequately removed through the heat exchanger. Initially, after the initiation of the event, the heat removed is almost zero for a brief short period since the condenser tubes are mostly filled with air, before the steam generated in the reactor reaches the condenser tubes.

Gas mixture and liquid mass flow

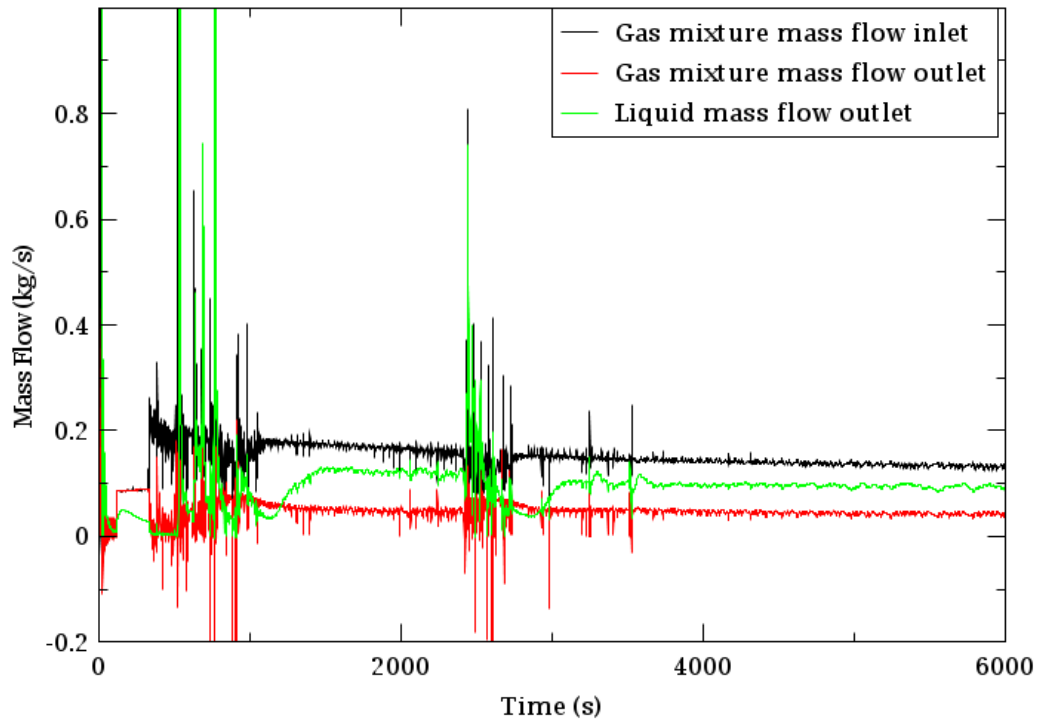


Figure 5.29 Gas and liquid mass flows across condenser tubes over time.

From Figure 5.29, it can be seen that all the steam entering at the condenser inlet is turned into liquid at the outlet, the remaining gas flow at the outlet is only air, which demonstrates that the proposed cooling loop for the decay heat removal system is working effectively in spite of the presence of the non-condensable gas in the mixture.

Initially, several oscillations are observed after the initiation of the event for liquid and gas mass flow, these are most likely attributed to condensation-induced water hammer (Tiselj & Martin, 2012). The phenomenon occurs when hot steam enters the pipe where there is already cold condensate and cooler wall temperature, resulting in the steam condensing abruptly and hence the pressures collapsing rapidly in the tube which creates these heavy abrupt oscillations. This phenomenon is captured by TRACE.

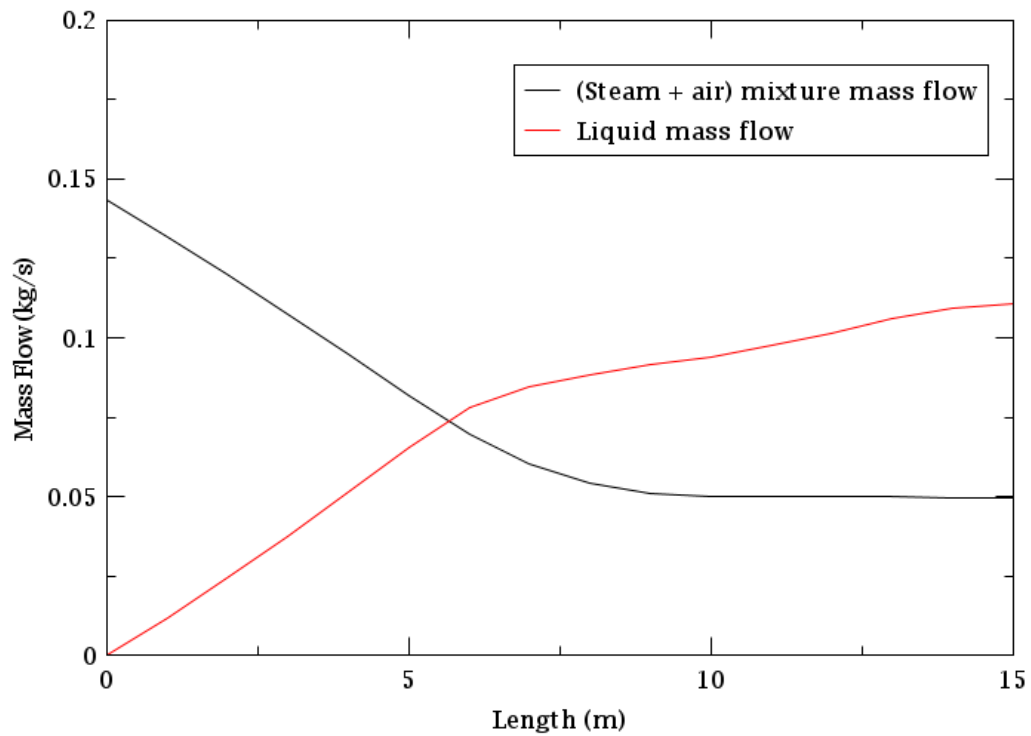


Figure 5.30 Axial profile of gas and liquid mass flows across the condenser tubes, 1 hr after shutdown.

Axial profile taken after 1 hr (Figure 5.30) shows the mass flow of the gas mixture reducing along the length of the pipe as the steam condenses, the value then plateaus at around 8 m along the pipe which means by that point all the steam condensed and mostly air remains. This is in fact consistent with the analytical solution, where the steam 1 hr after shutdown was shown to have all condensed by roughly the same length as illustrated in Figure 5.3.

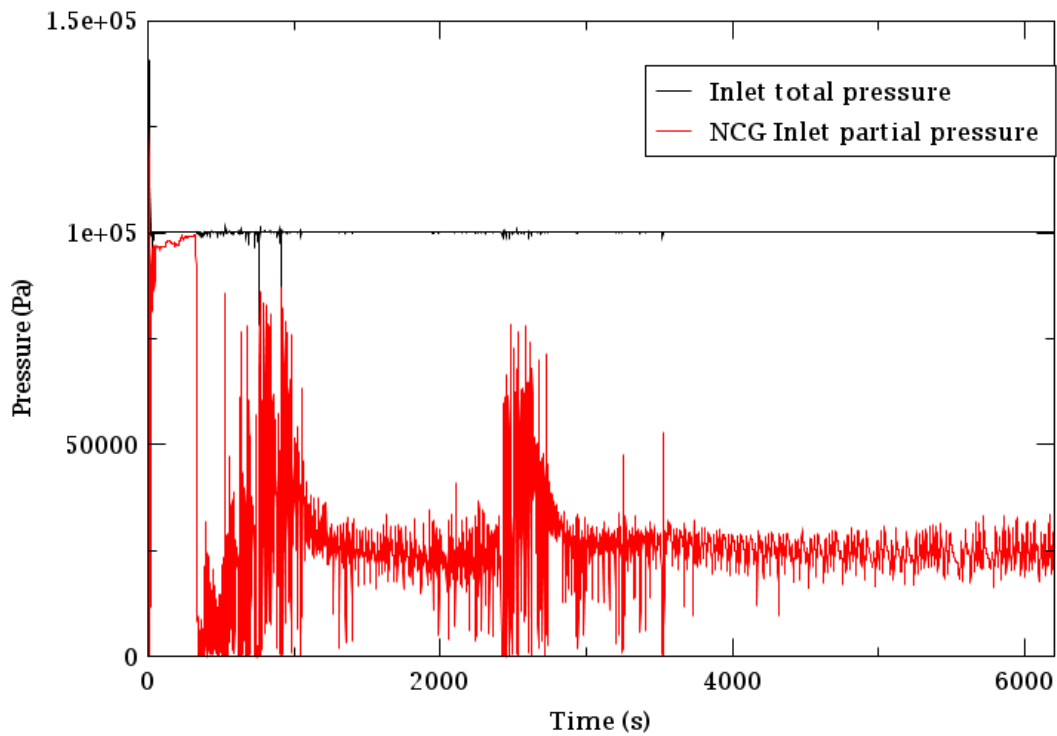


Figure 5.31 Condenser tubes inlet pressure over time.

Figure 5.31 illustrates the total pressure of the flow at the inlet of the condenser tube as well as the partial pressure of the NCG in the mixture. The initial conditions of the condenser tube specified in TRACE input model before the simulation starts are assumed to be pure steam at 2 bar. Therefore, right after the simulation starts, the steam in the condenser tubes is condensed instantly, collapsing the pressure in the tubes which rapidly draws air from the injection line due to the pressure difference. This explains the high amount of NCG observed at the start of the simulation, where the total pressure of the flow at the condenser tube inlet seems to be mostly NCG before steam generated in the reactor reaches the condenser tubes around 300s after the start of the event. The partial pressure of NCG is roughly around 25 %. This amount is postulated to increase over time as the amount of steam generated will be reducing proportionally to the decay power.

GHE heat flux and temperature

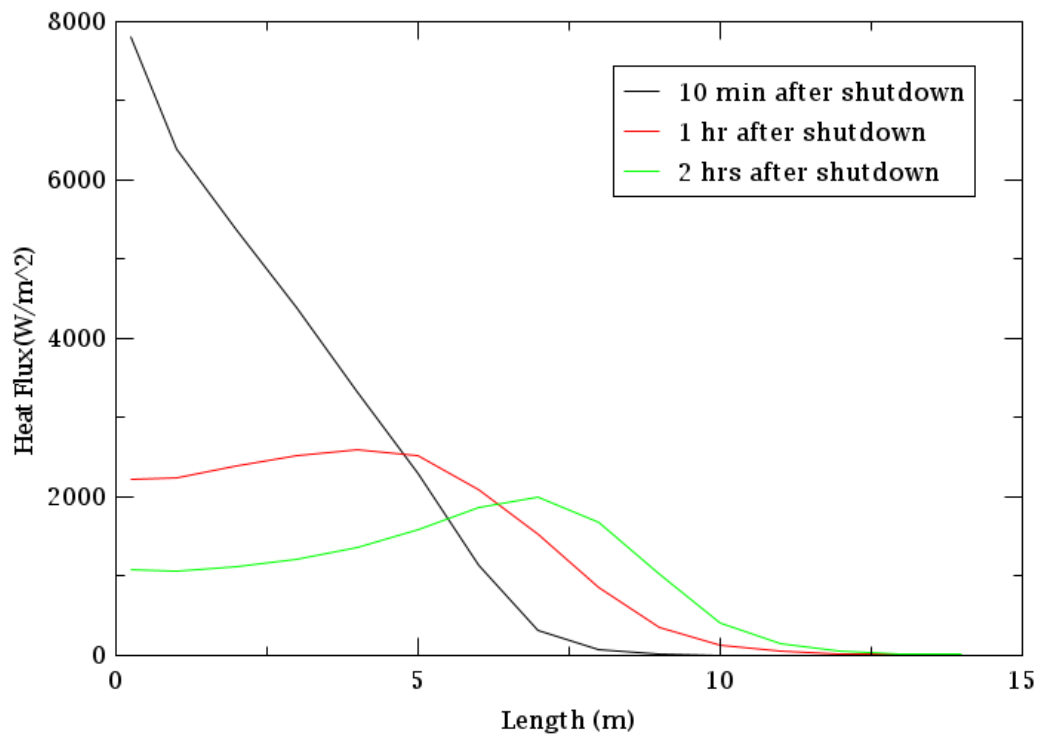


Figure 5.32 Axial profile of radial heat flux across condenser tubes.

Figure 5.32 shows the axial profiles for the heat flux across the inner wall heat exchanger pipes at three different times. Initially heat flux peak is at the initial part of the pipe where most of the heat is ejected however over time as this part heats up and the temperature gradient reduces, more heat will be ejected towards the end part of the pipe that remains relatively cooler (Figure 5.33). The overall performance of the loop seems satisfactory and in accordance with the expected results based on the single pipe simulations.

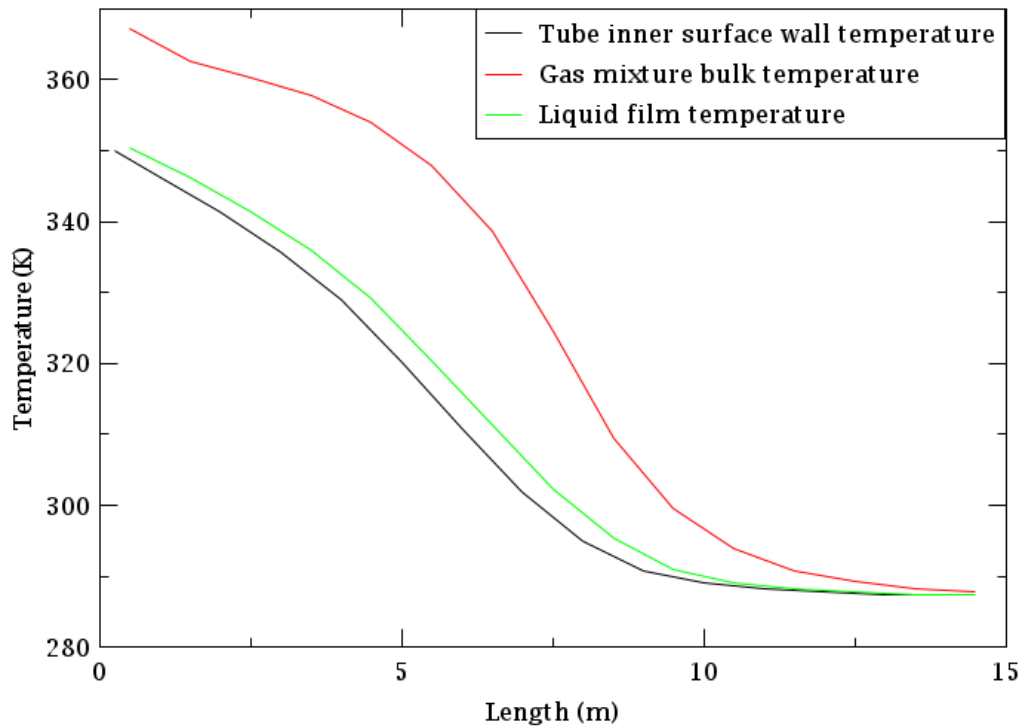


Figure 5.33 Temperature axial profile across condenser tubes, 1 hr after shutdown.

5.3. Limitations and Errors

Although the analysis provided in the analytical and the numerical studies aimed to be as accurate and realistically representative to the best estimate, there are several assumptions embedded within the analyses which are a source of uncertainty and errors:

In the analytical solution, many simplifying assumptions were adopted, which are outlined in section 3, in addition to the mesh size all contribute to the uncertainty of obtained solution. The assumptions state steady state, ignore the cooling of the bulk temperature before the flow is condensed, the pressure is assumed to remain constant.... etc which obviously are not correct.

In addition, all empirical correlations used in the analytical model and numerical simulations have a margin of uncertainty. The uncertainties associated with these correlations vary from one study to another: Shah reported that mean deviation of the correlation when compared against a data set of 474 points was 15.4 %. (Garimella & Fronk, 2015).

In another comparative study (Jeon et al., 2013a) where Chato and Shah correlations were compared to many experimental studies with low vapour velocities where stratified-wavy regimes prevail, it was reported that both correlations predicted the results significantly well with only 3 % deviation. Both correlations also underpredicted the heat transfer coefficient in the same source. This is most likely linked to the fact that Shah correlation does not account for entrainment as noted by Shah (Garimella & Fronk, 2015) and the Chato correlation ignores the cooling through the bottom film.

(Dobson & Chato, 1998) extensively reviewed the use of Chato (1962) and Jaster and Kosky (1976) correlations on a wide range of conditions, they reported that the two models predicted their experimental data within ± 25 % uncertainty when dealing with wavy regime. They also showed that neither model effectively captured the change in heat transfer with quality well and both models did not consider the contribution of the liquid pool. (Garimella & Fronk, 2015)

The simple Nusselt analysis theory is also reported to have up to 50 % inaccuracy according to (M. Ghiaasiaan, 2017). However, the analysis in this work tried to limit that uncertainty by coupling the correlation with the Lee-Kim factor, which takes into account the effect of the interfacial shear stress that was not accounted for in the original theory. The improved latent enthalpy was also employed to account for the subcooling of the condensate film.

Moreover, Lockhart-Martinelli multiplier used for calculating pressure drop in this condensation model, was developed using an adiabatic database of air-water mixture and was not necessarily developed for the condensation process. This creates another source of uncertainty since the mechanisms of adiabatic two-phase flow are different and could potentially result in significant deviations from the real processes during condensing two phase flows. The analytical model tried to account for this uncertainty by performing pressure drop calculations with 50 % safety margin as shown in Figure 3.5. Meaning that there is always more leeway to offset in worst case scenario.

5.4. Future Work

At this stage, the uncertainties associated with the analysis remain large to quantify with good confidence. Further comprehensive experimental and numerical studies will be required in the future to validate the TRACE model and consolidate the findings of this report. Condensation in horizontal tubes with the presence of NCG remains a fairly unexplored field compared to vertical tubes and most of the studies are inconclusive. There has not been many investigations carried out in this area especially for geothermal heat exchangers applications and the phenomenon is yet not fully understood, as reported in (Ren et al., 2015).

Additionally, the analysis in this study was performed with the assumption that each pipe is completely independent from the bundle. Further studies on the settings of the pipe position and feedback from other pipe tubes will be required in this case. The design also requires reliability assessments to determine how many tracks (buses) will be needed.

6. Conclusions

In this report, a reasonable theoretical model was established to perform pressure drop and heat transfer calculations for LUTHER decay heat removal system with natural circulation. Thermal hydraulic system code TRACE was also used to model the proposed DHR system. Qualitatively, the theoretical and numerical results showed similar trend overall, although there was a considerable quantitative difference between the two models. Based on the obtained results, the present study demonstrates feasibility of this system and a preliminary DHR design was proposed.

The effect of NCG was slightly more evident in the numerical simulations performed with TRACE compared to the results obtained from the analytical model. This is because the ground HTC did not deteriorate as significantly in the TRACE simulation as in the analytical calculations. But overall, the presence of NCG up to 80 % mass fraction has little to a very minor effect and did not compromise the overall performance of the loop.

The heat transfer coefficient of the ground material dictates the heat removal of decay heat for most of the time and under most varying conditions. The ground material is a decisive factor in the study of heat transfer for an underground decay heat removal system. The choice of material will depend on the geographical location as well as the geological properties of the chosen depth underground. A wide spectrum of potential ground materials of varying thermal-physical properties has been considered in this study. A solid bedrock of granite seems to be the most favourable option from a heat transfer perspective.

Further experimental work in the future is needed for TRACE validation and to better understand the encountered phenomena.

References

- Ahn, T., Kang, J., Bae, B., Jeong, J. J., & Yun, B. (2019). Steam condensation in horizontal and inclined tubes under stratified flow conditions. *International Journal of Heat and Mass Transfer*, *141*, 71–87.
<https://doi.org/10.1016/j.ijheatmasstransfer.2019.06.056>
- ASHARE. (2017). *ASHRAE Handbook Fundamentals*.
- Ayhan, H., & Sökmen, C. N. (2016). Design and modeling of the passive residual heat removal system for VVERs. *Annals of Nuclear Energy*, *95*, 109–115.
<https://doi.org/10.1016/j.anucene.2016.05.003>
- Bae, B. U., Kim, S., Park, Y. S., & Kang, K. H. (2020). Experimental investigation on condensation heat transfer for bundle tube heat exchanger of the PCCS (Passive Containment Cooling System). *Annals of Nuclear Energy*, *139*, 107285.
<https://doi.org/10.1016/j.anucene.2019.107285>
- Bai, J., Zhao, B., & Wang, J. (2017). Study on the performance of an open-loop passive containment cooling system. *Journal of Nuclear Science and Technology*, *3131*(October), 113–121. <https://doi.org/10.1080/00223131.2017.1386133>
- Bai, J., Zhao, B., & Wang, J. (2018). Study on the performance of an open-loop passive containment cooling system. *Journal of Nuclear Science and Technology*, *55*(1), 113–121. <https://doi.org/https://doi.org/10.1155/2014/358365>
- Bajs, T., Debrecin, N., & Šegon, V. (2000). *ASSESSMENT OF DISCRETIZATION APPROACH FOR RELAP5 / MOD3 COMPUTER CODE*.
- Bang, J., Hwang, J. H., Kim, H. G., & Jerng, D. W. (2021). Parametric analyses for the design of a closed-loop passive containment cooling system. *Nuclear Engineering and Technology*, *53*(4), 1134–1145. <https://doi.org/10.1016/j.net.2020.09.007>
- Bergman, T. L., & Lavine, A. S. (2017). *Fundamentals of heat and Mass Transfer* (Eighth). Wiley.
- Butterworth, D. (1975). A comparison of some void-fraction relationships for co-current

- gas-liquid flow. *International Journal of Multiphase Flow*, 1(6), 845–850.
[https://doi.org/10.1016/0301-9322\(75\)90038-5](https://doi.org/10.1016/0301-9322(75)90038-5)
- Cavallini, A., Censi, G., Del Col, D., Doretti, L., Longo, G. A., & Rossetto, L. (2002). Condensation of halogenated refrigerants inside smooth tubes. *HVAC and R Research*, 8(4), 429–451. <https://doi.org/10.1080/10789669.2002.10391299>
- Cavallini, A., Del Col, D., Doretti, L., Matkovic, M., Rossetto, L., Zilio, C., & Censi, G. (2006). Condensation in horizontal smooth tubes: A new heat transfer model for heat exchanger design. *Heat Transfer Engineering*, 27(8), 31–38.
<https://doi.org/10.1080/01457630600793970>
- Cengel, Y. A., & Ghajar, A. J. (2020). *Heat and Mass Transfer, Fundamentals and Applications* (sixth). McGraw-Hill Education.
- Chato, J. . (1962). Laminar condensation inside horizontal and inclined tubes. *ASHRAE Journal*, 4(2), 52–60.
- Chen, W., Hui, K., Wang, B., Zhao, Q., Chong, D., & Yan, J. (2021). Review of the tube external condensation heat transfer characteristic of the passive containment cooling system in nuclear power plant. *Annals of Nuclear Energy*, 157, 108226.
<https://doi.org/10.1016/j.anucene.2021.108226>
- Collier, J. G., & Thome, J. R. (1994). *Convective Boiling and Condensation* (third). Clarendon Press.
- Dalla Santa, G., Galgaro, A., Sassi, R., Cultrera, M., Scotton, P., Mueller, J., Bertermann, D., Mendrinos, D., Pasquali, R., Perego, R., Pera, S., Di Sipio, E., Cassiani, G., De Carli, M., & Bernardi, A. (2020). An updated ground thermal properties database for GSHP applications. *Geothermics*, 85(September 2019), 101758.
<https://doi.org/10.1016/j.geothermics.2019.101758>
- Dobson, M. K., & Chato, J. C. (1998). Condensation in smooth horizontal tubes. *Journal of Heat Transfer*, 120(1), 193–213. <https://doi.org/10.1115/1.2830043>
- Finnish Energy. (2021a). *Energy Year 2020 - District Heating*.
- Finnish Energy. (2021b). *Energy Year 2020 - Electricity* (p. 33).
https://energia.fi/en/newsroom/publications/energy_year_2020_-

[_electricity.html#material-view](#)

- Garimella, S., & Fronk, B. (2015). Internal Flow Condensation. In J. R. Thome (Ed.), *Encyclopedia of Two-Phase Heat Transfer and Flow I Fundamentals and Methods Volume 2: Condensation Heat Transfer* (Issue 1, pp. 165–230).
https://doi.org/10.1142/9789814623216_0014
- Ghiaasiaan, S. mostafa. (2011). *CONVECTIVE HEAT AND MASS TRANSFER*. Cambridge University press.
- Ha, H., Lee, S., & Kim, H. (2017). Optimal design of passive containment cooling system for innovative PWR. *Nuclear Engineering and Technology*, 49(5), 941–952.
<https://doi.org/10.1016/j.net.2017.03.005>
- Huang, J., Zhang, J., & Wang, L. (2015). Review of vapor condensation heat and mass transfer in the presence of non-condensable gas. *Applied Thermal Engineering*, 89, 469–484. <https://doi.org/10.1016/j.applthermaleng.2015.06.040>
- Hyvärinen, J. (2020). *Energy Technology Project Works: Vol. BH10A1601*.
- Hyvärinen, J., & Truong, T. (2020). *SuoMiReaktori , a novel concept for a District Heating Reactor Design and licensing – Introduction to STUK*.
- IAEA. (1991). Safety Related Terms for Advanced Nuclear Plants. *Iaea-Tecdoc-626*, September, 20. http://www-pub.iaea.org/MTCD/publications/PDF/te_626_web.pdf
- IAEA. (2020). Advances in Small Modular Reactor Technology developments. A *Supplement to: IAEA Advanced Reactors Information System (ARIS) 2020 Edition*, 354. <http://aris.iaea.org/>
- Jeon, S. S., Hong, S. J., Park, J. Y., Seul, K. W., & Park, G. C. (2013a). Assessment of horizontal in-tube condensation models using MARS code. Part I: Stratified flow condensation. *Nuclear Engineering and Design*, 254, 254–265.
<https://doi.org/10.1016/j.nucengdes.2012.10.006>
- Jeon, S. S., Hong, S. J., Park, J. Y., Seul, K. W., & Park, G. C. (2013b). Assessment of horizontal in-tube condensation models using MARS code. Part II: Annular flow condensation. *Nuclear Engineering and Design*, 262, 510–524.
<https://doi.org/10.1016/j.nucengdes.2013.05.014>

- Kuhn, S. Z., Schrock, V. E., & Peterson, P. F. (1997). An investigation of condensation from steam-gas mixtures flowing downward inside a vertical tube. *Nuclear Engineering and Design*, 177(1–3), 53–69. [https://doi.org/10.1016/S0029-5493\(97\)00185-4](https://doi.org/10.1016/S0029-5493(97)00185-4)
- Lee, K.-Y., & Kim, M. H. (2011). Steam Condensation in the Presence of a Noncondensable Gas in a Horizontal Tube. *Evaporation, Condensation and Heat Transfer*. <https://doi.org/10.5772/21234>
- Leppänen, J. (2019). A Review of District Heating Reactor Technology. *VTT Technical Research Centre of Finland*.
- Leppänen, J. (2021). *Low-temperature District Heating and Desalination Reactor (LDR) Technology*. https://www.ecosmr.fi/wp-content/uploads/2021/06/Leppanen_EcoSMR_15062021.pdf
- Liebenberg, L., & Meyer, J. P. (2006). The characterization of flow regimes with power spectral density distributions of pressure fluctuations during condensation in smooth and micro-fin tubes. *Experimental Thermal and Fluid Science*, 31(2), 127–140. <https://doi.org/10.1016/j.expthermflusci.2006.03.023>
- Lips, S., & Meyer, J. P. (2011). Two-phase flow in inclined tubes with specific reference to condensation: A review. *International Journal of Multiphase Flow*, 37(8), 845–859. <https://doi.org/10.1016/j.ijmultiphaseflow.2011.04.005>
- Locatelli, G. (2018). *Why are Megaprojects, Including Nuclear Power Plants, Delivered Overbudget and Late? Reasons and Remedies*. 1–28. <http://arxiv.org/abs/1802.07312>
- Locatelli, G., Bingham, C., & Mancini, M. (2014). Small modular reactors: A comprehensive overview of their economics and strategic aspects. *Progress in Nuclear Energy*, 73, 75–85. <https://doi.org/10.1016/j.pnucene.2014.01.010>
- Lockhart, R. W., & Martinelli, R. C. (1949). Proposed correlation of data for isothermal two-phase two component flow in pipes. In *Chemical Engineering Progress* (Vol. 45, pp. 39–48).
- Lu, J., Cao, H., & Li, J. M. (2019). Experimental study of condensation heat transfer of steam in the presence of non-condensable gas CO₂ on a horizontal tube at sub-

- atmospheric pressure. *Experimental Thermal and Fluid Science*, 105(December 2018), 278–288. <https://doi.org/10.1016/j.expthermflusci.2019.04.004>
- M. Ghiaasiaan. (2017). *Two-Phase Flow, Boiling, and Condensation: In Conventional and Miniature Systems* (2nd ed.). Cambridge University press.
- Martinelli, R. C., & Nelson, D. B. (1948). Prediction of Pressure Drop during Forced-Circulation of Boiling Water. *Trans. of the ASME*, 70, 695–702.
- Myers, C. W., & Mahar, J. M. (2017). *SMR2011-6 UNDERGROUND SITING OF SMALL MODULAR REACTORS IN BEDROCK* : 1–10.
- Na, M. W., Shin, D., Park, J. H., Lee, J. I., & Kim, S. J. (2020). Indefinite sustainability of passive residual heat removal system of small modular reactor using dry air cooling tower. *Nuclear Engineering and Technology*, 52(5), 964–974. <https://doi.org/10.1016/j.net.2019.11.003>
- NIST. (2021). *NIST Chemistry WebBook, SRD 69, Thermophysical Properties of Fluid Systems*. <https://webbook.nist.gov/chemistry/fluid/>
- Olivier, S. P., Meyer, J. P., De Paepe, M., & De Kerpel, K. (2016). The influence of inclination angle on void fraction and heat transfer during condensation inside a smooth tube. *International Journal of Multiphase Flow*, 80, 1–14. <https://doi.org/10.1016/j.ijmultiphaseflow.2015.10.015>
- Oosterbaan, H., Janiszewski, M., Uotinen, L., Siren, T., & Rinne, M. (2017). Numerical Thermal Back-calculation of the Kerava Solar Village Underground Thermal Energy Storage. *Procedia Engineering*, 191, 352–360. <https://doi.org/10.1016/j.proeng.2017.05.191>
- Paiho, S., & Reda, F. (2016). Towards next generation district heating in Finland. *Renewable and Sustainable Energy Reviews*, 65, 915–924. <https://doi.org/10.1016/j.rser.2016.07.049>
- Paiho, S., & Saastamoinen, H. (2018). How to develop district heating in Finland? *Energy Policy*, 122(January), 668–676. <https://doi.org/10.1016/j.enpol.2018.08.025>
- Palen, J. W., Breber, G., & Taborek, J. (1979). Prediction of flow regimes in horizontal tube-side condensation. *Heat Transfer Engineering*, 1(2), 47–57.

<https://doi.org/10.1080/01457637908939558>

- Park, J. Y. (2015). Assessments of UCB-Kuhn Condensation Tests by Various Thermal-Hydraulic Codes. *Transactions of the Korean Nuclear Society Spring Meeting*, 8–11.
- Polo, J. (1998). *State of the Art Report On Condensation Phenomena Within Tubes in the Presence of Noncondensables Gas*. 75.
- Prošek, A. (2020). *Nuclear Safety - Use of computer codes for deterministic safety analysis*. 01, 1–81. <https://predmeti.fmf.uni-lj.si/JVa>
- Ren, B., Zhang, L., Cao, J., Xu, H., & Tao, Z. (2015). Experimental and theoretical investigation on condensation inside a horizontal tube with noncondensable gas. *International Journal of Heat and Mass Transfer*, 82, 588–603.
<https://doi.org/10.1016/j.ijheatmasstransfer.2014.11.041>
- Rifert, V., & Sereda, V. (2019). *Heat transfer during film condensation inside plain tubes . Review of experimental research*. 1.
- Sambuu, O., & Obara, T. (2015). Comparative study on HTGR designs for passive decay heat removal. *Progress in Nuclear Energy*, 82, 37–45.
<https://doi.org/10.1016/j.pnucene.2014.07.013>
- Sereda, V., Rifert, V., Gorin, V., Baraniuk, O., & Barabash, P. (2021). Heat transfer during film condensation inside horizontal tubes in stratified phase flow. *Heat and Mass Transfer/Waerme- Und Stoffuebertragung*, 57(2), 251–267.
<https://doi.org/10.1007/s00231-020-02946-2>
- Shabestary, A. M., Viereckl, F., Zhang, Y., Manthey, R., Lucas, D., Schuster, C., Leyer, S., Hurtado, A., & Hampel, U. (2019). Modelling of passive heat removal systems: A review with reference to the framatome KERENA BWR reactor: Part i. *Energies*, 13(1). <https://doi.org/10.3390/en13010035>
- Shah, M. M. (1979). A general correlation for heat transfer during film condensation inside pipes. *International Journal of Heat and Mass Transfer*, 22(4), 547–556.
[https://doi.org/10.1016/0017-9310\(79\)90058-9](https://doi.org/10.1016/0017-9310(79)90058-9)
- Shen, S., Wang, Y., & Yuan, D. (2017). Circumferential distribution of local heat transfer coefficient during steam stratified flow condensation in vacuum horizontal tube.

- International Journal of Heat and Mass Transfer*, 114, 816–825.
<https://doi.org/10.1016/j.ijheatmasstransfer.2017.06.042>
- Shiralkar, B., Cheung, Y. K., Marquino, W., & Klebanov, L. (2007). *NATURAL CIRCULATION IN ESBWR Bharat Shiralkar ICONE15-10439 NATURAL CIRCULATION IN ESBWR GE Energy – Nuclear*.
- Siddique, M., Golay, M. W., & Kazimi, M. S. (1993). Local heat transfer coefficients for forced-convection condensation of steam in a vertical tube in the presence of a noncondensable gas. *Nuclear Technology*, 102(3), 386–402.
<https://doi.org/10.13182/NT93-A17037>
- Silvonen, T. (2011). *Reliability analysis for passive systems – A case study on a passive containment cooling system*.
- Sparrow, E. M., Minkowycz, W. J., & Saddy, M. (1967). Forced convection condensation in the presence of noncondensables and interfacial resistance. *International Journal of Heat and Mass Transfer*, 10(12), 1829–1845. [https://doi.org/10.1016/0017-9310\(67\)90053-1](https://doi.org/10.1016/0017-9310(67)90053-1)
- The White House. (2021). Promoting Small Modular Reactors for National Defense and Space Exploration. *Federal Register, Presidential Documents*, 86(9), 3727–3731.
<https://doi.org/10.4324/9780203122273>
- Thom, J. R. S. (1964). Prediction of pressure drop during forced circulation boiling of water. *International Journal of Heat and Mass Transfer*, 7(7), 709–724.
[https://doi.org/10.1016/0017-9310\(64\)90002-X](https://doi.org/10.1016/0017-9310(64)90002-X)
- Thome, J. R., & Cioncolini, A. (2015). *Two-Phase Flow Pattern Maps for Macrochannels*. 47–84. https://doi.org/10.1142/9789814623216_0020
- Tiselj, I., & Martin, C. S. (2012). Slug modeling with 1D two-fluid model. *Kerntechnik*, 77(2), 101–107. <https://doi.org/10.3139/124.110238>
- Truong, T., Suikkanen, H., & Hyvärinen, J. (2021). Reactor Core Conceptual Design for a Scalable Heating Experimental Reactor, LUTHER. *Journal of Nuclear Engineering*, 2(2), 207–214. <https://doi.org/10.3390/jne2020019>
- Tulkki, V., Pursiheimo, E., & Lindroos, T. (2017). District Heat with Small Modular

- Reactors (SMR). *VTT Technical Research Centre of Finland*.
<https://www.vtt.fi/inf/julkaisut/muut/2017/OA-District-heat-with-Small.pdf>
- USNRC. (2019). *TRACE V5.1341 THEORY MANUAL, Field Equations , Solution Methods , and Physical Models*.
<https://www.nrc.gov/docs/ML1200/ML120060218.pdf>
- Värri, K., & Syri, S. (2019). The possible role of modular nuclear reactors in district heating: Case Helsinki region. *Energies*, 12(11), 1–24.
<https://doi.org/10.3390/en12112195>
- Wu, T., & Vierow, K. (2006). Local heat transfer measurements of steam/air mixtures in horizontal condenser tubes. *International Journal of Heat and Mass Transfer*, 49(15–16), 2491–2501. <https://doi.org/10.1016/j.ijheatmasstransfer.2006.01.025>
- Zohuri, B., & McDaniel, P. (2019). *Thermodynamics in Nuclear Power Plant Systems* (Second). Springer International Publishing. <https://doi.org/10.1007/978-3-319-93919-3>

